

International Journal of Thermodynamics

Editor-in-Chief

L. Kuddusi

Honorary Editors

A. Bejan

M. J. Moran

J. Szargut

G. Tsatsaronis

A. Valero

M. R. von Spakovsky

Abstracting and Indexing:

Chemical Abstracts Services, Copernicus, DOAJ, EBSCO, Emerging Sources Citation Index, Engineering Index, Google Scholar, Scopus, and ULAKBIM



*International Centre for
Applied Thermodynamics*

Editor-in-Chief

Prof. Dr. Lütfullah KUDDUSİ

Associate Editor-in-Chief

Assoc. Prof. Dr. Patrice ESTELLÉ

Prof. Dr. Enrico SCIUBBA

Associate Editor

Prof. Dr. Ali KOSAR

Prof. Dr. Derya Burcu ÖZKAN

Prof. Dr. Mustafa ÖZDEMİR

Prof. Dr. Ahmet DURMAYAZ

Assoc. Prof. Dr. Onur TAYLAN

Prof. Dr. Mehmet ARİK

Prof. Dr. Ayşegül ABUŞOĞLU

Prof. Dr. G. Reza VAKİLİ-NEZHAAD

Prof. Dr. Bayram ŞAHİN

Assoc. Prof. Dr. Murat ÇAKAN

Editorial Board

Prof. Dr. Yasar DEMİREL

Prof. Dr. Lütfullah KUDDUSİ

Prof. Dr. Ahmet DURMAYAZ

Prof. Dr. Derya Burcu ÖZKAN

Prof. Dr. Mustafa ÖZDEMİR

Prof. Dr. Ali KOSAR

Prof. Dr. Mehmet ARİK

Assoc. Prof. Dr. Abdussamet SUBASI

Prof. Dr. Daniel FAVRAT

Prof. Silvia Azucena NEBRA

Prof. Dr. Luis SERRA

Assoc. Prof. Dr. Onur TAYLAN

Prof. Dr. Francois MARECHAL

Prof. Dr. Gian Paolo BERETTA

Prof. Dr. Ayşegül ABUŞOĞLU

Prof. Dr. Abel HERNANDEZ-GUERRERO

Prof. Dr. Silvio DE OLIVEIRA JUNIOR

Prof. Dr. Sean WRIGHT

Prof. Dr. Nilufer EGRİCAN

Prof. Dr. G. Reza VAKİLİ-NEZHAAD

Prof. Dr. Bayram ŞAHİN

Prof. Dr. Vittorio VERDA

Assoc. Prof. Dr. Murat ÇAKAN

Publishing Editor

Assoc. Prof. Dr. Abdussamet SUBASI

Assist. Prof. Mustafa Yasin GÖKASLAN

Res. Assist. Ali Murat BİNARK

Language Editor

Assoc. Prof. Dr. Abdussamet SUBASI

Journal Contacts

Editor-in-Chief

Prof. Dr. Lütfullah Kuddusi

ISTANBUL TECHNICAL UNIVERSITY

kuddusi@itu.edu.tr

+902122931300/2452

Department of Mechanical Engineering

Istanbul Technical University

Gumussuyu, 34437 Istanbul Turkey

Volume: 27

Issue: 4

Web: <https://dergipark.org.tr/tr/pub/ijot>

International Journal of Thermodynamics (IJoT)

ISSN:1301-9724 / e-ISSN:2146-1511

CONTENTS

Research Article

1. Performances Study of Eco-friendly Binary Azeotropic Mixtures Used as Working Fluid in Three Refrigeration Cycles 1-13

L. Mchouchi, Y. Tamene, H. Madani, M. Mehemmai

Research Article

2. Analysis of Thermodynamic Models for Liquid-Vapor Equilibrium: Evaluating Accuracy and Applicability 14-22

A. Zerfa, H. Madani, H. Grine, A. Beicha

Research Article

3. Thermodynamic Properties of R1234yf and DMAC Binary Solution 23-29

B. Gurevich

Research Article

4. Thermodynamic Efficiency Analysis of a Combined Power and Cooling (ORC-VCRC) System Using Cyclopentane (C₅H₁₀) as a Substitute for Conventional Hydrocarbons 30-42

Y. Maalem, H. Madani

Research Article

5. Highly Efficient Energy Integration: Thermodynamic Analysis of Heat Recovered from SOFC Through S-CO₂ And Kalina Cycles 43-55

A. Elbir

Research Article

Performances Study of Eco-friendly Binary Azeotropic Mixtures Used as Working Fluid in Three Refrigeration Cycles

¹L. Mchouchi , ^{2*}Y. Tamene , ³H. Madani , ⁴M. Mehemmai 

^{1,2,3,4} Laboratory of Studies of Industrial Energy Systems (LESEI), Department of Mechanical Engineering, Faculty of Technology, University of Batna 2, 05000 Batna, Algeria

E-mails: ¹l.mchouchi@univ-batna2.dz, ^{2*}y.tamene@univ-batna2.dz, ³h.madani@univ-batna2.dz, ⁴mohammed.mehemmai@univ-batna2.dz

Received 12 July 2024, Revised 2 October 2024, Accepted 24 October 2024

Abstract

According to the European (F-gas) regulation, all refrigerants with a global warming potential (GWP) above 150 will be out by 2030. Searching for alternative refrigerants that are environmentally friendly has become an urgent challenge for the refrigeration and air-conditioning sector. Based on their environmental advantages and good thermo-physical properties, azeotropic mixtures have recently gained special interest as substitutes for conventional refrigerants. This study aims to compare the performance of three eco-friendly azeotropic mixtures with the common refrigerant R134a in three refrigeration cycles: the basic cycle (BC), the ejector-expansion refrigeration cycle, and the ejector sub-cooled cycle. The mixtures under study are R1234ze+R600a, R1234yf+R600a, and R1234yf+R290. These mixtures have global warming potential (GWP) of 5.668, 3.8688, and 3.2865 respectively, whereas R134a has a GWP of 1430.

To reach this objective a numerical program was developed using MATLAB software to evaluate the coefficient of performance (COP), and the cooling capacity of the three refrigeration cycles using the studied eco-friendly mixtures and were compared with those of the commonly used R134a refrigerant. The entrainment ratio was also compared for the two ejector cycles using these refrigerants. The simulation was realized for condensing temperatures (T_c) selected between 30 and 55°C and evaporation temperatures (T_e) ranging between -10 and 10°C. The results have shown that the eco-friendly azeotropic mixture R1234yf+R290 (GWP=3.51) has the best performances compared to the two other mixtures and they are close to those of R134a. On the other hand, the ejector expansion refrigeration cycle has exhibited a high coefficient of performance compared to the basic cycle and ejector sub-cooled cycle, and a high entrainment ratio compared to the ejector sub-cooled cycle for all used refrigerants. However, the ejector sub-cooled cycle gave a better cooling capacity than the other cycles. According to the obtained results, the azeotropic mixture R1234yf+R290 apart from its excellent environmental properties yields better performances in most of cases, this confirms that it could be a suitable substitute for conventional working fluid R134a which has a great global warming potential.

Keywords: Azeotropic mixtures; ejector cycle; entrainment ratio; global warming potential.

1. Introduction

Finding high-performing, environmentally friendly working fluids with low environmental effects is a major challenge facing the refrigeration sector. The European F-gas regulation mandates the phase-out of refrigerants with GWPs greater than 150 by 2030 [1].

The usually used refrigerants in the applications of thermodynamic machines such as heat pumps, air-conditioning, and refrigeration systems have a good performance but a high global warming potential (GWP), which has a significant negative influence on the environment and adds significantly to atmospheric greenhouse gas concentrations [2]. In refrigeration engineering, finding effective refrigeration systems is also crucial. The introduction of the technology of ejector expansion in the cooling systems to improve cooling efficiency was proposed for the first time by Kornhauser [3] in 1990. Several studies have focused on the amelioration of the conventional vapor-compression refrigeration cycle.

Xing et al. [4] have proposed a novel vapor-compression refrigeration cycle with mechanical sub-cooling using an ejector to improve the performance of a conventional single-stage vapor-compression refrigeration cycle. Their simulation results have shown the novel cycle displays volumetric refrigeration capacity improvements of 11.7% with R404A and 7.2% with R290 when the evaporator temperature ranges were from -40 to -10 °C, and the condenser temperature was 45 °C on the other hand, the novel cycle has achieved COP improvements of 9.5% with R404A and 7.0% with R290. In addition, they deduced that the improvement of the COP and cooling capacity of this novel cycle largely depends on the operation pressures of the ejector.

Yang et al. [5] studied a novel combined power and ejector-refrigeration cycle using a zeotropic mixture, and it was compared with a conventional combined power and ejector-refrigeration cycle. It was found that the cycle exergy

achieves a maximum value of 10.29% with a mixture of isobutane/pentane (40%/60%), and the thermal efficiency gets a maximum value of 10.77% with a mixture of isobutane/pentane (70%/30%). The mixture of isobutane/pentane (80%/20%) has given a maximum temperature glide in the evaporator of 15.09 K.

In another study, based on the first and second laws of thermodynamics, a theoretical analysis of the performance of this new cycle was carried out by Yari and Sirousazar [6]. It was found that the COP and second law efficiency values of the new ejector-vapour compression refrigeration cycle are on average 8.6 and 8.15 % higher than that of the conventional ejector-vapour compression refrigeration cycle with R125. It was also shown that the COP of the new cycle is 21 % higher than that of conventional vapor compression.

Disawas and Wongwises [7] conducted an experimental study comparing the performance of a two-phase ejector refrigeration cycle with that of a conventional refrigeration cycle. The results showed that the coefficient of performance of the two-phase ejector refrigeration cycle was higher than that of the conventional refrigeration cycle across all experimental conditions. However, it was observed that as the heat sink temperature increased, the growth became relatively smaller. A literature review on two-phase ejectors and their applications in compression refrigeration systems and heat pumps was conducted by Sarkar [8]. The review revealed that both theoretical and experimental studies have confirmed that using an ejector as an expansion device can significantly improve the performance of subcritical and transcritical refrigeration and heat pump cycles. The review also showed that the improvement in energetic or exergetic performance by using an ejector is greatly influenced by the cycle operating conditions, the working fluids used, and the ejector geometries.

Besagni et al. [9] have presented a literature review on ejector refrigeration systems and working fluids. They deeply analyzed ejector technology and behavior, refrigerant properties and their influence on the ejector performance, and all of the ejector refrigeration technologies, with a focus on past, present, and future trends. They concluded that the use of heat-driven ejector refrigeration systems could be a promising alternative to traditional compressor-based refrigeration technologies for energy consumption reduction.

The incorporation of an ejector into the vapor compression cycle leads to improving the COP by reducing the throttling loss associated with the expansion device. A numerical simulation using a one-dimensional model based on mass balances was made by Nehdi et al. [10]. According to the simulation results of the improved cycle, it has been shown that the geometric parameters of the ejector design have considerable effects on the system's performance. A comparison of four different refrigeration cycles using ternary mixtures was proposed by Maalem et al. [11]. Their results showed that the cycle with booster and ejector gave better performance than the other studied cycles.

Many researchers have studied the use of pure refrigerants as working fluids in the ejector refrigeration cycle. Sarkar [12] conducted a comparative analysis of the performance of three natural refrigerants using the ejector expansion refrigeration cycle. The findings indicated propane yields a maximum COP improvement of 26.1 % followed by isobutane (22.8 %) and ammonia (11.7 %) for studies ranges. A thermodynamic analysis of an air conditioning system is conducted by Aisyah and Ariyadi [13] to assess the performance of R1224yd and compared to R123 and R245fa.

The system is analyzed from a thermodynamic perspective and key performance indicators such as the Coefficient of Performance and exergy efficiency. The results are then compared to R245fa and R123. Results showed that R1224yd offers better performance than R245fa which has 1-3% higher performance value and exergy efficiency and has comparable performance to R123.

Rostamnejad and Zare [14] proposed a new ejector-expansion refrigeration cycle, and a comparison was made with the standard ejector-expansion refrigeration cycle and conventional vapor compression refrigeration system. Six environmentally friendly refrigerants were utilized as working fluids. Their results showed that, among the six investigated refrigerants, R1234ze is the best one for which the proposed system has 5.7% and 15.5% higher exergy efficiency values than the standard ejector-expansion refrigeration cycle and conventional vapor compression refrigeration, respectively, at a condensing temperature of 40 °C and evaporation temperature of 5 °C.

Ma et al. [15] conducted a numerical study of the fundamental refrigeration cycle with an ejector, using several hydrocarbon refrigerants, including propane, butane, isobutane, and propylene, as working fluids. The findings have shown that the ejector-expansion refrigeration cycle using hydrocarbons has greater COP, volumetric cooling capacity, and exergy efficiency, as well as lower exergy destruction compared with the standard refrigeration cycle. In another hand, they have noticed that propane and propylene have better performance than isobutene and butane.

A numerical model based on the energetic and exergetic methods has been developed by Maalem et al. [16] to compare the eco-friendly refrigerant R131I with the usually used fluid R134a in the ejector-expansion refrigeration cycle. The thermodynamic performances studied include the coefficient of performance (COP), the entrainment ratio (μ), the exergy destruction, and the exergy efficiency. Their results have indicated that the R131I has a better performance in terms of the entrainment ratio and the coefficient of performance, as well as lower exergy destruction compared to R134a. Li et al. [17] made a theoretical study on the performance characteristics of the ejector-expansion refrigeration cycle using R1234yf as refrigerant have been investigated. They showed that the EERC R1234yf has better performance than the standard refrigeration cycle, and the improvement is more important under the conditions of a higher condensation temperature and a lower evaporation temperature. The coefficient of performance and volumetric cooling capacity improvements of the ejector-expansion refrigeration cycle over the standard refrigeration cycle are also greater than that of the cycle using R134a as a working fluid.

Lucas et al. [18] have presented an ejector operation characteristic for a CO₂ ejector based on experimental data, which is designed to be used in system simulations such as the refrigeration cycle. Based on experimental data, correlations for the ejector efficiency and the driving mass flow rate were determined and used. The correlation for the ejector efficiency, which uses dimensionless coefficients, has predicted the experimental data within 10%.

Ozone depletion potential (ODP) and global warming potential (GWP) have recently become the two fundamental parameters in new refrigerants investigation, finding environmentally friendly refrigerants is therefore essential.

Binary azeotropic mixtures emerge as the most viable alternatives to conventional refrigerants in the vapor compression refrigeration cycle, Calleja-Anta et al [19] have studied experimentally the mixture RE170/R600 as a potential drop-in refrigerant of R600a. For a given operating condition, the energy performance of RE170/R600 mixtures with a maximum proportion of 27.5 % of RE170 has been tested using a water-to-water single-stage compression cycle, measuring COP increments from 10.1 to 17.6 % in relation to R600a. Then, the blend RE170/R600 (15/85 %), considered as the potential drop-in fluid of R600a, has been tested in a wide range of operating conditions, concluding that it offers the same cooling capacity as R600a but with COP increments from 12.6 % to 17.6 %.

Benbai et al. [20] have numerically studied six azeotropic mixtures, R1234yf + R290, R1234yf + R152a, R1234yf + R600a, R134a + R290, R134a + R600a, and R1270 + R134a, in single-stage steam compression refrigeration system. The effect of the entrainment ratio on the coefficient of performance has been investigated for the six refrigerants. The simulation results showed that the R1234yf + R290 mixture has given the highest coefficient of performance and entrainment ratio.

Using a constant-pressure two-phase ejector model, a numerical study was realized by Zhao et al. [21] to study the performance evolution of the ejector-expansion refrigeration cycle, the zeotropic mixture R134a/R143a was selected as working fluid. The simulation results reveal that the cycle COP increases first and then decreases as the mass fraction of R134a increases. The COP has reached a maximum value of 4.18 with a mass fraction of 0.9 and has yielded a minimum value of 3.66 with a mass fraction of 0.5. With mixture 0.9/0.1, the COP improvement has reached a maximum value of 10.47%.

The performance of the refrigeration cycle with ejector using four zeotropic binary mixtures based on R1234yf (R1234yf + R152a, R1234yf + R134a, R1234yf + R32, and R1234yf + R125) was investigated by Mehemmai et al. [22]. The effects of key operating parameters such as evaporation temperature, condensation temperature, and mass fraction were also analyzed. Their results showed that the COP of the two mixtures (R1234yf + R152a and R1234yf + R134a) was not affected by the change in mass fractions on the other hand the mass fractions variation had a significant effect on the COP of the two other mixtures: R1234yf + R32 and R1234yf + R125. Among studied mixtures and fractions used, the mixture R1234yf + R152a has given the highest COP with a mass fraction of 0.75.

To investigate the performance of an ejector refrigeration cycle using three CO₂-based mixtures (CO₂+R290, CO₂+R1234yf, CO₂+R600a) in subcritical mode, and CO₂+R116 in transcritical mode, Abdou et al. [23] have developed a simulation program. Results have shown that the suction nozzle pressure drop influences significantly the cycle performance, but does not affect the entrainment ratio of the ejector. On the other hand, they found that the maximum performance of refrigeration cycles, in sub or trans-critical mode, was proportional to the evaporation temperature and was inversely proportional to the temperature of the condenser-gas cooler.

Liu et al. [24] established a model for a refrigeration cycle with an ejector using zeotropic refrigerants as a working fluid. Different mixtures were studied (R123/R245fa, R245fa/R141b, R141b/RC318, R245fa/R134a, R245fa/R22, R141b/R134a, R245fa/R143a,

and R141b/R22). The performance of the ejector refrigeration cycle was studied, and results have indicated that the outlet temperatures of both the generator and evaporator can be increased using a zeotropic mixture compared to that using a pure refrigerant, contrariwise the average temperature difference of the heat transfer in the condenser is larger than that of the pure refrigerant. Among the studied refrigerants, using R245fa/R22 (0.3/0.7) as the working medium yields the refrigeration cycle with the best COP (0.293), which is 4% and 22% higher than those using R22 and R245fa, respectively. The results have revealed the advantages of zeotropic refrigerants.

From the literature review, it was noticed that the types of cycles as well as the used refrigerants have an important influence on the final performances of the refrigeration Machinery. This work aims to investigate the performances of three different refrigeration cycles using environmentally friendly binary mixtures and compare them with the usually used refrigerant R134a. The selected azeotropic mixtures are R1234ze+R600a, R1234yf+R600a, and R1234yf+R290, they have respectively a global warming potential (GWP) equal to 5.668, 3.8688, and 3.2865.

2. Studied Cycles

In this study, performances of three refrigeration cycles using azeotropic eco-friendly mixtures as working fluids are investigated.

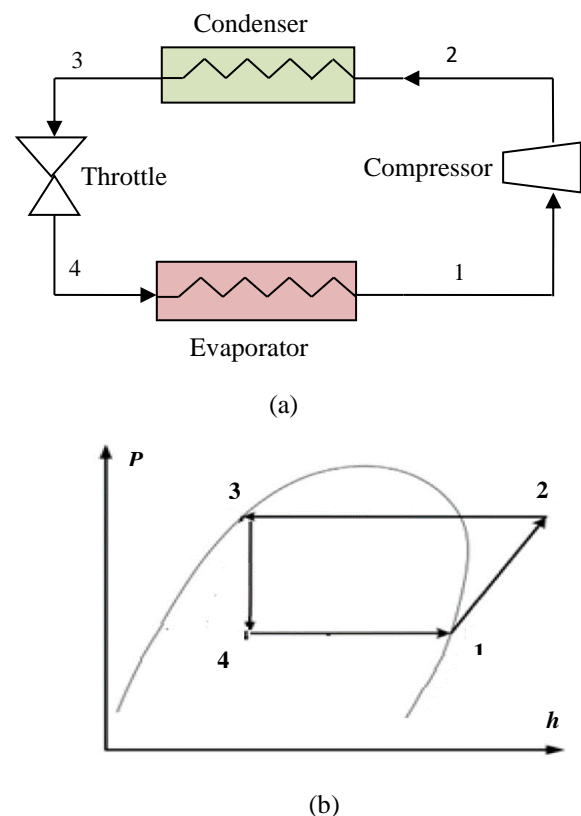
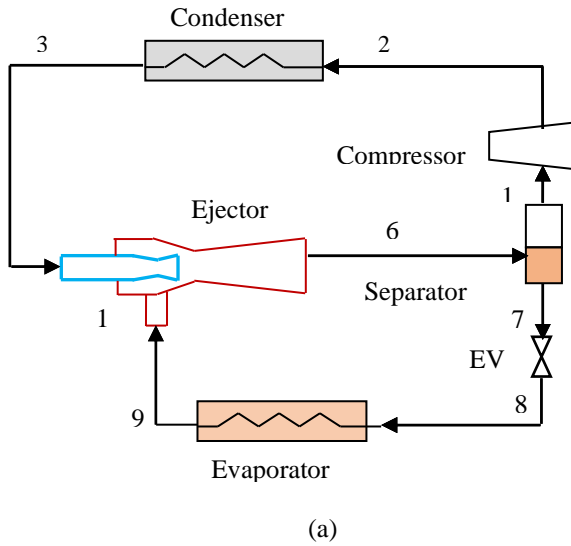
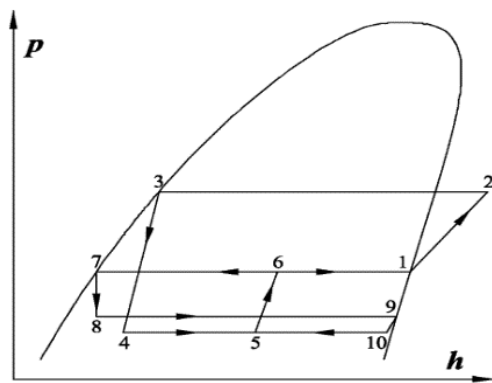


Figure 1. Schematic cycle (a) and P-h diagram (b) of the Basic Cycle [23].

The schematic representation and P-H diagrams of the concerned cycles are represented in Figure.1 for the basic cycle (BC), in Figure.2 for the ejector-expansion refrigeration cycle (Configuration 1), and in Figure.3 the ejector sub-cooled cycle (Configuration 2).



(a)



(b)

Figure 2. Schematic cycle (a) and P-h diagram (b) of the ejector-expansion refrigeration cycle (Configuration 1) [16].

Since the ejector is the more important component in the ejector cycles, it determines the performance of the cycle. The ejector model is classified into two types: constant pressure mixing model and constant area mixing model. According to previous studies (Sumeru et al [25]; Khalil et al.[26]; He et al. [27]; Li et al. [17]; Sarkar [8]; Xing et al. [4]) the constant-pressure mixing model is better than the constant-area mixing model. In this study, this model was adopted. For the ejector, the mathematical model is detailed below.

3. Mathematical Modelling and Simulation

3.1 Ejector Modelling [17] [4]

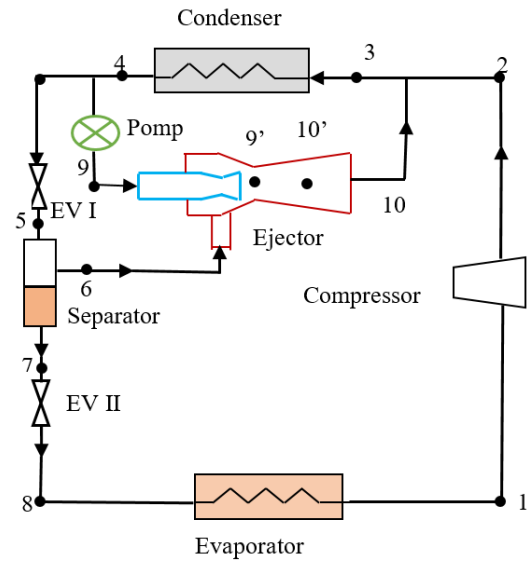
The entrainment ratio μ is an important parameter for assessing the ejector's performance it is defined as following:

$$\mu = \frac{m_s}{m_p} \quad (1)$$

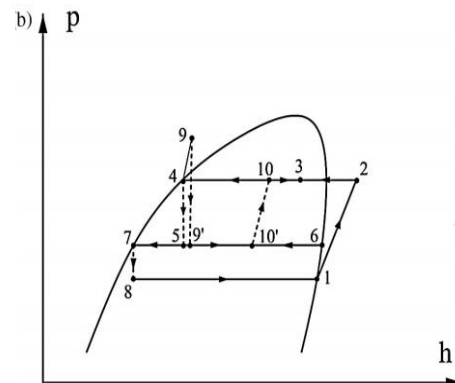
Where m_p and m_s represent respectively, the mass flow rates of the primary and secondary flows.

The thermodynamic analysis has been conducted on the following common assumptions [17].

- Steady-state conditions are assumed.
- The throttling process in the expansion valve is isenthalpic.



(a)



(b)

Figure 3. Schematic cycle (a) and P-h diagram (b) of the ejector sub-cooled cycle (Configuration 2) [3].

- The azeotropic composition of each binary mixture remains constant throughout the process.
- Neglecting the pressure drop in heat exchangers and connecting pipes.
- The entry and exit velocities of the ejector are neglected.
- Engine flow and suction flow reach the same pressure at the inlet of the constant-area mixing section of the ejector, and no mixing occurs between the two flows before the inlet of the mixing section.
- The refrigerant leaving the condenser and evaporator ports is saturated.
- Heat does not transfer with the environment surrounding the system except in the condenser.
- The compressor has isentropic efficiency.

3.2 Motive Nozzle Outlet

The velocity of the motive fluid in the exit nozzle is given by:

$$u_{p,out} = \sqrt{2(h_{p,in} - h_{p,out})} \quad (2)$$

$$h_{p,out} = h_{p,in} - \eta_m(h_{p,in} - h_{p,out,is}) \quad (3)$$

Where $h_{p,in}$, is the inlet specific enthalpy of the primary fluid, $h_{p,out,is}$ is the exit enthalpy through an isentropic expansion process in the nozzle.

3.3 Suction Nozzle

For the ejector-expansion refrigeration cycle, at the suction nozzle outlet, the following equations can be applied:

$$h_{s,out} = h_{s,in} - \eta_s(h_{s,in} - h_{s,out,is}) \quad (4)$$

$$u_{s,out} = \sqrt{2(h_{s,in} - h_{s,out})} \quad (5)$$

For the ejector sub-cooled cycle at the suction nozzle the velocity is neglected Xing et al [4]

3.4 Mixing Chamber

The velocity exiting the mixing chamber for the ejector-expansion refrigeration cycle is given by:

$$u_{mix,out} = \sqrt{\eta_m} \left(\frac{1}{(1+\mu)} u_{p,out} + \frac{\mu}{(1+\mu)} u_{s,out} \right) \quad (6)$$

And for the ejector sub-cooled cycle it is given by:

$$u_{mix,out} = \sqrt{\eta_m} \left(\frac{1}{(1+\mu)} u_{p,out} \right) \quad (7)$$

The enthalpy and the entropy of the refrigerant at the mixing chamber for the ejector-expansion refrigeration cycle are given by:

$$h_{mix,out} = \frac{1}{(1+\mu)} \left(h_{p,out} + \frac{u_{p,out}^2}{2} \right) + \frac{\mu}{(1+\mu)} \left(h_{s,out} + \frac{u_{s,out}^2}{2} \right) - \frac{u_{mix,out}^2}{2} \quad (8)$$

$$s_{mix,out} = s(h_{mix,out}, p_{mix,out}) \quad (9)$$

The enthalpy of the refrigerant at the mixing chamber for the ejector sub-cooled cycle is given by:

$$h_{mix,out} = \frac{h_{p,in} + \mu h_{s,in}}{(1+\mu)} - \frac{u_{mix,out}^2}{2} \quad (10)$$

3.5 Diffuser Section Model.

The following relation calculates the specific enthalpy at the diffuser outlet:

$$h_{d,out} = h_{mix,out} + \frac{u_{mix,out}^2}{2} \quad (11)$$

And for the ejector sub-cooled cycle it given by:

$$h_{d,out,is} = h_{mix,out} + \eta_d(h_{d,out} - h_{mix,out}) \quad (12)$$

The ideal specific enthalpy of the mixed fluid at the diffuser's output can be obtained by using the definition of the diffuser's isentropic efficiency η_d for the ejector-expansion refrigeration cycle can be written as:

$$h_{d,out,is} = h_{mix,out} + \eta_d(h_{d,out} - h_{mix,out}) \quad (13)$$

For the ejector sub-cooled cycle, the specific enthalpy at the diffuser outlet is given by:

$$h_{d,out,is} = h(P_d, s_{out}) \quad (14)$$

The pressure and vapor quality of the refrigerant outlet the ejector-expansion refrigeration cycle are expressed by:

$$p_{d,out} = p(h_{d,out,is}, s_{mix,out}) \quad (15)$$

$$x_{d,out} = x(h_{d,out}, p_{d,out}) \quad (16)$$

To verify the preliminary input value for the entrainment ratio (μ), the following conditions must be satisfied: For the ejector-expansion refrigeration cycle

$$x_{d,out} = \frac{1}{1+\mu} \quad (17)$$

From the above equations neglecting the diffuser outlet velocity, the entrainment ratio for the ejector sub-cooled cycle is summarized:

$$\mu = \sqrt{\frac{\eta_n \eta_m \eta_d (h_{p,in} - h_{p,out})}{(h_{d,out,is} - h_{mix,out})}} - 1 \quad (18)$$

The refrigeration COP (coefficient of performance) of the cycles can be expressed as:

$$COP = \frac{q_{col,evap}}{w_c} \quad (19)$$

$$COP = \frac{q_{col,evap}}{w_c + w_p} \quad (20)$$

The Operational parameters for both configurations are presented In Table 1, and Table 2 shows the equations used to model each component of the cycles.

Table 1. Operational Parameters for Both Configurations (Li et al [17] Maalem et al [11]; Xing et al [4]).

Parameter	Symbol	Value
Evaporating temperature	Te (°C)	5
Condensing temperature	Tc (°C)	40
Motive nozzle efficiency	η_n (%)	85
Suction nozzle efficiency	η_s (%)	85
Mixing section efficiency	η_m (%)	95
Diffuser efficiency	η_d (%)	85
Efficiency pump	η_p (%)	75

Based on the mathematical model built, a computer program was developed in MATLAB and the refrigerants thermodynamic properties were obtained using REFPROP Version 9.0 to investigate the performance of the studied mixtures used as working fluid in three refrigeration cycles.

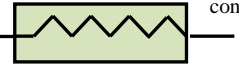



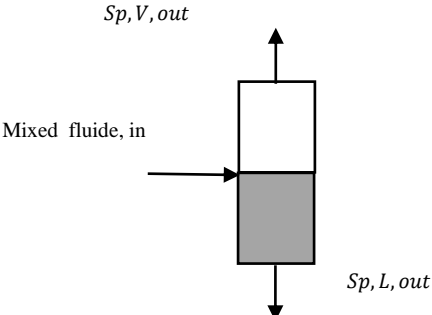
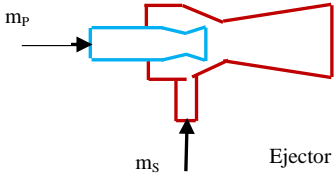

The detailed flowchart for the two ejector cycles calculation procedure is presented in Figure 4.

4. Results and Discussion

4.1 Environmental and Critical Properties of Working Fluids.

The environmental properties (GWP and ODP) have become the most important properties in the research and development of alternative working fluids. The critical and environmental properties of the azeotropic mixtures concerned in this study are presented in Table 3.

Table 2. Components Characteristic Equations.

Component	Characteristic Equations
 <p>Condenser</p>	<p>BC $q_{col} = h_{cond,out} - h_{cond,in}$ Configuration 1. $q_{col} = \frac{h_{cond,out} - h_{cond,in}}{1+\mu}$ Configuration 2. $q_{col} = 2(h_{cond,out} - h_{cond,in})$</p>
 <p>Evaporator</p>	<p>(BC): $q_{col} = h_{evap,out} - h_{evap,in}$ Configuration 1 $q_{col} = \frac{\mu(h_{evap,out} - h_{evap,in})}{1+\mu}$ Configuration 2 $q_{col} = m'_1(h_{evap,out} - h_{evap,in})$</p>
 <p>Compressor</p>	<p>BC : $w_c = h_{c,out} - h_{c,in}$ $\eta_c = 0.874 - 0.0135\pi$ [28] Configuration 1 $w_c = \frac{h_{c,out} - h_{c,in}}{1+\mu}$ $h_{c,out} = h_{c,in} + \frac{h_{c,out,is} - h_{c,in}}{\eta_c}$ Configuration 2 $w_c = m_{c,in}(h_{2is} - h_1)/\eta_c$ [4]</p>
 <p>Throttle valve</p>	<p>For BC, Configuration 1 and 2 $h_{tv,out} = h_{tv,in}$</p>
 <p>Separator</p>	<p>$h_{Sp,L,out} = h(p_{d,out}, x_{d,out} = 0)$ $h_{Sp,V,out} = h(p_{d,out}, x_{d,out} = 1)$</p>
 <p>Ejector</p>	<p>Calculation algorithm proposed by Li et al. [17] for Configuration 1. And by Xing et al [4] for Configuration 2</p>
 <p>Pump</p>	<p>$w_p = m_p(h_{9s} - h_4)/\eta_p$</p>

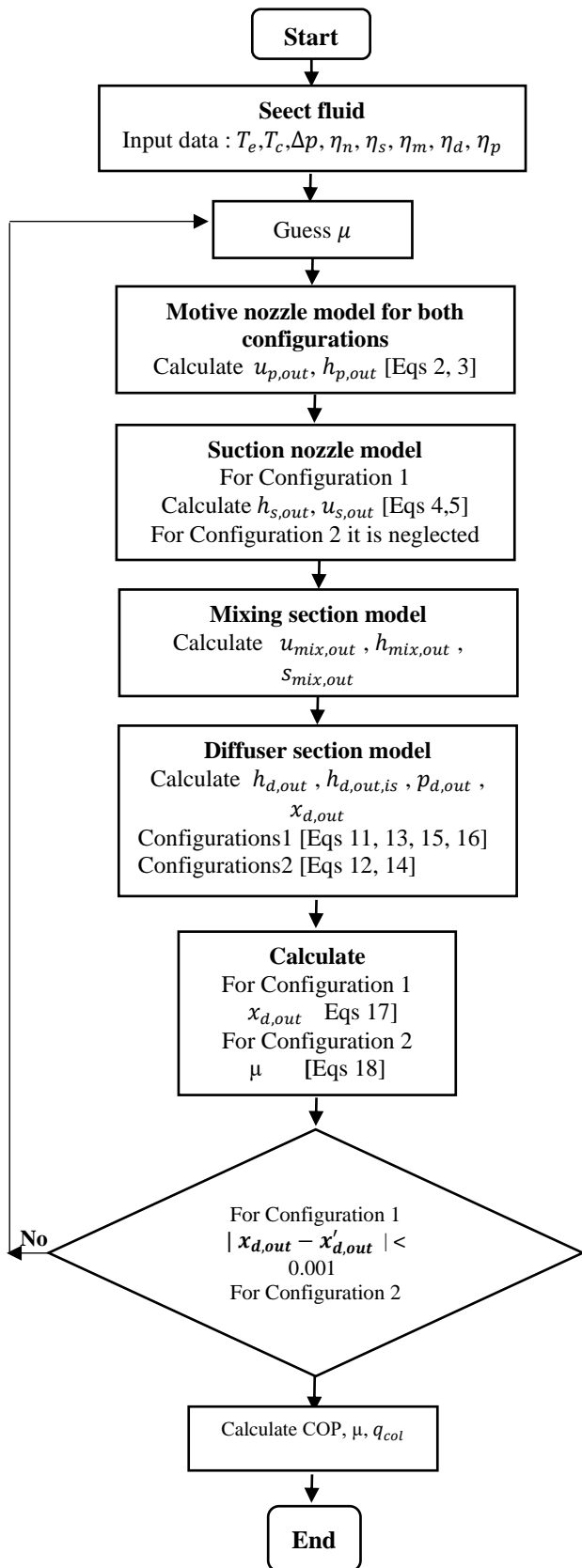


Figure 4. Flowchart for both ejector cycles calculation procedure.

The different values are obtained using the equations below:

Critical temperature T_c

$$T_{c_{mixture}}(k) = \sum_i^n x_{pure, i} * T_{c_{pure, i}} \quad (21)$$

Critical pressure P_c

$$P_c(k)_{mixture} = \sum_i^n x_{pure, i} * P_{c_{pure, i}} \quad (22)$$

Where $x_{pure, i}$ represents the molar fraction of component i in the mixture.

Table 3. Environmental and critical properties of working fluids.

Working Fluids	GWP	Critical Temperature $T_c(k)$	Critical Pressure $P_c(MPa)$	Mass Fraction*	Molar Fraction
R1234ze +R600a	5.40	390.9 40	3.6365	0.7972/ 0.208	0.6670/ 0.33
R1234yf +R600a	3.93	373.0 98	3.4161	0.9285/ 0.0715	0.8686/ 0.1314
R1234yf +R290	3.51	369.3 01	4.0003	0.4879/ 0.5121	0.2887/ 0.7113
R134a	1430	374.2 10	4.0593	/	/

* For those values of the mass fractions, the binary mixtures are azeotropic.

Global warming potential of mixtures relation [11]:

$$GWP_{mixture} = \sum_i^n GWP_{pure, i} * w_{pure, i} \quad (23)$$

Where $w_{pure, i}$ represents the mass fraction of component i in the mixture.

From values of the Table 3, it can be seen that the three azeotropic mixtures exhibits a global warming potential lower than six, while the phase-out R134a has high GWP (GWP=1430).

4.2 Validation of Developed Code.

Before using the developed program to compare the performances of azeotropic mixtures with the traditional single fluid R134a in the three refrigeration cycles concerned in this study, the developed program was validated with found studies in the literature.

The developed program has been validated under the same operating conditions, by comparing the values of the entrainment ratio with the results reported by Maalem et al. [11] and the results of volumetric refrigeration capacity reported by Xing et al. [4].

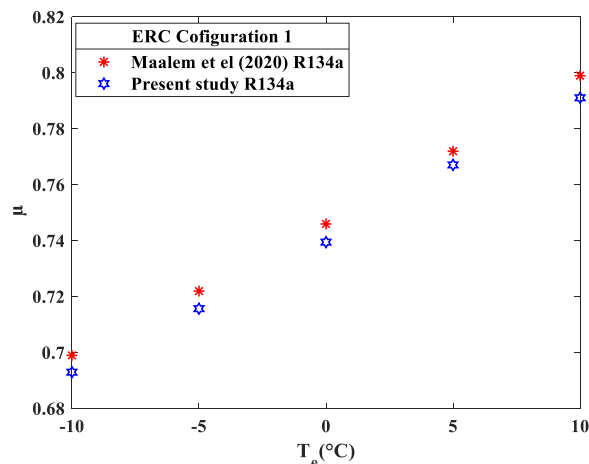


Figure 5. Validation of developed code with li et al [16].

From Figure 5 the entrainment ratio evolves from 0.699 to 0.799 when T_e varies between -10 to 10 °C for Maalem et al and in this study, it varies between 0.693 and 0.791 for the same T_e variation. Similarly, for Figure 6 the volumetric refrigeration capacity varies between 799.556 kJ/m^3 and 2877.959 kJ/m^3 when T_e evolves from -40 to -10 °C for Xing et al and in this study, it varies between 797.748 kJ/m^3 and 2876.283 kJ/m^3 for the same T_e variation. A good agreement can be noted between the results obtained from the developed program and those of the references.

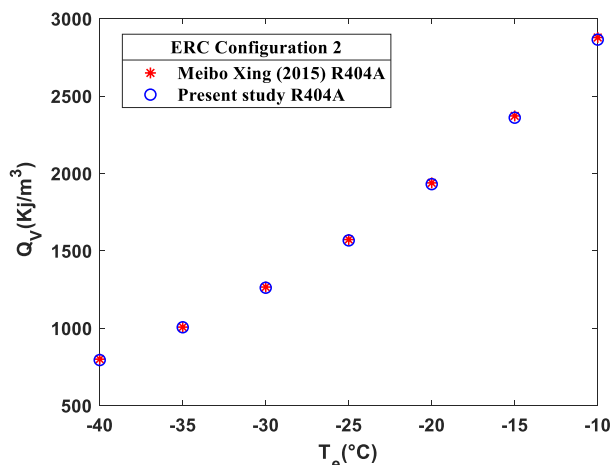


Figure 6. Validation of developed code with Xing et al [3]. For $T_c=25$ °C and pressure ratio = 1.14.

4.3 Performances Computation of Working Fluids

4.3.1 Influence of Condensing Temperatures on Performances

In this section, the effects of condenser temperature (T_c) for a constant evaporation temperature (T_e) of 5 °C on the performances of the basic cycle, the ejector-expansion refrigeration cycle, and the ejectorsub-cooled cycle using the investigating fluids are presented.

With the same condenser outlet temperatures (30 to 55) °C, Figure 7 shows the simulated results of the variation of the coefficient of performance (COP) values of the three refrigeration cycles using the investigating fluids. It was noted that the COP decreases in all refrigeration cycles with the increase in condenser temperature. This decrease is directly linked to the variation in enthalpy of the condenser in the refrigeration cycles, while the enthalpy at the evaporator outlet of cooling cycles remains constant.

For the basic cycle (Figure.7 (a)), it was observed that at low condensation temperatures, the COP value obtained with the single working fluid R134a is higher than those of the three investigated working fluid mixtures it decreases from (8.24 to 3.31). However, at high condensation temperatures the COP value obtained with the working fluids R1234ze+R600a are very close (8.04 to 3.3) of those of R134a and higher than the two other working fluid mixtures. The COP values of R1234yf+R600a and R1234yf+R290 decreases from (7.81 to 3.27) and (7.82 to 3.05), respectively, as the condensation temperatures increase from 30 to 55 °C.

For the ejector-expansion refrigeration cycle (as shown in Figure.7 (b)), it was noticed that the COP values obtained with both working fluids R134a and R1234yf+R290 are nearly identical. They decrease from (8.7875 to 3.8501 and (8.8605 to 3.8828), respectively and they are higher than those of R1234ze+R600a and R1234yf+R600a which the

COP decreases from (8.2626 to 3.7417) and (7.5778 to 3.4566), respectively, for all the condensation temperatures. In the case of the ejector sub-cooled cycle (Figure.7 (c)), the COP values obtained with both working fluids R134a and R1234ze+R600a are close, they decrease from (7.4632 to 3.1808) and (7.3193 to 3.1901), respectively. The differences in the COP values between the three cooling cycles can be explained due to the different architectures of each cycle, where the thermodynamic losses (irreversibility) are lower in the architecture of the ejector-expansion refrigeration cycle than the other cooling cycles, which explain the high COP of this cycle.

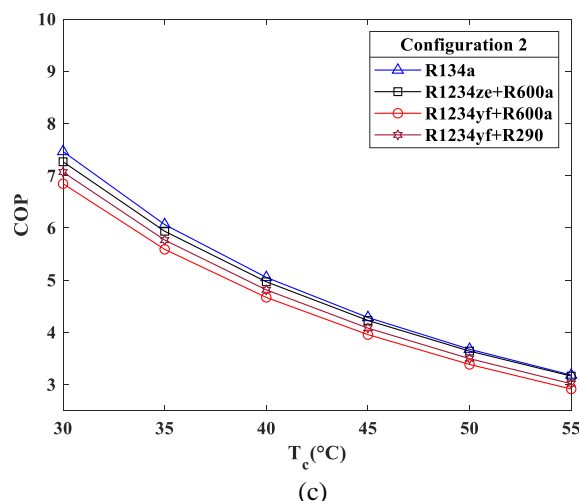
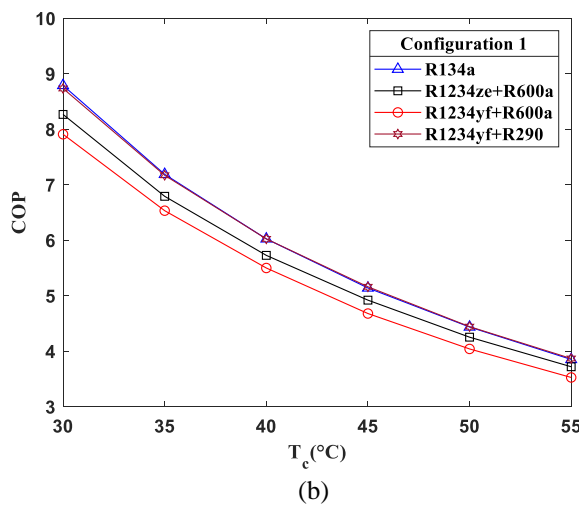
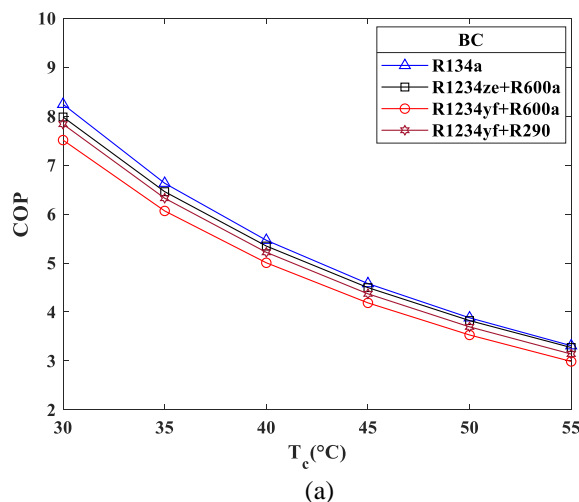


Figure 7. Influence of condensing temperatures on the COP of refrigeration systems.

Figure 8 shows the effect of the condensing temperatures on the cooling capacity of investigating working fluids in the three refrigeration systems. From the obtained numerical results, it is noticed that the cooling capacity decreases with the condensing temperatures. These results can be explained by the fact that the increase of the condensation temperature implies an increase in enthalpy at the condenser outlet of cooling cycles, while the enthalpy at the evaporator outlet of cooling cycles remains constant, which causes a reduction in cooling capacity and consequently, reduction in COP of cooling cycles.

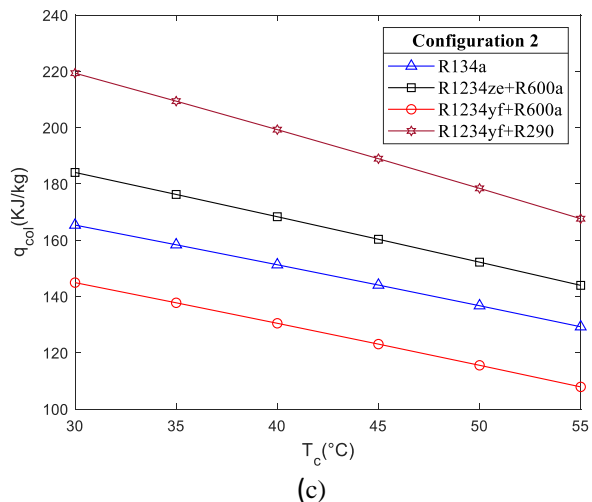
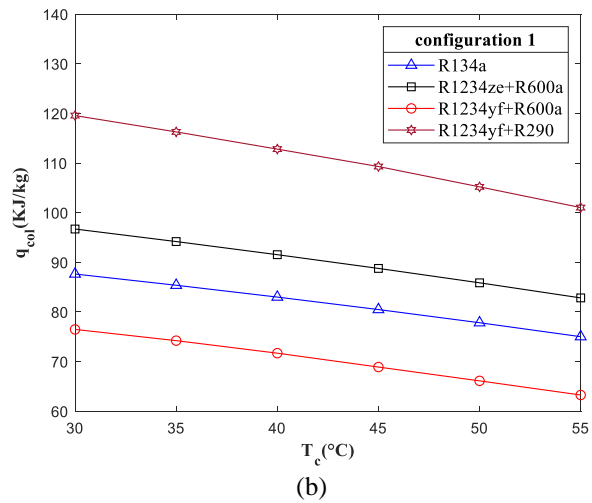
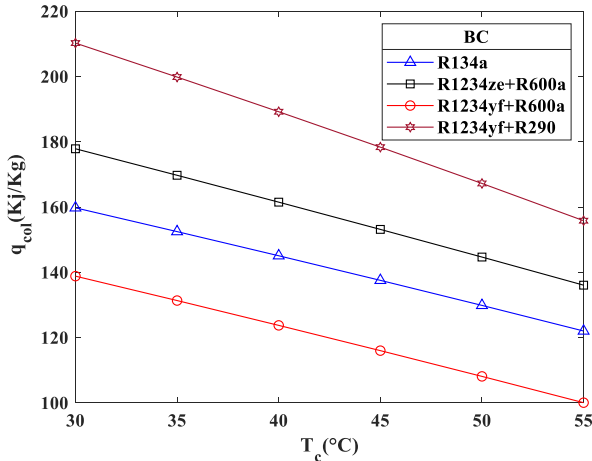


Figure 8. Influence of condensing temperatures on the cooling capacity of refrigeration systems.

The results showed that the maximum values of the cooling capacity in all three cycles are obtained where they work with the mixture R1234yf+R290. It can be also noted that the two mixtures R1234yf+R290 and R1234ze+R600a give a better cooling capacity than R134a.

By comparing the cooling capacity values of the three studied cooling cycles, it can be seen that the ejector sub-cooled cycle (Figure.8 (c)) exhibits the highest cooling capacity (261.847 to 202.1223 kJ/kg), followed by the basic cycle (244.4832 to 188.4839 kJ/kg) (Figure.8 (a)), and finally the ejector-expansion refrigeration cycle(140.5819 to 119.1757 kJ/kg) (Figure.8 (b)).

Figure 9 shows the effect of condensing temperatures on the entrainment ratio (μ) of the ejection expansion cooling cycle and the ejection sub-cooling cycle using the investigated working fluids R1234ze+R600a, R1234yf+R600a, R1234yf+R600a, R1234yf+R290, and R134a. From the simulation results obtained, it can be seen that the entrainment ratio decreases with increasing condenser temperature in both cooling cycles. This can be explained by the fact that when the condensing temperatures increase from (30 to 55°C), the primary mass flow of the motive fluid increases, and the secondary mass flow of entrained fluid decreases, and hence the entrainment ratio of both cycles decreases.

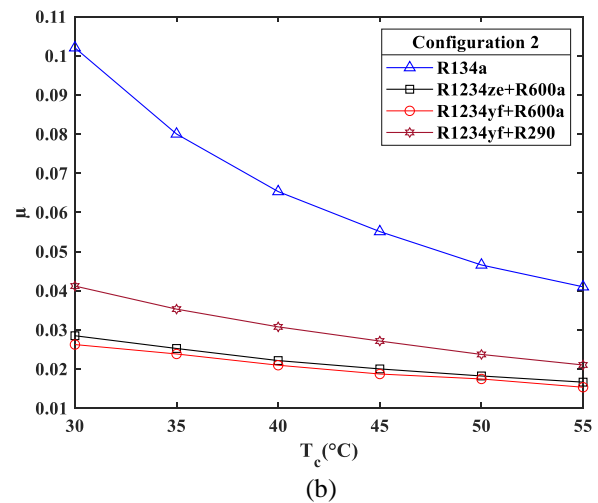
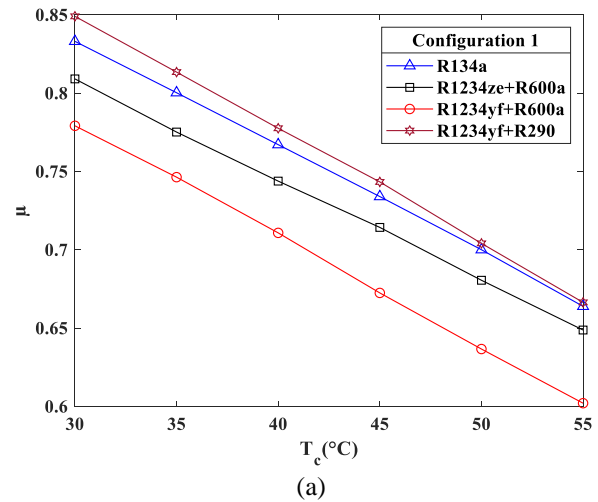


Figure 9. Influence of condensing temperatures on entrainment ratio.

Figure 9(a) and Figure 9(b) show that the working fluid R134a in the two ejector cycles gives a higher entrainment

ratio compared to the mixtures. On the other hand, among the three studied mixtures, the R1234yf+R290 gives the higher entrainment ratio, it vary between 0.85047 and 0.66921 in the ejector-expansion refrigeration cycle.

By comparing the entrainment ratio values of both cycles, it can be seen that the ejector expansion refrigeration cycle (Figure.9 (a)) exhibits the highest entrainment ratio for all working fluids when the condenser temperature ranges from 30 to 55 °C and the evaporator temperature is 5 °C. This is because the primary flow of the motive fluid leaving from the condenser in the ejector-expansion refrigeration cycle is lower than the primary flow of the motive fluid leaving from the pump in the ejector sub-cooled cycle.

4.3.2 Influence of Evaporating Temperatures on Performances

In the following section, the effects of evaporator temperatures (T_e) for a constant condensation temperature (T_c) of 40°C on the performances of the three studied cycles using the investigated mixtures are presented.

Figure 10 shows the variation of the coefficient of performance (COP) of the three refrigeration cycles using the investigated mixtures as working fluids at evaporator temperatures ranging from -10 to 10 °C.

In Figure 10 (a, b, and c), it is evident that the coefficient of performance (COP) of all mixtures increases as the evaporator temperature rises while maintaining a constant condensation temperature of 40°C. This increase is directly related to the change in enthalpy of the evaporator in the refrigeration cycles, while the enthalpy at the condenser outlet of the cycles remains constant. It is noticed from the results that the COP values obtained with the mixture R1234yf+R290 (3,7759 to 7,2792) are higher than those of R134a (3,6956 to 7,2625) and better than the two other mixtures.

Based on Figure 11, it is observed that the cooling capacity of the studied working fluids increases as the evaporation temperatures rise. This is due to that higher evaporation temperatures imply an increase in enthalpy at the evaporator outlet of the cooling cycles, while the enthalpy at the condenser outlet remains constant, which causes an increase in cooling capacity and consequently, the increase in the COP of cooling cycles.

The results showed that the maximum value of the cooling capacity in the three cycles is obtained with the working fluid mixture R1234yf+ R290 (GWP=3.51) followed by R1234ze+R600a, and R134a. The mixture R1234yf+R600a gives the lower values of the cooling capacity in the three cycles. When the evaporation temperature increases from -10 to 10 °C, the cooling capacity of the fluid mixture R1234yf+R290 in the basic cycle increases from 176.1074 to 193.4466 kJ/kg while in the ejector-expansion refrigeration cycle, and in ejector sub-cooled cycle, it increases from 111.5706 to 113.1995 kJ/kg and 187.588 to 205.0074 kJ/kg, respectively.

The effects of evaporator temperatures on the entrainment ratio of the ejector-expansion refrigeration cycle and ejector sub-cooled cycle using the studied refrigerant as working fluids are shown in Figure 12(a) and Figure 12(b), respectively.

Results revealed that the entrainment ratio in the ejector-expansion refrigeration cycle increases with increasing evaporation temperature for all the examined working fluids. This can be explained by the fact that when the evaporation temperatures increase from (-10 to 10°C), the primary mass

flow of the driving fluid decreases, and the secondary mass flow of the trapped fluid increases, thus the entrainment ratio in the ejection expansion cooling cycle increases.

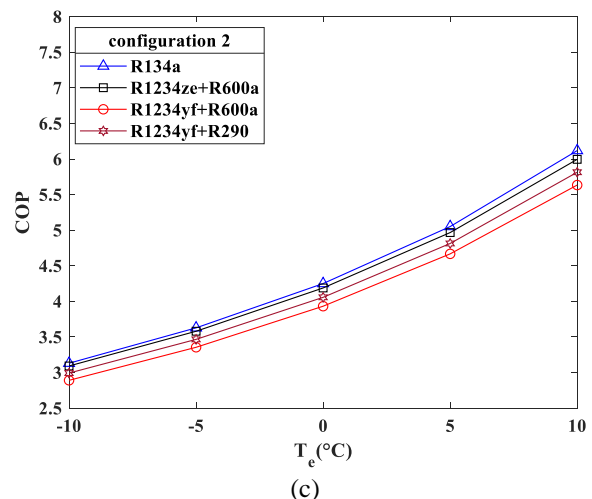
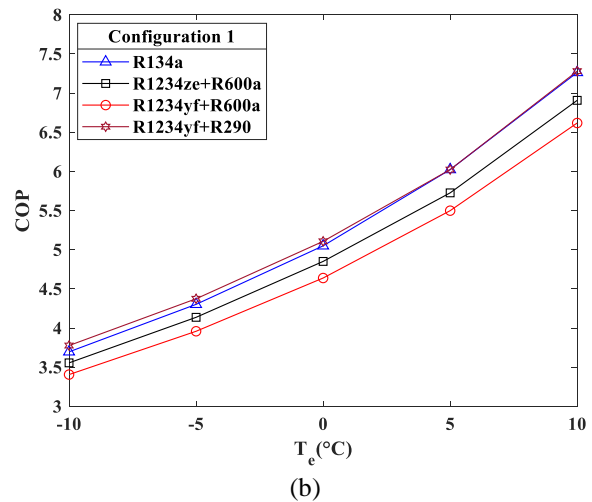
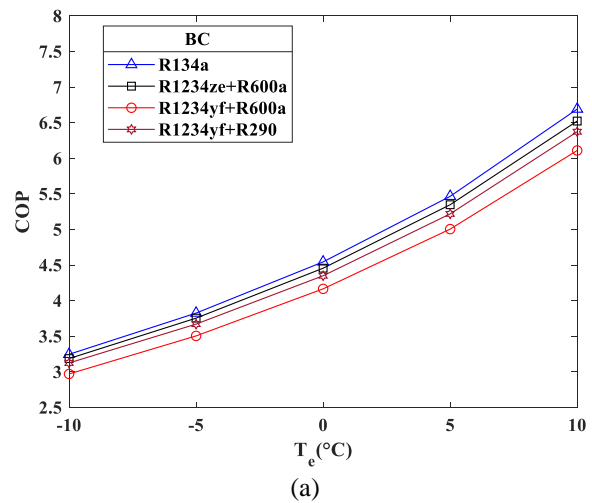


Figure 10. Influence of evaporating temperatures on the COP.

The effects of evaporator temperatures on the entrainment ratio of the ejector-expansion refrigeration cycle and ejector sub-cooled cycle using the studied refrigerant as working fluids are shown in Figure 12(a) and Figure 12(b), respectively.

Results revealed that the entrainment ratio in the ejector-expansion refrigeration cycle increases with increasing

evaporation temperature for all the examined working fluids. This can be explained by the fact that when the evaporation temperatures increase from (-10 to 10°C), the primary mass flow of the driving fluid decreases, and the secondary mass flow of the trapped fluid increases, thus the entrainment ratio in the ejection expansion cooling cycle increases.

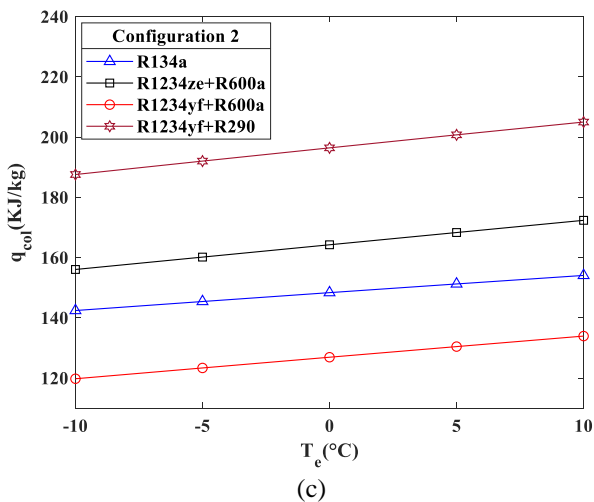
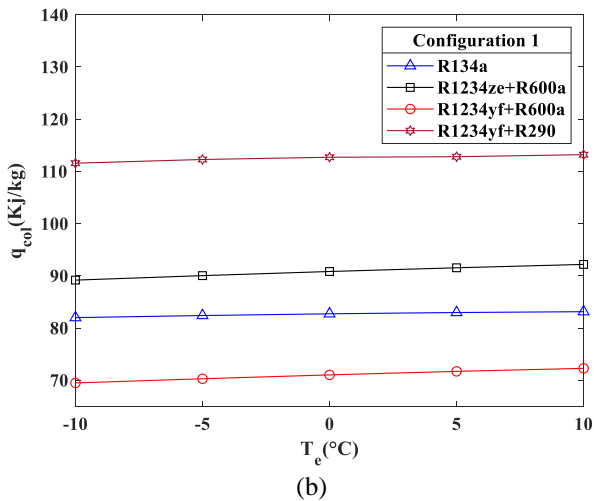
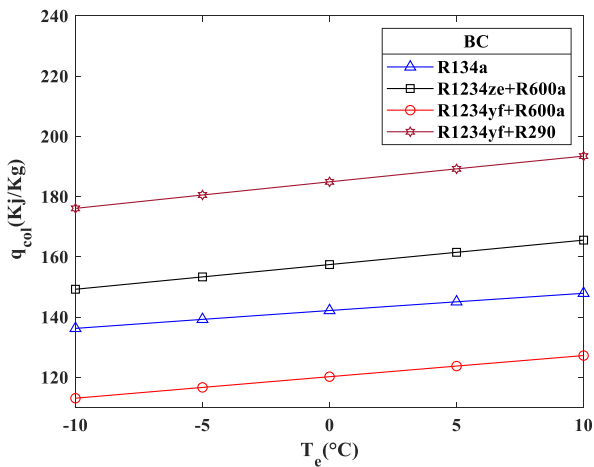


Figure 11. Influence of evaporating temperatures on the cooling capacity

However, for the ejector sub-cooled cycle (Figure 12(b)), the entrainment ratio remains constant because the evaporator has no direct interaction with the ejector.

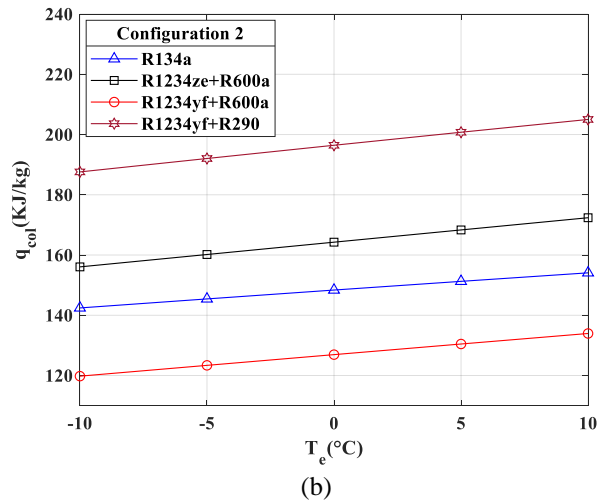
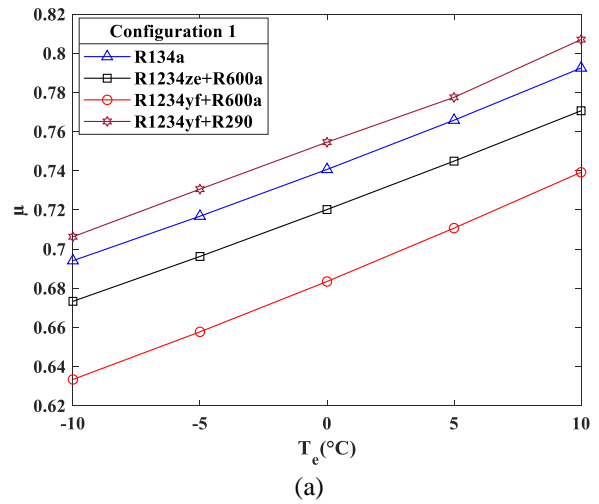


Figure 12. Influence of evaporating temperatures on entrainment ratio.

5. Conclusions

In this work, the performances of three eco-friendly azeotropic mixtures were compared with the usually used refrigerant R134a, which has good performances but is environmentally unfriendly with a great warming potential. The studied refrigerants were used as working fluid in three refrigeration cycles: basic cycle, ejector-expansion refrigeration cycle, and ejector sub-cooled cycle.

A numerical program was developed using MATLAB software to evaluate the coefficient of performance (COP), the cooling capacity, and the entrainment ratio of the studied cycles.

The refrigerants thermodynamic properties were obtained using REFPROP Version 9.0. The main conclusions are listed below

- The ejector expansion refrigeration cycle exhibits a high coefficient of performance compared to the basic cycle and ejector sub-cooled cycle;
- The ejector expansion refrigeration cycle exhibits a high entrainment ratio compared to the ejector sub-cooled cycle;
- The ejector sub-cooled cycle exhibits a high cooling capacity compared to the basic and cycle ejector expansion refrigeration cycle;
- There is a decrease in COP, cooling capacity, and entrainment ratio with the increase in condenser temperature for all studied cycles;

- There is an increase in COP and cooling capacity with the increase in evaporator temperature for the studied refrigeration cycles.
- The entrainment ratio increases with the evaporator temperature for the basic cycle and the ejector-expansion refrigeration cycle but remains constant for the ejector sub-cooled cycle.
- The eco-friendly azeotropic mixture R1234yf+R290 gives the best performances compared to the two other mixtures ;
- The performances of the eco-friendly azeotropic mixture R1234yf+R290 are close to those of R134a.

According to the obtained results, the azeotropic mixture R1234yf+R290 apart from its excellent environmental properties (GWP= 3.51) yields better performances in most of the cases, this confirms that it could be a suitable substitute for conventional working fluid R134a in the studied refrigeration systems.

Nomenclature

Symbols

h	Specific enthalpy [kJ kg^{-1}]
m	Mass flow rate [kg s^{-1}]
s	Specific entropy [$\text{kJ kg}^{-1} \text{K}^{-1}$]
u	Velocity [m s^{-1}]
Q_{col}	Cooling capacity [kJ kg^{-1}]
t_v	Throttle valve
W	Specific work [kJ kg^{-1}]
P	Pressure [kPa]
T	Temperature [$^{\circ}\text{C}$ or K]
x_d	Vapor quality
δp	Pressure drop [kPa]

Greek letters

μ	Entrainment ratio of ejector
η	Efficiency
Π	Compression ratio

Subscripts

$cond$	Condenser
D	Diffuser
c	Compressor
$evap$	Evaporator
p	Pompe
is	Isentropic process
in	Inlet
out	Outlet
$1-10, 9', 10'$	State point

Refrigerants name

R134a	1,1,1,2-tetrafluoroethene
R1234ze	trans-1,3,3,3-tetrafluoropropene
R600a	Isobutene
R1234yf	2,3,3,3-tetrafluoropropene
R290	propane

References:

[1] The European F-gas regulation. available: <https://eur-lex.europa.eu/legal-content/EN/TXT/?uri=CELEX%3A32024R0573&qid=1724340419698> (accessed March. 04, 2024).

[2] W. T. Tsai, "Environmental risks of new-generation fluorocarbons in replacement of potent greenhouse gases," *Int. J. Glob. Warm.*, vol. 5, no. 1, pp. 84–95,

2013, doi: 10.1504/IJGW.2013.051484.

[3] A. A. Kornhauser, "The Use Of An Ejector as Refrigerant Expander," in *IRACC 1990: Proceedings of the International Refrigeration and Air Conditioning Conference, Indiana*, pp. 10-19, 1990. doi: 10.1109/IECEC.1990.747930.

[4] M. Xing, G. Yan, and J. Yu, "Performance evaluation of an ejector subcooled vapor-compression refrigeration cycle," *Energy Convers. Manag.*, vol. 92, pp. 431–436, 2015, doi: <https://doi.org/10.1016/j.enconman.2014.12.091>.

[5] X. Yang, N. Zheng, L. Zhao, S. Deng, H. Li, and Z. Yu, "Analysis of a novel combined power and ejector-refrigeration cycle," *Energy Convers. Manag.*, vol. 108, pp. 266–274, Jan. 2016, doi: 10.1016/j.enconman.2015.11.019.

[6] M. Yari and M. Sirousazar, "Performance analysis of the ejector-vapour compression refrigeration cycle," *Proc. Inst. Mech. Eng. Part A J. Power Energy*, vol. 221, no. 8, pp. 1089–1098, Jan. 2007, doi: 10.1243/09576509JPE484.

[7] S. Disawas and S. Wongwises, "Experimental investigation on the performance of the refrigeration cycle using a two-phase ejector as an expansion device," *Int. J. Refrig.*, vol. 27, pp. 587–594, Sep. 2004, doi: 10.1016/j.ijrefrig.2004.04.002.

[8] J. Sarkar, "Ejector enhanced vapor compression refrigeration and heat pump systems - A review," *Renewable and Sustainable Energy Reviews*. vol. 16, pp. 6647–6659, Dec. 2012, doi: 10.1016/j.rser.2012.08.007.

[9] G. Besagni, R. Mereu, and F. Inzoli, "Ejector refrigeration: A comprehensive review," *Renew. Sustain. Energy Rev.*, vol. 53, pp. 373–407, 2016, doi: <https://doi.org/10.1016/j.rser.2015.08.059>.

[10] E. Nehdi, L. Kairouani, and M. Bouzaina, "Performance analysis of the vapour compression cycle using ejector as an expander," *Int. J. Energy Res.*, vol. 31, no. 4, pp. 364–375, Mar. 2007, doi: 10.1002/er.1260.

[11] Y. Maalem, S. Fedali, H. Madani, and Y. Tamene, "Performance analysis of ternary azeotropic mixtures in different vapor compression refrigeration cycles," *Int. J. Refrig.*, vol. 119, pp. 139–151, Nov. 2020, doi: 10.1016/j.ijrefrig.2020.07.021.

[12] J. Sarkar, "Performance characteristics of natural-refrigerants- based ejector expansion refrigeration cycles," *Proc. Inst. Mech. Eng. Part A J. Power Energy*, vol. 223, no. 1, pp. 543–550, May 2009, doi: 10.1243/09576509JPE753.

[13] N. Aisyah and H. M. Ariyadi, "Performance Evaluation of R1224yd as Alternative to R123 and R245fa for Vapor Compression Heat Pump System," *Int. J. Thermodyn.*, vol. 27, no. 5, pp. 13–21, 2024, doi: 10.5541/ijot.1310329.

[14] H. Rostamnejad and V. Zare, "Performance improvement of ejector expansion refrigeration cycles employing a booster compressor using different refrigerants: Thermodynamic analysis and optimization," *Int. J. Refrig.*, vol. 101, pp. 56–70, May. 2019, doi: 10.1016/j.ijrefrig.2019.02.031.

- [15] Z. Ma, X. Liu, H. Wang, H. Li, and X. Wang, "Off-Design Analysis of Hydrocarbon-based Ejector-Expansion Refrigeration Cycle," *J.Egy.Pro.*, vol. 105, pp. 4685–4690, May. 2017, doi: 10.1016/j.egypro.2017.03.1015.
- [16] Y. Maalem, Y. Tamene, and H. Madani, "Performances Investigation of the Eco-friendly Refrigerant R131I used as Working Fluid in the Ejector-Expansion Refrigeration Cycle," *Int. J. Thermodyn.*, vol. 26, no. 3, pp. 25–35, 2023, doi: 10.5541/ijot.1263939.
- [17] H. Li, F. Cao, X. Bu, L. Wang, and X. Wang, "Performance characteristics of R1234yf ejector-expansion refrigeration cycle," *Appl. Energy.*, vol. 121, pp. 96–1013 May. 2014, doi: 10.1016/j.apenergy.2014.01.079.
- [18] C. Lucas, J. Koehler, A. Schroeder, and C. Tischendorf, "Experimentally validated CO₂ ejector operation characteristic used in a numerical investigation of ejector cycle," *Int. J. Refrig.*, vol. 36, pp. 881–891 May. 2013, doi: 10.1016/j.ijrefrig.2012.10.035.
- [19] D. Calleja-Anta, M. Martínez-Ángeles, L. Nebot-Andres, D. Sánchez, and R. Llopis, "Experimental validation of RE170 / R600 (Dimethyl Ether / Butane) mixture as a superior refrigerant compared to R600a (Isobutane)," *Int. J. Refrig.*, vol. 168, pp. 208–219, 2024, doi: <https://doi.org/10.1016/j.ijrefrig.2024.08.008>.
- [20] L. Benbia, S. Fedali, C. Bougriou, and H. Madani, "Influence of azeotropic binary mixtures on single-stage refrigeration system performance," *High Temp. Press.*, vol. 51, no. 4, pp. 319–339, 2022, doi: 10.32908/hthp.v51.1185.
- [21] L. Zhao, X. Yang, S. Deng, H. Li, and Z. Yu, "Performance analysis of the ejector-expansion refrigeration cycle using zeotropic mixtures," *Int. J. Refrig.*, vol. 57, pp. 197–207 Sep. 2015, doi: 10.1016/j.ijrefrig.2015.05.006.
- [22] M. Mehemmai, H. Grine, M. Hakim, and C. Bougriou, "Performance analysis of ejector refrigeration cycle with zeotropic mixtures," *Int. J. Thermofluid Sci. Technol.*, vol. 10, no. 4, pp. 1–17, 2023.
- [23] C. Abdou, H. Madan, and A. Hasseine, "Study of the performances of an ejector refrigeration cycle using CO₂- based mixtures in subcritical and transcritical mode," *Int. J. Thermofluid Sci. Technol.*, vol. 10, no. 3, pp. 1–16, 2023.
- [24] B. Liu, X. Guo, X. Xi, J. Sun, B. Zhang, and Z. Yang, "Thermodynamic analyses of ejector refrigeration cycle with zeotropic mixture," *Energy*, vol. 263, p. 125989, 2023, doi: <https://doi.org/10.1016/j.energy.2022.125989>.
- [25] K. Sumeru, H. Nasution, and F. N. Ani, "A review on two-phase ejector as an expansion device in vapor compression refrigeration cycle," *Renew. Sustain. Energy Rev.*, vol. 16, no. 7, pp. 4927–4937, Sep. 2012, doi: 10.1016/j.rser.2012.04.058.
- [26] A. Khalil, M. Fatouh, and E. Elgandy, "Ejector design and theoretical study of R134a ejector refrigeration cycle," *Int. J. Refrig.*, vol. 34, no. 7, pp. 1684–1698, 2011, doi: 10.1016/j.ijrefrig.2011.01.005.
- [27] S. He, Y. Li, and R. Z. Wang, "Progress of mathematical modeling on ejectors," *Renew. Sustain. Energy Rev.*, vol. 13, no. 8, pp. 1760–1780, Oct. 2009, doi: 10.1016/j.rser.2008.09.032.

Research Article

Analysis of Thermodynamic Models for Liquid-Vapor Equilibrium: Evaluating Accuracy and Applicability

¹A.Zerfa , ^{2*}H. Madani , ³H. Grine , ⁴A. Beicha 

^{1,2,3}Laboratory of Studies on Industrial Energy Systems, Faculty of Technology, University of Batna 2, 05000 Batna, Algeria.

¹Laboratory of Sensors, Instrumentation and Process (LCIP). Faculty of Science and Technology, University of Khenchela, 04000 Khenchela, Algeria.

⁴Department of Process Engineering, Faculty of Technology, University of Batna 2, 05000 Batna, Algeria
E-mails: ¹zerfa.abdnour@yahoo.com, ^{2*}h.madani@univ-batna2.dz, ³grinehichem713@yahoo.com, ⁴a.beicha@univ-batna2.dz

Received 31 December 2023, Revised 15 May 2024, Accepted 9 July 2024

Abstract

This article investigates the liquid-vapor equilibrium of four binary refrigerant systems: R134a + R290, R152a + R1234ze, R152a + R1243zf, and R1243zf + R134a. The study employs three thermodynamic models for accurate predictions: the Peng-Robinson equation with the classical mixture rule of van der Waals (vdW) and the Wilson model, the PC-SAFT equation, and the PR-MC-WS-NRTL model. Activity coefficients are determined using the Peng-Robinson equation with vdW and the Wilson model. The PC-SAFT equation and the PR-MC-WS-NRTL model are also applied to model the data. The calculated results show good agreement with reference data. Favorable agreements exist between the calculated results and the reference data, with relative errors remaining below (0.15 and 0.42) % for the molar fraction and the pressure, respectively. This research provides valuable insights into the accuracy and applicability of different thermodynamic models in predicting liquid-vapor equilibrium within refrigerant systems.

Keywords: Equations of state; pc-saft; binary mixture; gwp; elv.

1. Introduction

The international community has long recognized the urgent need to address the environmental impact of refrigerants, leading to the establishment of various protocols aimed at mitigating their harmful effects. Notable among these are the Montreal Protocol and the Kyoto Protocol. Initiated in 1987, the Montreal Protocol focuses on the phase-out of ozone-depleting substances, including certain refrigerants. Its success in phasing out substances like chlorofluorocarbons (CFCs) has significantly contributed to the healing of the ozone layer. In contrast, the Kyoto Protocol targets greenhouse gas emissions, including those associated with certain refrigerants. By setting binding emission reduction targets for industrialized nations, it seeks to combat climate change. These protocols collectively represent global efforts to strike a balance between the essential role of refrigerants in daily life and the imperative to protect the environment.

Understanding the thermodynamic behavior of refrigerants is crucial in designing efficient cooling systems. The utilization of the PR (Peng-Robinson) equation of state holds particular relevance, enabling accurate modeling of the thermodynamic properties of refrigerants. Incorporating activity parameters, such as those derived from models like NRTL (Non-Random Two-Liquid) or the Wilson model, significantly enhances the

accuracy of thermodynamic predictions. These parameters account for non-ideal interactions among refrigerant molecules, thus considering the effects of non-ideality in mixtures. Additionally, the PC-SAFT (Perturbed Chain Statistical Associating Fluid Theory) approach provides an advanced alternative for modeling complex mixtures, offering an accurate representation of both liquid and gaseous phases. Integrating these models into cooling system designs allows optimization of energy performance and equipment reliability, contributing to more efficient and sustainable cooling solutions.

PC-SAFT (Perturbed-Chain Statistical Associating Fluid Theory) plays a pivotal role in the accurate prediction and calculation of liquid-vapor equilibrium, particularly in the realm of refrigerants and other complex fluids. It is a relatively new model that has been shown to be more accurate than traditional cubic equations of state such as Redlich-Kwong, Soave-Redlich-Kwong, and Peng-Robinson [1]. PC-SAFT takes into account the molecular structure of the fluids being modeled, allowing for better prediction of the behavior of mixtures with complex interactions. It has been used to model VLE in a variety of systems, including CO₂ mixtures [2], and deep eutectic solvents and ionic liquids [3]. To use PC-SAFT for VLE calculations, the mixture composition, density, and temperature are utilized as independent variables [1].

Researchers and engineers leverage PC-SAFT to explore the phase equilibria of refrigerants, enabling a comprehensive understanding of their thermodynamic properties. Recent studies, such as those by Gross and Sadowski [4] and Mollerup and Kontogeorgis [5], have demonstrated the effectiveness of PC-SAFT in providing precise predictions of phase behavior, critical points, and saturation properties. These references highlight the significance of PC-SAFT in advancing our comprehension of liquid-vapor equilibrium, paving the way for the development of environmentally sustainable cooling technologies.

The purpose of this study is to introduce a new simple calculation technique for predicting the binary interaction parameter [6] within the framework of the classical mixing rule. This technique aims to enhance the accuracy of isothermal (VLE) calculations in both subcritical and supercritical regions for various binary Refrigerant systems. Utilizing PR (with the incorporation of activity coefficients such as the Wilson and NRTL models) or PC-SAFT allows for a more accurate representation of non-ideal behavior, widely used in academic research.

The binary refrigerant systems considered in this study are: (R134a + R290) [7], (R152a + R1234ze (Z)) [8], (R152a + R1243zf) [8], and (R1243zf + R134a) [9]. These binary systems are noted for being environmentally friendly, possessing zero ozone depletion potential (ODP) and low global warming potential (GWP).

Tables 1 and 2 present the critical parameters, acentric factors, and environmental properties of the compounds in the binary blends, pure-component parameters for the PC-SAFT equation of state, and Mathias–Copeman coefficients.

Table 1. Critical parameters (T_c, P_c) and acentric factors (ω), ODP and GWP.

Compound	T_c/K	P_c/MPa	ω	ODP	GWP
R290	369.89	4.0593	0.1521	0	3
R1234ze	423.27	3.5330	0.327	0	<1
R1243zf	376.93	3.5182	0.261	0	<1
R134a	374.21	4.2512	0.327	0	1430
R152a	386.35	4.4990	0.226	0	124

2. Thermodynamic Models

In this study, we will use three different models to calculate the mole fractions of the liquid phase, the vapor phase, as well as the pressure.

2.1 Perturbed-Chain Statistical Fluid Theory. PC-SAFT Model

The first model is that of the PC-SAFT equation, which has demonstrated its capacity to predict the position of the azeotrope and determine the equilibrium values of liquid and vapour molar fractions. The equations have been described in previous works [10-11-12].

The PC-SAFT equation of state is a molecular-based model that considers molecules as chains of spherical segments. It represents the residual Helmholtz energy and incorporates various contributions. It's important to note that the terms of the equation of state corresponding to repulsive and dispersive effects require knowledge of three input parameters: the number of segments (m), the corresponding segment diameter (σ), and the segment dispersion energy parameter (ϵ/k). When dealing with mixtures, similar to cubic equations, it's necessary to define

combination rules for the cross parameters of σ and ϵ . If i and j denote two segments, the commonly used rules are referred to as Lorentz-Berthelot combination rules.

$$\begin{cases} \epsilon_{ij} = \sqrt{\epsilon_i \epsilon_j} (1 - k_{ij}) \\ \sigma_{ij} = \frac{\sigma_i + \sigma_j}{2} (1 - l_{ij}) \end{cases} \quad (1)$$

Where k_{ij} the adjustable binary interaction parameter is that can be fitted to experimental data for mixtures. In this model, the general definition of the Helmholtz energy is illustrated by

$$\begin{cases} \bar{a}^{\text{res}} = \bar{a}^{\text{seg}} + \bar{a}^{\text{chain}} + \bar{a}^{\text{assoc}} \\ P(T, v) = - \left(\frac{\partial \bar{a}^{\text{res}}}{\partial T} \right)_v \end{cases} \quad (2)$$

Where \bar{a}^{seg} is the Helmholtz energy of the segment, including both hard-sphere reference and dispersion terms,

This \bar{a}^{chain} is the contribution from chain formation and \bar{a}^{assoc} is the contribution of the associating interactions. Currently, most process simulators do not include association terms in their SAFT models.

2.2 PR-MC-WS-NRTL Model

PR-MC-WS-NRTL model was applied by our group [11-13-14] to correlate the experimental data. The model is based on the Peng-Robinson equation of state (PR EoS), the Mathias-Copeman (MC) alpha function, the Wong-Sandler (WS) mixing rules involving the NRTL (Non-Random Two Liquids) model.

2.3 PR-vdW-Wilson Model

The PR-EoS is given by the following form:

$$p = \frac{RT}{v-b} - \frac{\alpha(T)}{v^2 + 2vb - b^2} \quad (3)$$

$$\alpha_i(T) = 0.457235 \frac{R^2 T_{c,i}^2 \alpha_i(T)}{P_{c,i}} \quad (4)$$

$$b_i = 0.0077796 \frac{RT_{c,i}}{P_{c,i}} \quad (5)$$

Where their alpha-function, it is given by:

$$\alpha_i(T) = [1 + (0.37464 + 1.5422 \omega_i - 0.26992 \omega_i^2) \left(1 - \sqrt{\frac{T}{T_{c,i}}}\right)] \quad (6)$$

The fugacity coefficients in the liquid and vapor phases must be equal for the refrigerant blends to be in isothermal vapor-liquid equilibrium. The fugacity coefficient of species i can be expressed as follows when the Peng-Robinson Equation of State (PR-EoS) is used with the standard mixing rule (vdW) to forecast the isothermal vapor-liquid equilibrium:

$$\ln \phi_i^l = \frac{b_i}{b_m} (z - 1) - \ln \left[z \left(1 - \frac{b_m}{v} \right) \right] + \frac{a_m}{2.828RTb_m} \left(\frac{b_i}{b_m} - \frac{2}{a_m} \sum_j x_j a_{ij} \right) \ln \left(\frac{1 + 2.414 \frac{b_m}{v}}{1 - 0.414 \frac{b_m}{v}} \right) \quad (7)$$

The mixing rule of van der Waals (vdW) is as follows:

$$a_m = \sum_i \sum_j x_i x_j a_{ij} \quad (8)$$

$$b_m = \sum_i x_i b_i \quad (9)$$

With:

$$a_{ij} = (1 - k_{ij})\sqrt{a_i a_j} \quad (10)$$

Where $k_{ii} = 0$. $k_{ij} = k_{ji}$ is the binary interaction parameter.

The Wilson model is a thermodynamic model involving excess free enthalpy. It is a classic model used for predicting liquid-vapor equilibrium or estimating excess free enthalpy of miscible mixtures. In its initial form, the Wilson model ΔG^E expresses in the following expression:

$$\frac{G_m^E}{RT} = -\sum_i x_i \ln(1 - \sum_j x_j A_{ji}) \quad (11)$$

Where x_i is the mole fraction of species i and A_{ji} adjustable parameters such that $A_{ii} = 0$ and $A_{ij} \neq A_{ji} \neq 0$.

The activity coefficient is written as follows:

$$\ln \gamma_i = -\ln(1 - \sum_j x_j A_{ji}) + 1 - \sum_j [x_j(1 - A_{i/j}) / (1 - \sum_k x_k A_{k/j})] \quad (12)$$

3. Results and Discussion

Table 2. Vapor–liquid equilibrium pressures and phase compositions for the system (R134a + R290) [7], (R152a + R1234ze (Z)) [8], (R152a + R1243zf) [8], and (R1243zf + R134a) [9], Δx and ΔP are deviations in liquid and vapor mole fractions, Calculated values are from PC-SAFT, PR-MC-WS-NRTL, and PR-vdW-Wilson.

Experimental data			PC-SAFT				PR-vdW- WILSON				PR-MC-WS-NRTL			
P_{exp}/MPa	x_{1exp}	y_{1exp}	P_{cal}/MPa	y_{1cal}	$\Delta P/\text{MPa}$	Δy_1	P_{cal}/MPa	y_{1cal}	$\Delta P/\text{MPa}$	Δy_1	x_{1cal}	y_{1cal}	Δx_1	Δy_1
R134a + R290 [7]														
T = 253.15 K														
0.2441	0.0000	0.0000	0.2470	0.0000	0.0030	0.0000	0.2445	0.0000	-0.0004	0.0000	0.0000	0.0000	0.0000	0.0000
0.2686	0.0689	0.1418	0.2750	0.1500	0.0060	0.0080	0.2692	0.1417	-0.0006	0.0001	0.0694	0.1462	-0.0005	-0.0044
0.2844	0.1470	0.2375	0.2900	0.2340	0.0050	-0.0030	0.2844	0.2357	0.0000	0.0018	0.1460	0.2387	0.0010	-0.0012
0.2936	0.2517	0.3037	0.2960	0.2910	0.0030	-0.0120	0.2933	0.3101	0.0003	-0.0064	0.2502	0.3100	0.0015	-0.0063
0.2954	0.3482	0.3501	0.2970	0.3200	0.0010	-0.0300	0.2954	0.3525	0.0000	-0.0024	0.3510	0.3492	-0.0028	0.0010
0.2938	0.4719	0.3830	0.2940	0.3440	0.0000	-0.0390	0.2940	0.3882	-0.0002	-0.0052	0.4736	0.3774	-0.0017	0.0056
0.2883	0.6383	0.3892	0.2840	0.3800	-0.0040	-0.0090	0.2888	0.4195	-0.0005	-0.0303	0.6348	0.4031	0.0035	-0.0139
0.2570	0.8468	0.5130	0.2390	0.5000	-0.0180	-0.0130	0.2762	0.4561	-0.0192	0.0569	0.8548	0.4823	-0.0080	0.0307
0.1319	1.0000	1.0000	0.1320	1.0000	0.0010	0.0000	0.1327	1.0000	-0.0008	0.0000	1.0000	1.0000	0.0000	0.0000
T = 273.15 K														
0.4725	0.0000	0.0000	0.4780	0.0000	0.0060	0.0000	0.4745	0.0000	-0.0020	0.0000	0.0000	0.0000	0.0000	0.0000
0.5093	0.0516	0.1046	0.5180	0.1120	0.0090	0.0070	0.5155	0.1129	-0.0062	-0.0083	0.0523	0.1100	-0.0007	-0.0054
0.5430	0.1256	0.2105	0.5510	0.2080	0.0080	-0.0030	0.5521	0.2184	-0.0091	-0.0079	0.1251	0.2104	0.0007	0.0001
0.5668	0.2248	0.2913	0.5700	0.2800	0.0030	-0.0110	0.5766	0.3051	-0.0098	-0.0138	0.2242	0.2954	0.0006	-0.0041
0.5759	0.3449	0.3606	0.5740	0.3330	-0.0020	-0.0270	0.5866	0.3685	-0.0107	-0.0079	0.3453	0.3592	-0.0004	0.0014
0.5716	0.4951	0.4132	0.5660	0.3820	-0.0060	-0.0320	0.5847	0.4173	-0.0131	-0.0041	0.4942	0.4107	0.0010	0.0025
0.5542	0.6585	0.4459	0.5400	0.4400	-0.0150	-0.0060	0.5737	0.4541	-0.0195	-0.0082	0.6550	0.4576	0.0035	-0.0117
0.5136	0.8035	0.5300	0.4840	0.5330	-0.0290	0.0030	0.5540	0.4896	-0.0404	0.0404	0.8067	0.5243	-0.0028	0.0057
0.2938	1.0000	1.0000	0.2890	1.0000	-0.0040	0.0000	0.2928	1.0000	0.0010	0.0000	1.0000	1.0000	0.0000	0.0000

Table 2. Vapor–liquid equilibrium pressures and phase compositions for the system (R134a + R290) [7], (R152a + R1234ze (Z)) [8], (R152a + R1243zf) [8], and (R1243zf + R134a) [9], Δx and ΔP are deviations in liquid and vapor mole fractions, Calculated values are from PC-SAFT, PR-MC-WS-NRTL, and PR-vdW-Wilson“(continue)”.

Three models (PC-SAFT, PR-MC-WS-NRTL, and PR-vdW-Wilson) have been proposed for the calculation of liquid and vapor mole fractions, as well as pressure. The critical temperature, critical pressure, and acentric factor of pure components, and the PC-SAFT parameter values of the selected compounds used in this study, are provided in Table 1, sourced from literature cited in the references.

The experimental and calculated compositions and pressures of the binary mixtures using (PC-SAFT), (PR-MC-WS-NRTL) model, and (PR-vdW-Wilson) model, respectively, are presented in Table 2 and implemented in Figures 1 through.

The parameters of (PC-SAFT), (PR-MC-WS-NRTL), and (PR-vdW-Wilson) models were obtained by minimizing the following objectivefunction:

$$F_{obj} = \frac{100}{N} \left[\sum_1^N \left(\frac{P_{exp} - P_{cal}}{P_{exp}} \right)^2 + \sum_1^N \left(\frac{z_{exp} - z_{cal}}{z_{exp}} \right)^2 \right] \quad (13)$$

In order to assess the goodness of fit of our method, the deviations MRD (Mean Relative Deviation), and the Bias, applied on liquid and vapour phase mole fractions for mixtures, or pressure are calculated using Eq. (14) and Eq. (15) respectively:

$$MRD = \frac{100}{N} \sum |((U_{exp} - U_{cal})/U_{exp})| \quad (14)$$

T = 293.15 K														
0.8365	0.0000	0.0000	0.8420	0.0000	0.0060	0.0000	0.8365	0.0000	0.0000	0.0000	0.0000	0.0000	0.0000	0.0000
0.8942	0.0508	0.0967	0.9070	0.1020	0.0130	0.0060	0.9015	0.1036	-0.0073	-0.0069	0.0521	0.1011	-0.0013	-0.0044
0.9500	0.1208	0.1962	0.9630	0.1940	0.0130	-0.0020	0.9597	0.2029	-0.0097	-0.0067	0.1207	0.1962	0.0001	0.0000
0.9729	0.1616	0.2379	0.9840	0.2330	0.0110	-0.0050	0.9820	0.2460	-0.0091	-0.0081	0.1603	0.2384	0.0013	-0.0005
0.9971	0.2199	0.2859	1.0020	0.2770	0.0050	-0.0090	1.0034	0.2950	-0.0063	-0.0091	0.2196	0.2894	0.0003	-0.0035
1.0197	0.5370	0.3684	1.0160	0.3450	-0.0040	-0.0230	1.0229	0.3691	-0.0032	-0.0007	0.3455	0.3677	-0.0002	0.0007
1.0088	0.7359	0.5069	0.9930	0.4270	-0.0160	-0.0230	1.0158	0.4413	-0.0070	0.0656	0.5321	0.4489	0.0016	0.0005
0.9241	0.8860	0.6741	0.8830	0.5640	-0.0420	0.0050	0.9585	0.5292	-0.0344	0.1449	0.7719	0.5611	-0.0006	-0.0013
0.5717	1.0000	1.0000	0.5640	1.0000	-0.0080	0.0000	0.5717	1.0000	0.0000	0.0000	1.0000	1.0000	0.0000	0.0000
R152a + R1234ze [8]														
T = 273.15 K														
0.2166	0.0000	0.0000	0.2140	0.0000	-0.0030	0.0000	0.2165	0.0000	0.0001	0.0000	0.0000	0.0000	0.0000	0.0000
0.2185	0.0385	0.0503	0.2170	0.0490	-0.0020	-0.0010	0.2222	0.0579	-0.0037	-0.0076	0.0444	0.0624	-0.0059	-0.0121
0.2261	0.1453	0.1778	0.2240	0.1790	-0.0020	0.0010	0.2333	0.1870	-0.0072	-0.0092	0.1483	0.1843	-0.0030	-0.0065
0.2308	0.2306	0.2710	0.2290	0.2760	-0.0010	0.0050	0.2394	0.2752	-0.0086	-0.0042	0.2284	0.2700	0.0023	0.0010
0.2379	0.3639	0.4111	0.2370	0.4180	0.0000	0.0060	0.2465	0.4047	-0.0086	0.0064	0.3640	0.4113	-0.0001	-0.0001
0.2446	0.4863	0.5296	0.2440	0.5390	0.0000	0.0090	0.2514	0.5215	-0.0068	0.0081	0.4933	0.5432	-0.0070	-0.0136
0.2507	0.6311	0.6665	0.2520	0.6740	0.0010	0.0080	0.2559	0.6595	-0.0052	0.0070	0.6099	0.6580	0.0213	0.0085
0.2547	0.7325	0.7567	0.2570	0.7650	0.0020	0.0080	0.2585	0.7556	-0.0038	0.0011	0.6982	0.7446	0.0343	0.0121
0.2592	0.8479	0.8639	0.2610	0.8670	0.0020	0.0030	0.2611	0.8632	-0.0019	0.0007	0.8146	0.8559	0.0333	0.0080
0.2623	0.9537	0.9573	0.2660	0.9590	0.0030	0.0020	0.2631	0.9592	-0.0008	-0.0019	0.9191	0.9555	0.0346	0.0018
0.2636	1.0000	1.0000	0.2670	1.0000	0.0040	0.0000	0.2640	1.0000	-0.0004	0.0000	1.0000	1.0000	0.0000	0.0000
T = 293.15 K														
0.4273	0.0000	0.0000	0.4220	0.0000	-0.0050	0.0000	0.4273	0.0000	0.0000	0.0000	0.0000	0.0000	0.0000	0.0000
0.4318	0.0386	0.0486	0.4270	0.0480	-0.0050	0.0000	0.4322	0.0481	-0.0004	0.0005	0.0436	0.0578	-0.0050	-0.0092
0.4441	0.1443	0.1725	0.4400	0.1740	-0.0040	0.0010	0.4448	0.1730	-0.0007	-0.0005	0.1427	0.1763	0.0016	-0.0038
0.4545	0.2299	0.2661	0.4500	0.2700	-0.0050	0.0040	0.4543	0.2678	0.0002	-0.0017	0.2279	0.2681	0.0020	-0.0020
0.4681	0.3625	0.4033	0.4650	0.4090	-0.0040	0.0060	0.4678	0.4058	0.0003	-0.0025	0.3625	0.4037	0.0000	-0.0004
0.4784	0.4844	0.5239	0.4770	0.5300	-0.0010	0.0060	0.4789	0.5253	-0.0005	-0.0014	0.4790	0.5168	0.0054	0.0071
0.4900	0.6308	0.6623	0.4900	0.6680	0.0000	0.0060	0.4908	0.6625	-0.0008	-0.0002	0.6324	0.6635	-0.0016	-0.0012
0.4974	0.7329	0.7557	0.4990	0.7610	0.0010	0.0050	0.4980	0.7557	-0.0006	0.0000	0.7301	0.7561	0.0028	-0.0004
0.5054	0.8478	0.8613	0.5080	0.8640	0.0020	0.0020	0.5052	0.8600	0.0002	0.0013	0.8354	0.8546	0.0124	0.0067
0.5102	0.9536	0.9569	0.5150	0.9580	0.0040	0.0010	0.5108	0.9569	-0.0006	0.0000	0.9396	0.9553	0.0140	0.0016
0.5124	1.0000	1.0000	0.5170	1.0000	0.0050	0.0000	0.5129	1.0000	-0.0005	0.0000	1.0000	1.0000	0.0000	0.0000
T = 313.15 K														
0.7665	0.0000	0.0000	0.7570	0.0000	-0.0100	0.0000	0.7665	0.0000	0.0000	0.0000	0.0000	0.0000	0.0000	0.0000
0.7735	0.0385	0.0474	0.7660	0.0470	-0.0080	0.0000	0.7752	0.0469	-0.0017	0.0005	0.0430	0.0543	-0.0045	-0.0069
0.7967	0.1441	0.1689	0.7880	0.1700	-0.0080	0.0010	0.7975	0.1689	-0.0008	0.0000	0.1522	0.1816	-0.0081	-0.0127
0.8125	0.2286	0.2609	0.8060	0.2630	-0.0070	0.0030	0.8137	0.2606	-0.0012	0.0003	0.2293	0.2645	-0.0007	-0.0036
0.8359	0.3623	0.3996	0.8310	0.4030	-0.0050	0.0030	0.8367	0.3979	-0.0008	0.0017	0.3628	0.3999	-0.0005	-0.0003
0.8520	0.4847	0.5174	0.8520	0.5230	0.0000	0.0060	0.8551	0.5175	-0.0031	-0.0001	0.4705	0.5047	0.0142	0.0127
0.8726	0.6301	0.6584	0.8740	0.6610	0.0010	0.0020	0.8740	0.6549	-0.0014	0.0035	0.6307	0.6568	-0.0006	0.0017
0.8847	0.7319	0.7506	0.8870	0.7540	0.0020	0.0040	0.8856	0.7496	-0.0009	0.0010	0.7378	0.7571	-0.0059	-0.0065
R152a + R1234ze (Z) [8]														
0.8961	0.8474	0.8585	0.9000	0.8600	0.0040	0.0010	0.8969	0.8568	-0.0008	0.0017	0.8477	0.8594	-0.0003	-0.0008

Table 2. Vapor–liquid equilibrium pressures and phase compositions for the system (R134a + R290) [7], (R152a + R1234ze (Z)) [8], (R152a + R1243zf) [8], and (R1243zf + R134a) [9], Δx and ΔP are deviations in liquid and vapor mole fractions, Calculated values are from PC-SAFT, PR-MC-WS-NRTL, and PR-vdW-Wilson“(continue)”.

0.9049	0.9535	0.9566	0.9100	0.9570	0.0050	0.0000	0.9058	0.9560	-0.0009	0.0006	0.9501	0.9551	0.0034	0.0016
0.9082	1.0000	1.0000	0.9140	1.0000	0.0060	0.0000	0.9093	1.0000	-0.0011	0.0000	1.0000	1.0000	0.0000	0.0000
R152a + R1243zf [8]														
T =273.15 K														
0.2682	0.0000	0.0000	0.2690	0.0000	0.0010	0.0000	0.2695	0.0000	-0.0013	0.0000	0.0000	0.0000	0.0000	0.0000
0.2704	0.0837	0.0902	0.2710	0.0890	0.0000	-0.0010	0.2710	0.0880	-0.0006	0.0022	0.0815	0.0870	0.0022	0.0033
0.2735	0.2127	0.2200	0.2730	0.2210	0.0000	0.0010	0.2726	0.2171	0.0009	0.0029	0.2088	0.2164	0.0039	0.0037
0.2744	0.3103	0.3134	0.2740	0.3170	0.0000	0.0040	0.2732	0.3113	0.0012	0.0021	0.3074	0.3119	0.0029	0.0016
0.2747	0.4082	0.4093	0.2750	0.4120	0.0000	0.0030	0.2733	0.4043	0.0014	0.0050	0.4080	0.4088	0.0002	0.0005
0.2750	0.5073	0.5029	0.2750	0.5070	0.0000	0.0040	0.2729	0.4981	0.0021	0.0048	0.5067	0.5035	0.0006	-0.0006
0.2742	0.5961	0.5885	0.2750	0.5920	0.0000	0.0030	0.2722	0.5827	0.0020	0.0058	0.5979	0.5923	-0.0018	-0.0038
0.2734	0.6891	0.6763	0.2750	0.5850	0.0010	-0.0910	0.2710	0.6729	0.0024	0.0034	0.6874	0.6785	0.0017	-0.0022
0.2710	0.8159	0.8000	0.2720	0.8060	0.0010	0.0060	0.2688	0.8003	0.0022	-0.0003	0.8139	0.8015	0.0020	-0.0015
0.2674	0.9206	0.9094	0.2690	0.9190	0.0020	0.0100	0.2663	0.9112	0.0011	-0.0018	0.9235	0.9137	0.0024	-0.0042
0.2636	1.0000	1.0000	0.2670	1.0000	0.0040	0.0000	0.2640	1.0000	-0.0004	0.0000	1.0000	1.0000	0.0000	0.0000
T =293.15 K														
0.5077	0.0000	0.0000	0.5080	0.0000	0.0010	0.0000	0.5100	0.0000	-0.0023	0.0000	0.0000	0.0000	0.0000	0.0000
0.5129	0.0824	0.0910	0.5130	0.0890	0.0000	-0.0020	0.5182	0.0913	-0.0053	-0.0003	0.0867	0.1242	-0.0043	-0.0332
0.5186	0.2125	0.2218	0.5200	0.2240	0.0010	0.0030	0.5250	0.2180	-0.0064	0.0038	0.2172	0.2234	-0.0047	-0.0016
0.5218	0.3094	0.3176	0.5230	0.3210	0.0010	0.0040	0.5270	0.3082	-0.0052	0.0094	0.3135	0.3144	-0.0041	0.0032
0.5241	0.4088	0.4130	0.5260	0.4180	0.0020	0.0050	0.5274	0.4009	-0.0033	0.0121	0.4109	0.4146	-0.0021	-0.0016
0.5254	0.5070	0.5083	0.5280	0.5120	0.0020	0.0030	0.5266	0.4943	-0.0012	0.0140	0.5077	0.5143	-0.0007	-0.0060
0.5253	0.5959	0.5948	0.5280	0.5960	0.0030	0.0410	0.5250	0.5809	0.0003	0.0139	0.5954	0.6021	0.0005	-0.0072
0.5248	0.6889	0.6824	0.5280	0.6850	0.0030	0.0030	0.5229	0.6738	0.0019	0.0086	0.6857	0.6894	0.0032	-0.0070
0.5225	0.8156	0.8057	0.5250	0.8080	0.0030	0.0030	0.5192	0.8040	0.0033	0.0017	0.8110	0.8107	0.0047	-0.0050
0.5169	0.9203	0.9122	0.5210	0.9150	0.0040	0.0020	0.5157	0.9145	0.0012	-0.0023	0.9117	0.9163	0.0086	-0.0041
0.5124	1.0000	1.0000	0.5170	1.0000	0.0050	0.0000	0.5129	1.0000	-0.0005	0.0000	1.0000	1.0000	0.0000	0.0000
T =313.15 K														
0.8809	0.0000	0.0000	0.8810	0.0000	0.0000	0.0000	0.8843	0.0000	-0.0034	0.0000	0.0000	0.0000	0.0000	0.0000
0.8906	0.0831	0.0916	0.8910	0.0900	0.0000	-0.0020	0.8999	0.0899	-0.0093	0.0017	0.0874	0.1056	-0.0043	-0.0140
0.9033	0.2121	0.2224	0.9030	0.2250	0.0000	0.0020	0.9134	0.2150	-0.0101	0.0074	0.2173	0.2419	-0.0051	-0.0195
0.9106	0.3098	0.3194	0.9110	0.3230	0.0000	0.0030	0.9185	0.3068	-0.0079	0.0126	0.3146	0.3357	-0.0048	-0.0163
0.9156	0.4075	0.4161	0.9170	0.4190	0.0010	0.0030	0.9209	0.3995	-0.0053	0.0166	0.4118	0.4268	-0.0043	-0.0107
0.9199	0.5079	0.5149	0.9210	0.5160	0.0010	0.0010	0.9213	0.4969	-0.0014	0.0180	0.5114	0.5190	-0.0035	-0.0041
0.9218	0.5959	0.5976	0.9240	0.6000	0.0020	0.0020	0.9205	0.5841	0.0013	0.0135	0.5968	0.5987	-0.0009	-0.0011
0.9215	0.6898	0.6881	0.9250	0.6900	0.0030	0.0020	0.9187	0.6791	0.0028	0.0090	0.6890	0.6868	0.0009	0.0013
0.9201	0.8153	0.8095	0.9230	0.8120	0.0030	0.0020	0.9153	0.8082	0.0048	0.0013	0.8124	0.8070	0.0029	0.0025
0.9138	0.9200	0.9150	0.9190	0.9170	0.0050	0.0020	0.9120	0.9169	0.0018	-0.0019	0.9186	0.9163	0.0014	-0.0013
0.9082	1.0000	1.0000	0.9140	1.0000	0.0060	0.0000	0.9093	1.0000	-0.0011	0.0000	1.0000	1.0000	0.0000	0.0000
R1243zf + R134a [9]														
T =243.15 K														
0.0845	0.0000	0.0000	0.0840	0.0000	-0.0010	0.0000	0.0843	0.0000	-0.0843	0.0000	0.0000	0.0000	0.0000	0.0000
0.0855	0.1640	0.1770	0.0860	0.1770	0.0000	0.0000	0.0858	0.1751	-0.0858	0.0019	0.1674	0.1730	-0.0034	0.0040

Table 2. Vapor–liquid equilibrium pressures and phase compositions for the system (R134a + R290) [7], (R152a + R1234ze (Z)) [8], (R152a + R1243zf) [8], and (R1243zf + R134a) [9], Δx and ΔP are deviations in liquid and vapor mole fractions, Calculated values are from PC-SAFT, PR-MC-WS-NRTL, and PR-vdW-Wilson“(continue)”.

0.0861	0.2310	0.2460	0.0860	0.2440	0.0000	-0.0020	0.0863	0.2427	-0.0863	0.0033	0.2385	0.2410	-0.0075	0.0051
--------	--------	--------	--------	--------	--------	---------	--------	--------	---------	--------	--------	--------	---------	--------

0.0869	0.3620	0.3670	0.0870	0.3680	0.0000	0.0010	0.0869	0.3699	-0.0869	-0.0029	0.3645	0.3564	-0.0025	0.0106
0.0866	0.4760	0.4750	0.0870	0.4740	0.0000	-0.0010	0.0870	0.4770	-0.0870	-0.0020	0.4755	0.4604	0.0005	0.0146
0.0866	0.5820	0.5800	0.0870	0.5720	0.0000	-0.0080	0.0869	0.5755	-0.0869	0.0045	0.5810	0.5586	0.0010	0.0214
0.0857	0.6740	0.6530	0.0860	0.6590	0.0000	0.0060	0.0865	0.6615	-0.0865	-0.0085	0.6635	0.6420	0.0105	0.0110
0.0846	0.8230	0.8040	0.0850	0.8060	0.0000	0.0020	0.0854	0.8064	-0.0854	-0.0024	0.8135	0.7852	0.0095	0.0188
0.0835	0.9120	0.8930	0.0840	0.9010	0.0000	0.0080	0.0843	0.8995	-0.0843	-0.0065	0.9025	0.8515	0.0095	0.0415
0.0819	1.0000	1.0000	0.0830	1.0000	0.0010	0.0000	0.0828	1.0000	-0.0828	0.0000	1.0000	1.0000	0.0000	0.0000
T = 263.15 K														
0.2010	0.0000	0.0000	0.1990	0.0000	-0.0020	0.0000	0.2006	0.0000	-0.2006	0.0000	0.0000	0.0000	0.0000	0.0000
0.2020	0.1630	0.1670	0.2010	0.1690	-0.0010	0.0020	0.2014	0.1634	-0.2014	0.0036	0.1630	0.1671	0.0000	-0.0001
0.2030	0.2440	0.2460	0.2010	0.2470	-0.0010	0.0010	0.2016	0.2436	-0.2016	0.0024	0.2450	0.2427	-0.0010	0.0033
0.2030	0.3510	0.3490	0.2010	0.3480	-0.0010	-0.0010	0.2016	0.3482	-0.2016	0.0008	0.3500	0.3335	0.0010	0.0155
0.2020	0.4660	0.4550	0.2010	0.4540	-0.0010	-0.0010	0.2011	0.4590	-0.2011	-0.0040	0.4605	0.4285	0.0055	0.0265
0.2010	0.5640	0.5480	0.2000	0.5460	-0.0010	-0.0020	0.2002	0.5526	-0.2002	-0.0046	0.5560	0.5157	0.0080	0.0323
0.1980	0.7060	0.6830	0.1970	0.6830	-0.0010	0.0000	0.1981	0.6885	-0.1981	-0.0055	0.6945	0.6642	0.0115	0.0188
0.1960	0.8060	0.7850	0.1940	0.7840	-0.0020	-0.0010	0.1958	0.7868	-0.1958	-0.0018	0.7955	0.7760	0.0105	0.0090
0.1920	0.8910	0.8760	0.1920	0.8750	0.0000	-0.0010	0.1931	0.8748	-0.1931	0.0012	0.8924	0.8718	-0.0014	0.0042
0.1870	1.0000	1.0000	0.1880	1.0000	0.0010	0.0000	0.1881	1.0000	-0.1881	0.0000	1.0000	1.0000	0.0000	0.0000
T = 283.15 K														
0.4140	0.0000	0.0000	0.4090	0.0000	-0.0050	0.0000	0.4146	0.0000	-0.4146	0.0000	0.0000	0.0000	0.0000	0.0000
0.4150	0.1630	0.1630	0.4120	0.1640	-0.0030	0.0010	0.4157	0.1635	-0.4157	-0.0005	0.1603	0.1630	0.0027	0.0000
0.4150	0.2450	0.2410	0.4120	0.2430	-0.0030	0.0020	0.4153	0.2422	-0.4153	-0.0012	0.2470	0.2430	-0.0020	-0.0020
0.4130	0.3580	0.3470	0.4100	0.3480	-0.0030	0.0010	0.4137	0.3485	-0.4137	-0.0015	0.3737	0.3525	-0.0157	-0.0055
0.4090	0.4680	0.4400	0.4080	0.4500	-0.0010	0.0100	0.4108	0.4507	-0.4108	-0.0017	0.4699	0.4373	-0.0019	0.0027
0.4060	0.5660	0.5420	0.4040	0.5410	-0.0020	-0.0010	0.4071	0.5423	-0.4071	-0.0003	0.5540	0.5160	0.0120	0.0260
0.3980	0.7110	0.6800	0.3960	0.6820	-0.0010	0.0020	0.3996	0.6819	-0.3996	-0.0019	0.6955	0.6666	0.0155	0.0134
0.3920	0.8060	0.7820	0.3900	0.7800	-0.0020	-0.0020	0.3932	0.7786	-0.3932	0.0034	0.7940	0.7806	0.0120	0.0014
0.3850	0.8770	0.8600	0.3850	0.8570	0.0000	-0.0030	0.3874	0.8550	-0.3874	0.0050	0.8743	0.8685	0.0027	-0.0085
0.3740	1.0000	1.0000	0.3740	1.0000	0.0010	0.0000	0.3754	1.0000	-0.3754	0.0000	1.0000	1.0000	0.0000	0.0000

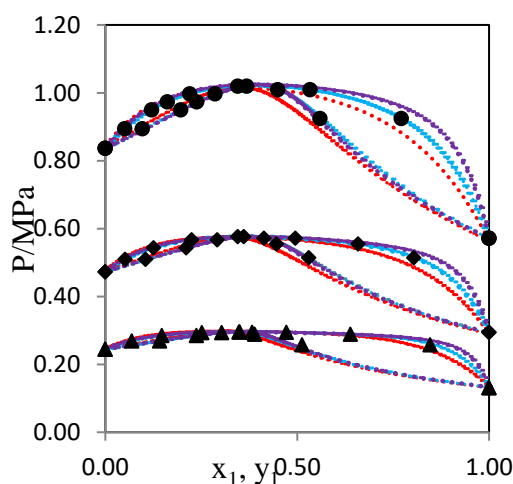


Figure 1. VLE for the system R134a + R290 [7] at different temperatures: (\blacktriangle) 253.15 K. (\blacklozenge) 273.15 K. (\bullet) 293.15 K; PC-SAFT model. PR-MC-WS-NRTL model. PR-vdW- Wilson model.

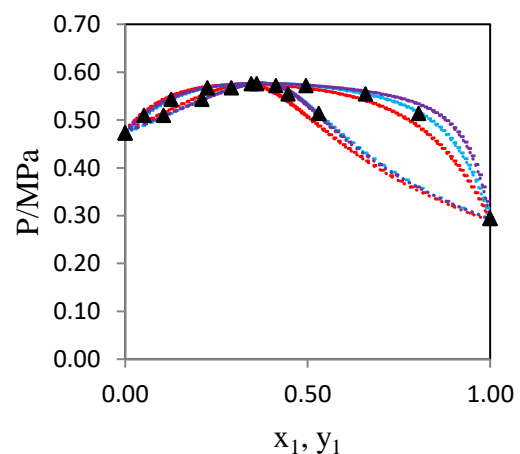


Figure 2. VLE for the system R134a + R290 [7] at (\blacktriangle) 273.15 K. PC-SAFT model. PR-MC-WS-NRTL model. PR-vdW- Wilson model.

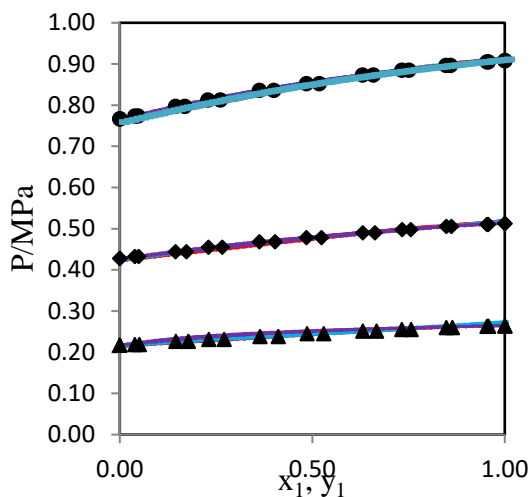


Figure 3. VLE for the system R152a + R1234ze[8] at different temperatures: (▲) 273.15 K. (◆) 293.15 K. (●) 313.15 K, PC-SAFT model. PR-MC-WS-NRTL model. PR-vdW- Wilson model.

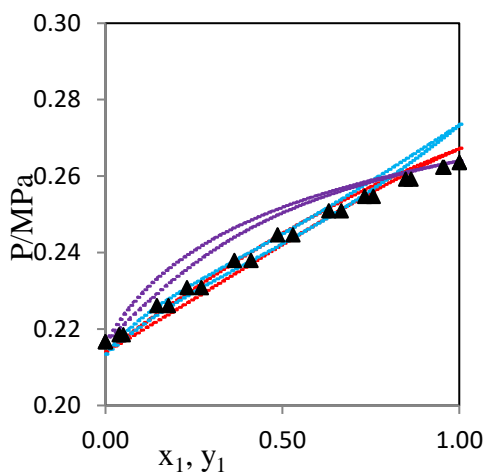


Figure 4. VLE for the system R152a + R1234ze [8] at (▲) 273.15 K, PC-SAFT model. PR-MC-WS-NRTL model. PR-vdW- Wilson model.

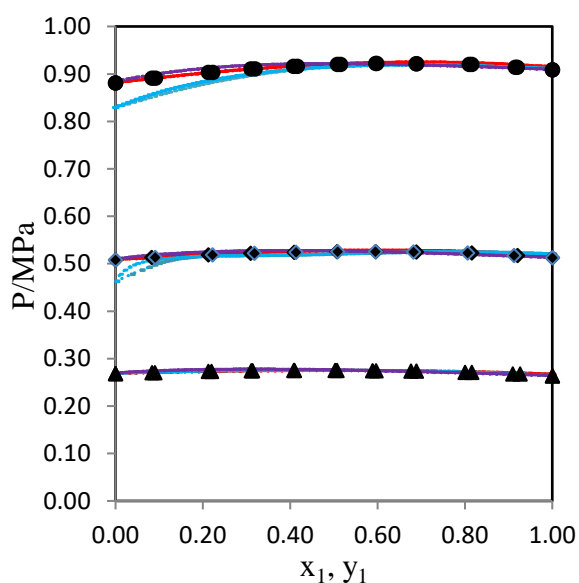


Figure 5. VLE for the system R152a + R1243zf[8] at different temperatures: (▲) 273.15 K. (◆) 293.15 K. (●) 313.15 K, PC-SAFT model. PR-MC-WS-NRTL model. PR-vdW- Wilson model.

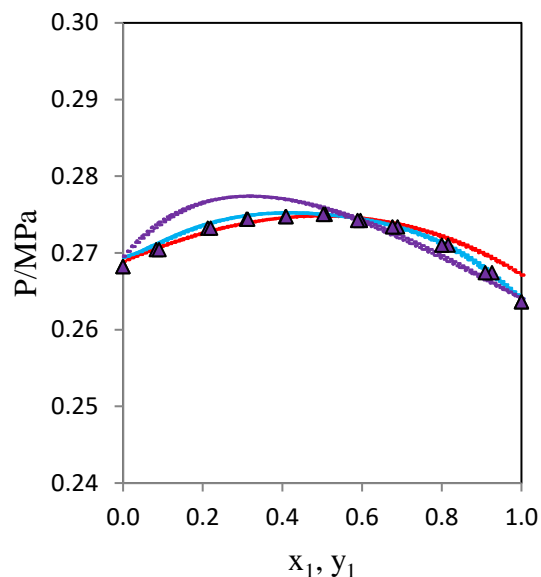


Figure 6. VLE for the system R152a + R1243zf[8] at (▲) 273.15 K, PC-SAFT model. PR-MC-WS-NRTL model. PR-vdW- Wilson model.

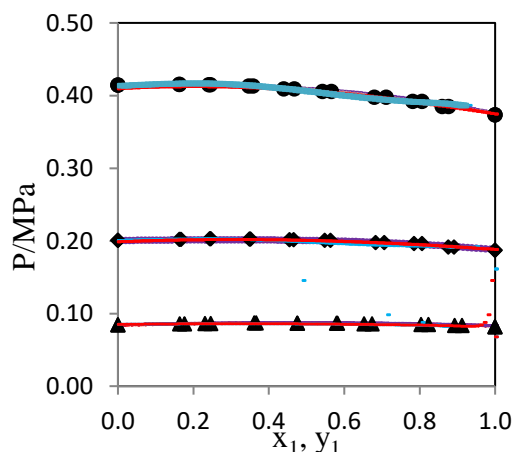


Figure 7. VLE for the system R1243zf + R134a[9] at different temperatures: (▲) 243.15 K. (◆) 263.15 K. (●) 283.15 K; PC-SAFT model. PR-MC-WS-NRTL model. PR-vdW- Wilson model.

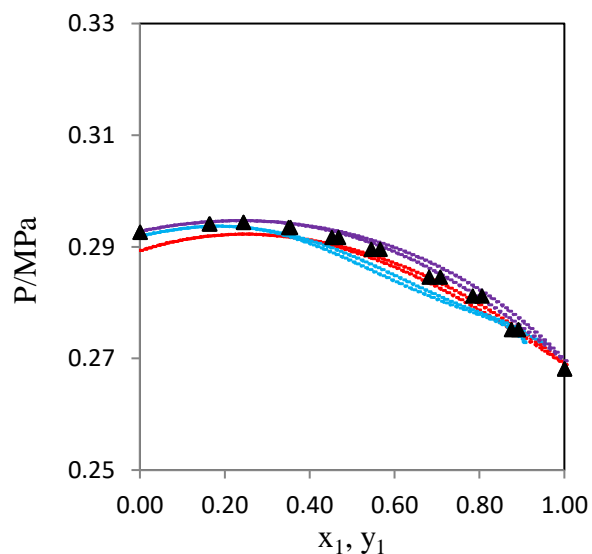


Figure 8. VLE for the system R1243zf + R134a [9] at (▲) 273.15 K, PC-SAFT model. PR-MC-WS-NRTL model. PR-vdW- Wilson model.

Table 3. Pure-component parameters for the PC-SAFT equation of state.

m_1	m_2	m_3	σ_1 [Å]	σ_2 [Å]	σ_3 [Å]	$(\epsilon/k)_1$ (K)	$(\epsilon/k)_2$ (K)	$(\epsilon/k)_3$ (K)
R134a + R290 [7]								
3.54	2.12	2.26	3.09	3.63	3.76	160.60	199.46	216.53
R152a + R1234ze [8]								
3.06	3.43	2.26	3.17	3.26	3.76	176.20	166.18	216.53
R152a + R1243zf [8]								
3.06	2.99	2.26	3.17	3.45	3.76	176.21	173.56	216.53
R1243zf + R134a [9]								
2.99	3.54	2.26	3.45	3.09	3.76	173.56	160.60	216.53

Table 4. Mathias–Copeman coefficients.

Coefficients	R134a	R290	R152a	R1234ze	R1243zf
C_1	0.850	0.600	0.835	0.861	0.850
C_2	0.007	-0.006	-0.631	-0.240	0.007
C_3	-0.054	0.174	0.790	0.602	-0.054

$$\text{Bias} = \frac{100}{N} \sum ((U_{\text{exp}} - U_{\text{cal}}) / U_{\text{exp}}) \quad (15)$$

Where N is the number of data points, and $U = x_i y_i$ or P.

Figures (1-8) illustrate the variation of pressure as a function of the mole fraction of the most volatile pure component at different isotherms for the four binary systems: R134a + R290, 152a + R1234ze, R152a + R1243zf, and R1243zf + R134a, respectively. The curves represented by symbols depict the experimental values extracted from the literature, while the dashed curves in different colors represent the results calculated by the three chosen models (PC-SAFT, PR-MC-WS-NRTL and PR-vdW-Wilson). The liquid-vapour equilibrium data of these systems were studied within specific temperature interval: three isotherms (253.15, 273.15 and 293.15) K for the system R134a + R290, three isotherms (273.15, 293.15 and 313.15) K for the system R152a + R1234ze, three isotherms (273.15, 293.15 and 313.15) K for the R152a + R1243zf system, and three isotherms too (243.15, 263.15, 283.15) K for the R1243zf + R134a system. The R134a + R290 system exhibits homogeneous azeotropic behavior at maximum pressure, while the others are non-azeotropic systems. The boiling and dew curves of these binary systems are well represented by the three proposed models, where there is a good agreement between the points calculated using the chosen models and the experimental data. The values of the bias and MRD of each isotherm of the binary systems are illustrated in the Table 4. The relative differences with PC-SAFT model do not exceed (1.78 % for pressure, and 3.86 % for the vapour mole fraction), (1.47 % for pressure, and 3.87 % for the vapour mole fraction) with the PR-vdW-Wilson model, and (2.42 % for vapour mole fraction, and 0.68 % for the liquid mole fraction) with the PR-MC-WS-NRTL model for the R134a + R290 system. The relative differences with PC-SAFT model do not exceed (0.76 % for pressure, and 0.95 % for the vapour mole fraction), (1.80 % for pressure, and 2.93 % for the vapour mole fraction) with the PR-vdW-Wilson model, and (3.85 % for vapour mole fraction, and 3.93 % for the liquid mole fraction) with the PR-MC-WS-NRTL

model for the R152a + R1234ze system. The relative differences with PC-SAFT model do not exceed (0.43 % for pressure, and 1.84 % for the vapour mole fraction), (0.54 % for pressure, and 2.82 % for the vapour mole fraction) with the PR-vdW-Wilson model, and (2.24 % for vapour mole fraction, and 1.29 % for the liquid mole fraction) with the PR-MC-WS-NRTL model for the R152a + R1243zf system. The relative differences with PC-SAFT model do not exceed (0.56 % for pressure, and 0.51 % for the vapour mole fraction), (0.56 % for pressure, and 0.84 % for the vapour mole fraction) with the PR-vdW-Wilson model, and (2.83 % for vapour mole fraction, and 1.67 % for the liquid mole fraction) with the PR-MC-WS-NRTL model for the R1243zf + R134a system.

4. Conclusion

The research aims to utilize three models, namely PC-SAFT, PR-MC-WS-NRTL, and PR-vdW-Wilson, for the computation of liquid and vapour mole fractions as well as pressure in binary systems. The investigation focuses on four binary systems: R134a + R290, 152a + R1234ze, R152a + R1243zf, and R1243zf + R134a. The study explores the liquid-vapor equilibrium data across different temperature intervals for each system. Notably, the R134a + R290 system exhibits homogeneous azeotropic behaviour at maximum pressure, while the others are non-azeotropic. The boiling and dew curves of these binary systems are effectively represented by the three proposed models. Demonstrating a favorable agreement between calculated and experimental data. The research evaluates the bias and mean relative differences (MRD) for each isotherm, with the relative differences for the liquid and vapor phases within acceptable limits, as exemplified by the R134a + R290 system.

List of symbols

\bar{a}	Reduced Helmholtz free energy
A	Parameter of the equation of state (energy parameter [J. m ³ .mol ⁻²]).
B	Parameter of the equation of state (molar covolume parameter [m ³ .mol ⁻¹])
C	Cubic term of the Helmholtz free energy equation.
D	segment diameter of component
EoS	Equation of State
F_{obj}	objective function
G	Molar Gibbs energy [J. mol ⁻¹].
K	Boltzmann constant
k_{ij}	Binary interaction parameter.
MC	Mathias-Copeman
$NRTL$	Non-Random- Two-Liquids
P	Pressure [MPa].
PR	Peng-Robinson
$SAFT$	Statistical Associating Fluid Theory
R	Gas constant [J.mol ⁻¹ .K ⁻¹]
RE	Relative Error ($\Delta U, \Delta P$)
T	Temperature[K]
VLE	Vapour-Liquid Equilibrium
x	Liquid mole fraction
y	Vapor mole fraction
U	represents x, y or P
V	Total volume [m ³]
vdW	van der Waals
WS	Wong-Sandler

Greekletters

a	Alpha function.
σ	segment diameter
ω	Acentric factor

Subscripts and superscripts

<i>assoc</i>	associating interactions
<i>c</i>	Pure-component critical property.
<i>cal</i>	Calculated property.
<i>chain</i>	chain formation
<i>Exp</i>	Experimental property.
<i>res</i>	Residual property
<i>i, j</i>	Molecular species.

References:

- [1] A. Vidal, P. Koukouvinis, and M. Gavaises, "Vapor-liquid equilibrium calculations at specified composition, density and temperature with the perturbed chain statistical associating fluid theory (PC-SAFT) equation of state," *Fluid Phase Equilibria*, vol. 521, p. 11266, 2020.
- [2] I. N. Diamantonis, G. C. Boulougouris, E. Mansoor, D. M. Tsangaris, and I. G. Economou, "Evaluation of Cubic, SAFT, and PC-SAFT Equations of State for the Vapor-Liquid Equilibrium Modeling of CO₂ Mixtures with Other Gases," *Ind. Eng. Chem. Res.*, vol. 52, pp. 3933-3942, 2013.
- [3] A. Aminian, "Modeling vapor-liquid equilibrium and liquid-liquid extraction of deep eutectic solvents and ionic liquids using perturbed-chain statistical associating fluid theory equation of state. Part II," *AIChE Journal*, vol. 68, p. e17774, 2022.
- [4] J. Gross and G. Sadowski, "An Equation of State Based on a Perturbation Theory for Chain Molecules," *Industrial & Engineering Chemistry Research*, vol. 40, pp. 1244-1260, 2001.
- [5] J. M. Mollerup and G. M. Montogeorgis, "Application of the SAFT-VR approach to the refrigerants methane, ethane, propane, n-butane, n-pentane, n-hexane, R134a, and R141b," *Fluid Phase Equilibria*, vol. 211, pp. 225-235, 2003.
- [6] A. Zerfa, Y. Maalem, H. Madani, and A. Beicha, "Modelling of the Isothermal Vapor-Liquid Equilibrium of Alternative Refrigerants: Determination of Phase Diagrams (High-pressure/Low-pressure) and Optimized Binary Interaction Parameters," *JPIChE*, vol. 51, pp. 39-58, 2023.
- [7] Y. Qin, N. Li, H. Zhang, B. Liu, C. Wu, and Z. Wang, "Experimental investigation on vapor liquid equilibrium and azeotropic behavior for the 1,1,1,2-tetrafluoroethane (R134a) + propane (R290) system at temperatures from 253.15 to 303.15 K," *International Journal of Refrigeration*, vol. 120, pp. 209-220, 2020.
- [8] S. Peng, E. Wang, Z. Yang, and Y. Duan, "Vapor-liquid equilibrium measurements for the binary mixtures of 1,1-difluoroethane (R152a) with trans-1,3,3,3-tetrafluoropropene (R1234ze(E)) and 3,3,3-trifluoropropene (R1243zf)," *Fluid Phase Equilibria*, vol. 558, p. 113470, 2022.
- [9] X. Yao, L. Ding, X. Dong, Y. Zhao, X. Wang, J. Shen, and M. Gong, "Experimental measurement of vapor-liquid equilibrium for 3,3,3-trifluoropropene (R1243zf) + 1,1,1,2-tetrafluoroethane (R134a) at temperatures from 243.15 to 293.15 K," *International Journal of Refrigeration*, vol. 120, pp. 97-103, 2020.
- [10] I. Anoune, Z. Mimoune, H. Madani, and A. Merzougui, "New modified PC-SAFT pure component parameters for accurate VLE and critical phenomena description," *Fluid Phase Equilibria*, vol. 532, p. 112916, 2021.
- [11] B. Bentama, H. Grine, I. Anoune, H. Madani, and C. Bougriou, "Calculation of azeotropic properties for binary mixtures with the PC-SAFT equation of state," *Fluid Phase Equilibria*, vol. 565, p. 113631, 2023.
- [12] Z. Mimoune, I. Anoune, and H. Madani, "Implementation of PC-SAFT for Predicting thermodynamic properties of pure refrigerants and vapor-liquid equilibria of refrigerants binary mixtures," *Fluid Phase Equilibria*, vol. 573, p. 113868, 2023.
- [13] S. Fedali, H. Madani, and C. Bougriou, "Modeling of the thermodynamic properties of the mixtures: Prediction of the position of azeotropes for binary mixtures," *Fluid Phase Equilibria*, vol. 379, pp. 120-127, 2014.
- [14] Y. Maalem, A. Zerfa, Y. Tamene, S. Fedali, and H. Madani, "Prediction of thermodynamic properties of the ternary azeotropic mixtures," *Fluid Phase Equilibria*, vol. 517, p. 1126, 2020.

Research Article

Thermodynamic Properties of R1234yf and DMAC Binary Solution

^{1*}B. Gurevich 

^{1*}Shamoon College of Engineering
E-mail: ¹bellagu@sce.ac.il

Received 6 June 2024, Revised 15 August 2024, Accepted 23 August 2024

Abstract

To assess the performance of potential refrigerant-absorbent pairs, it is essential to have thermodynamic properties of both the pure components and their mixtures. Since these mixtures do not behave ideally, the properties of the solutions can only be obtained through experimental means. This paper's proposed candidate pair is the environmentally friendly refrigerant 2,3,3,3-Tetrafluoropropene (R1234yf) and the organic solvent Dimethylacetamide (DMAC). For this purpose, an experimental setup was designed to obtain data at the equilibrium point between the gas and liquid phases. The collected data was analyzed using models based on the vapor-liquid equilibrium of mixtures. Correlations were established for pressure-temperature and refrigerant concentration in the liquid phase and the solution's enthalpy. These results can facilitate further investigations into the solution's compatibility as an alternative working pair.

Keywords: Vapor liquid equilibrium; binary solutions; refrigerant 2,3,3,3-tetrafluoropropene (R1234yf) and dimethylacetamide (DMAC); thermodynamic properties.

1. Introduction

The use of environmentally friendly refrigerants, such as hydrocarbons (HCs), hydrofluoroolefin (HFO), R744 (carbon dioxide), and eco-safe nano refrigerants, can help to reduce ozone depletion potential (ODP) and global warming potential (GWP). When selecting refrigerants, it is important to consider other environmental factors such as toxicity, flammability, vapor pressure, solubility, stability, and lubricity [1]. HCs have gained popularity since the 1990s due to their relatively low environmental impact. However, the introduction of perfluorocarbons and HFCs (Hydrofluorocarbon) faced criticism in the Kyoto Protocol of 1997 due to their high GWP. Recently, HFO refrigerants, including R1234yf, R1234ze, R1336mzz(Z), and R1336mzz(E), have been implemented, showing significant progress in the development of environmentally friendly options since 2008.

In commercial diffusion absorption cooling systems, the options for binary solutions used with an auxiliary gas are limited to ammonia-water or water-lithium bromide combinations. The ammonia-water mixture is widely used in diffusion-absorption refrigeration systems due to its chemical stability across a wide range of pressures and temperatures. Additionally, ammonia has a high latent evaporation heat and a low freezing point (-77°C), making it suitable for applications requiring low evaporation temperatures. However, since ammonia water is volatile, a rectifier is usually required to separate the evaporated water from ammonia, leading to heat loss and reduced energy efficiency. Despite these drawbacks, the advantages of ammonia water include its environmental friendliness and production cost (10-20%). Its thermophysical properties can be obtained from various sources [2-5]. One disadvantage of using ammonia water as a working fluid is its high operating

pressure, toxicity, and corrosive nature towards copper and copper alloys, limiting its use to materials like carbon steel.

Although ammonia-water-hydrogen has been used as a working fluid in diffusion-absorption refrigeration systems for many years, researchers have explored alternative working mixtures to minimize activation energy. Pfaff et al. [6] suggest the use of the lithium bromide-water mixture as a working fluid in diffusion-absorption systems. The input temperatures in the generator range from 66°C to 78°C , which activates the bubble pump and makes this mixture appealing for solar refrigeration applications. Water, when used as a refrigerant fluid, has an evaporation temperature limited to values above 0°C , making it a viable alternative for air-conditioning applications. The advantage of the lithium bromide-water mixture is that the absorbent is non-volatile, eliminating the need for rectifiers used in ammonia-water systems. However, vacuum pressures pose a disadvantage, and high concentrations of lithium bromide can lead to crystallization problems. Due to the corrosive nature of salts, installations using this mixture require construction materials like copper. Thermo-physical properties of this mixture can be obtained from various sources [7-11].

Fluoride refrigerants are recommended for their good solubility with organic solvents such as N, N'-dimethylformamide (DMF) and N, N'-dimethylacetamide (DMAC). Compared to ammonia, these refrigerants have the advantage of being less toxic, and compared to water, they can reach temperatures below 0°C suitable for refrigeration. They exhibit chemical stability, non-corrosiveness, and complete miscibility over a wide range of temperatures [12,13]. DMF is commonly used as an absorbent in absorption refrigeration systems and has been utilized in diffusion-absorption systems as well. However, precautions

must be taken to prevent leaks when DMF reacts with certain metals in the presence of oxygen. Various researchers [14-17] have studied the properties of halogenated refrigerants combined with DMF. Koyfman et al. [18] conducted an experimental study using R22 and DMF as the working fluid, achieving evaporation temperatures below 0°C with activation temperatures in the generator between 50°C and 90°C, resulting in an energy efficiency of 0.35. Zohar et al. [19] incorporated refrigerants R32, R124, R125, and R134a into their analysis using DMF as an absorbent in all cases, observing valid results under different operating conditions. They found that these mixtures could be activated at a lower temperature (150°C), but with a lower coefficient of performance and higher condensation and evaporation temperatures compared to the ammonia-water mixture. DMAC, another commercially available organic compound with good solubility, is considered an absorbent for refrigeration systems [16]. It has been combined with halogenated refrigerants in diffusion-absorption applications. Since the boiling temperatures of both compounds are very close, a certain amount of DMAC evaporates in the generator, necessitating the use of a rectifier to avoid condensing DMAC, which reduces cooling capacity and increases manufacturing costs. Ezzine et al. [20] showed that R124-DMAC is a good working pair, achieving lower vapor pressures than the mixture with DMF and activation temperatures between 80°C and 180°C, making them ideal for activation using solar energy, geothermal sources, residual heat, or other sources. Light hydrocarbons with organic solvents have also been explored in the literature [21]. Hydrocarbons and mixtures of alkanes have been extensively studied as refrigerants in vapor-compression refrigerating machines and heat pumps, as evidenced in existing literature [22, 23]. Simulation results using Fortran for an absorption refrigeration model, considering ten alkane mixtures with both air and water cooling were presented by [24]. Dardour et al. [25] performed simulations to analyze the overall behavior and performance of an absorption-diffusion system utilizing propane-nonane-hydrogen as the working fluid. Propane served as the refrigerant, nonane as the absorbent, and hydrogen as the inert auxiliary gas. The Peng-Robinson equation of state was employed to extract the thermodynamic characteristics of individual substances, as well as their binary solution properties, from the Aspen software databank. Hydrocarbon mixtures can be activated at temperatures between 120°C and 150°C, but their coefficient of performance is sometimes lower than the previously described mixtures.

The study of [26] investigated the use of a nano ferrofluid (Fe₃O₄-ammonia/water) as a binary working solution in DAR system and the research presented an experimental study demonstrating the enhancement in DARS (Diffusion Absorption Refrigeration Systems) performance using the nano ferrofluid with helium as an inert gas. The experiments were conducted with nano ferrofluids containing 0.05 wt.% and 0.1 wt.% Fe₃O₄ nanoparticles concentrations in 300 ml NH₃/H₂O base-fluid, with the addition of 1 wt.% concentration of polyvinyl pyrrolidone surfactant, both with and without an external magnetic field. The results showed that the DARS with 0.1 wt.% nano ferrofluid under the external magnetic field exhibited the best performance.

While the thermodynamic properties of pure absorbents and refrigerants are well known, the thermodynamic properties of binary organic mixtures suitable for absorption

refrigeration systems have not been fully investigated. Additionally, the behavior of Hydrofluoroolefin (HFO) refrigerants with various absorbents remains largely unexplored. Since the thermophysical properties of the working fluids depend on the refrigerant's concentration in the solution, the objective of this study is to experimentally determine the pressure-temperature-concentration of binary mixtures at equilibrium, as well as the enthalpy-temperature-concentration data. The investigated refrigerants include R1234yf and DMAC (N,N'-dimethylacetamide, C₄H₉NO)

2. Research Design and Methods

For the absorbent refrigerant pair to be acceptable, the refrigerant and absorbent must have a strong molecular attraction. Since these forces cause the fluids to deviate from ideal fluid behavior, it is required that the transport and thermodynamic properties of the refrigerant and solution will be determined experimentally.

The research design is based on the work of [27] and [28]. The experimental set up consists of 300 ml Parr 4383 reactor equipped with pressure and temperature measuring devices to determine the system's equilibrium data (see Figure .1). To keep the reactor at constant temperature, it was heated from the sides by a controlled electrical heating jacket, and was insulated around and above. The contents of the vessel were stirred magnetically with a Teflon-clad stirring capsule. The two thermocouples inserted into the reactor measured the temperature of the liquid phase and temperature of the gas phase above the solution. The system equilibrium pressure in the vessel was measured with the pressure gauge. The equilibrium vapor pressure-temperature-concentration relationships was determined according to the following procedure.

1. First, the reactor was weighed.
2. A predetermined amount of the absorbent, was introduced to the reactor, and the reactor was reweighed.
3. A vacuum pump degassed the absorbent, and the vessel was weighed again. Then, the refrigerant was inserted and the vessel was weighed again.
4. The mixture was heated up in steps of 5°C at high refrigerant concentrations and 10°C at low concentrations.
5. When thermal equilibrium (showed by the equality in the temperature readings) between the gas phase and the mixture was achieved, the readings were logged.
6. After the completion of a series of equilibrium measurements, the vessel was cooled down to the ambient temperature, a certain amount of gas was inserted, and the reactor was weighed again.



Figure 1. Experimental setup.

3. Data Analysis Based on Vapor Liquid Mixture Equilibrium

At the pressure vessel, the liquid phase is at the bottom and the gaseous phase is above it. The mass concentration of the refrigerant in the liquid phase is determined by the following procedure. When thermal equilibrium is reached, i.e., the temperature of the liquid phase equals the gas phase, the total volume of the vessel (known parameter) is:

$$V_T = V_S + V_G \quad (1)$$

The total volume V_T consists of the sum of the solution volume, V_S , and the gas volume, V_G .

The mass of the components m_R and m_A (refrigerant and absorbent) in the vessel is the sum of each component in the liquid phase and in the gas phase (also known parameters):

$$m_R = m_{RS} + m_{RG} \quad (2)$$

$$m_A = m_{AS} + m_{AG} \quad (3)$$

where m_{RS} is the mass of the refrigerant in the liquid phase, m_{RG} is the mass of the refrigerant in gas phase, m_{AS} is the mass of the absorbent in the liquid phase and m_{AG} is the mass of the absorbent in the gas phase.

The volumes of the liquid and the gas phases, V_S and V_G are:

$$V_S = m_{RS}v_{RS} + m_{AS}v_{AS} \quad (4)$$

$$V_G = m_{RG}v_{RG} + m_{AG}v_{AG} \quad (5)$$

where v_{RS} , v_{AS} , v_{RG} , v_{AG} are the specific volumes of the refrigerant and the absorbent in the liquid and vapor phases as function of the temperature and/or the pressure of the system. The specific volumes of v_{RS} , v_{AS} can be calculated from the densities of the refrigerant and absorbent in the liquid phase:

$$v_{RS} = \frac{1}{\rho_{RS}} \quad (6)$$

$$v_{AS} = \frac{1}{\rho_{AS}} \quad (7)$$

In general, the density of the refrigerants can be obtained from the EES (Engineering Equation Solver) and density of the absorbent component in the liquid phase can be calculated by following polynomial equation:

$$\rho_{iS} = \rho_0 + \rho_1 T + \rho_2 T^2 \quad (8)$$

Note that the density is in the units of $\frac{gr}{cm^3}$ and the temperature in Celsius. The density constants ρ_0, ρ_1, ρ_2 are presented in Table 1.

Table 1. Density constants [26].

	ρ_0	ρ_1	ρ_2
DMAC	0.9528000	0.0005856	-0.000003363

The specific volume of the components in the gas phase v_{RG} and v_{AG} are the ratio of molar volume to molecular weight and will be calculated from Peng-Robinson equation of state (EOS).

$$v_{iG} = \frac{V_{iG}}{M_i} \quad (9)$$

$$P = \frac{RT}{V_{iG} - b_i} - \frac{a_i}{V_{iG}^2 + 2b_i V_{iG} - b_i^2} \quad (10)$$

$$a_i = 0.45724 \frac{R^2 T_{ci}^2}{p_{ci}} \left[1 + f_w (1 - T_{ri}^{0.5}) \right]^2 \quad (11)$$

$$b_i = 0.0778 \frac{RT_{ci}}{p_{ci}} \quad (12)$$

$$f_w = 0.37464 + 1.54226\omega + 0.26992\omega^2 \quad (13)$$

where, a_i and b_i are cubic EOS parameters, R is the ideal gas constant, T_{ci} and p_{ci} are critical temperature and pressure of the substance, T_{ri} is the reduced temperature and ω is the acentric factor. The data for the components is presented in Table 2.

Table 2. Data for the components.

	$T_c [^{\circ}C]$	$p_c [bar]$	$M \left[\frac{gr}{mol} \right]$	ω
R1234yf	94.7	33.82	114	0.276
DMAC	382.4	42.11	87.12	0.363

After the specific volumes are calculated, the weight fraction of the refrigerant in liquid phase can be defined by:

$$\xi_R = \frac{m_{RS}}{m_{RS} + m_{AS}} \quad (14)$$

and the weight fraction of the absorbent was calculated by:

$$\xi_A = 1 - \xi_R \quad (15)$$

Similarly, the weight fractions of the refrigerant and the absorbent in gas phase can be calculated by:

$$\psi_R = \frac{m_{RG}}{m_{RG} + m_{AG}} \quad (16)$$

$$\psi_A = 1 - \psi_R \quad (17)$$

The mole fractions of the refrigerant and the absorbent in liquid phase were calculated by:

$$x_R = \frac{\xi_R M_A}{\xi_R M_A + \xi_A M_R} \quad (18)$$

$$x_A = 1 - x_R \quad (19)$$

The mole fractions of the refrigerant and the absorbent in gas phase can be calculated by:

$$y_R = \frac{\psi_R M_A}{\psi_R M_A + \psi_A M_R} \quad (20)$$

$$y_A = 1 - y_R \quad (21)$$

There is one unknown parameter left. When there is an equilibrium between two phases, the fugacities are equal $f_i^V = f_i^L$ and for each component obtained:

$$y_i p = \gamma_i x_i p_i^{sat} \Phi_i \quad (22)$$

where y_i is the mole fraction of component i , p is the measured pressure of the system, γ_i is the activity coefficient, x_i is the molar concentration of component i in the liquid solution, p_i^{sat} is the saturation pressure of component i , Φ_i is the correction factor for pressure changes in the system and is calculated the following way:

$$\Phi_i = \exp \left[\frac{(V_i^L - B_i)(p - p^{sat})}{RT} \right] \quad (23)$$

where V_i^L and B_i are the molar volume and second virial coefficient of component i in the liquid phase.

For a binary system consisting of an absorber and a refrigerant:

$$y_A p = \gamma_A x_A p_A^{sat} \Phi_A \quad (24)$$

$$y_R p = \gamma_R x_R p_R^{sat} \Phi_R \quad (25)$$

The activity coefficient for each of the components is going to be calculated from the Van Laar relation for the molar excess Gibbs free energy g^E and activity coefficient γ_i :

$$\frac{g^E}{RT} = \frac{A x_A x_R}{x_R \left(\frac{B}{A} \right) + x_A} \quad (26)$$

$$\ln \gamma_R = A \left(1 + \frac{A}{B} \left(\frac{x_R}{x_A} \right) \right)^{-2} \quad (27)$$

$$\ln \gamma_R = A \left(1 + \frac{A}{B} \left(\frac{x_R}{x_A} \right) \right)^{-2} \quad (28)$$

where A, B are constants depending on temperature. Division of Eqs. (27) and (28) gives a new relationship between the activity coefficients of the two components:

$$\frac{\ln \gamma_A}{\ln \gamma_R} = \frac{A}{B} \left(\frac{x_R}{x_A} \right)^2 \quad (29)$$

When the activity coefficients are substituted into the equilibrium equations, it yields:

$$\ln \gamma_A = \ln \left(\frac{y_A p}{x_A p_A^{sat} \Phi_A} \right) \quad (30)$$

$$\ln \gamma_R = \ln \left(\frac{y_R p}{x_R p_R^{sat} \Phi_R} \right) \quad (31)$$

Due to the lack of an equation, the following assumption can be used:

$$\frac{B}{A} = \frac{V_A^L}{V_R^L} \quad (32)$$

After obtaining pressure-temperature-concentration data, it will be expressed in as a polynomial function:

$$p = \sum_{j=0}^{j=5} \sum_{i=0}^{i=6} p_{ij} \xi_R^i T^j \quad (33)$$

p_{ij} values were obtained by regression of the equilibrium results. The temperature T is in Kelvin. The results of the pressure-temperature-concentration are presented in Figure 2. Values of p_{ij} are presented in Table 3.

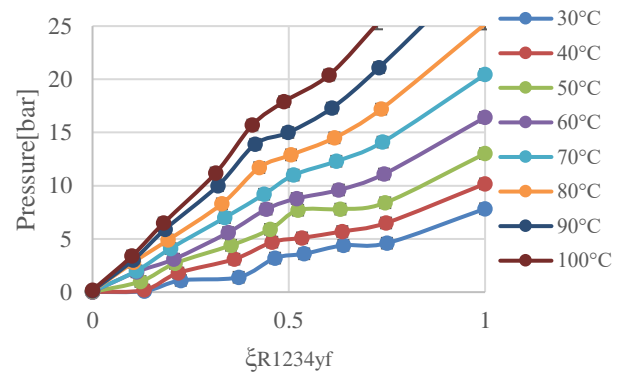


Figure 2. Pressure-temperature-concentration results in equilibrium.

Table 3. p_{ij} coefficients of R1234yf and DMAC.

i,j	0	1	2	3	4	5
0	277	-28.3	1.15	-0.0241	0.00028	0
1	-49	1.65	0.0986	-0.00437	0.00006	0
2	-8780	819	-29.9	0.527	-0.0045	0.00002
3	36700	-3390	123	-2.15	0.0182	-0.00006
4	-51700	4760	-172	3.01	-0.0255	0.00008
5	24100	-2170	78.7	-1.38	0.0117	-0.00004
6	-395	0	0	0	0	0

Table 4. h_{ij} coefficients of R1234yf and DMAC.

i,j	0	1	2	3	4	5	6
0	7670	192000	1440000	-4710000	6770000	-3270000	344000
1	638	16800	-127000	424000	632000	343000	0
2	18.2	-517	3960	13200	19800	-10700	0
3	-0.229	7.43	57.3	192	-288	157	0
4	0.00113	-0.00509	0.389	-1.31	1.97	1.07	0
5	0	0.00013	-0.001	0.00339	-0.00509	424000	0

In order to obtain the enthalpy of the solution, the following formula is used:

$$h = h_R \xi_R + h_A (1 - \xi_R) + h^E \quad (34)$$

h_R and h_A are the specific enthalpies of the pure components, h^E is the excess specific enthalpy of mixing and h is the enthalpy of the solution in the liquid phase. The data for the calculations of the specific enthalpies of the absorbent and the refrigerant can be found in the literature. However, it is important to state that the reference point is $100 \frac{kJ}{kg}$ at $0^\circ C$. The molar excess enthalpy H^E can be calculated the following manner:

$$H^E = -RT^2 \left(\frac{\partial \left(\frac{g}{RT} \right)}{\partial T} \right)_{p,x} \quad (35)$$

Gibbs free energy g equals to:

$$g = RT (x_A \ln \gamma_A + x_R \ln \gamma_R) \quad (36)$$

The results of the excess enthalpy with respect to molar refrigerant concentration are presented in Figure 3.

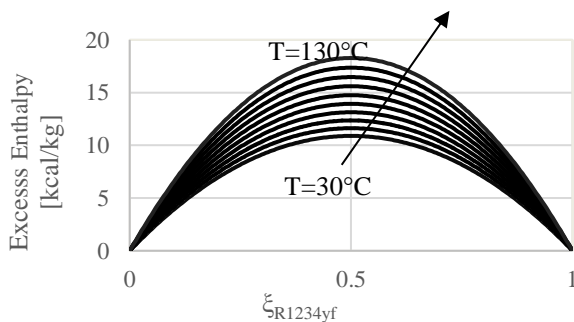


Figure 3. Excess enthalpy as a function of the refrigerant concentration for various equilibrium temperatures.

The specific excess enthalpy can be expressed in a polynomial form:

$$h^E = 4.1868 \sum_{i=0}^5 \sum_{j=0}^6 h_{ij} \xi_R^i T^j \quad (37)$$

The excess enthalpy of the liquid solution is in $\frac{kJ}{kg}$ and the temperature T is in Celsius. The coefficients h_{ij} were determined by regression of the equilibrium data. Their values are presented in Table 4.

Enthalpy of the liquid solution for various temperatures as a function of the refrigerant mass concentration is presented in Figure 4.

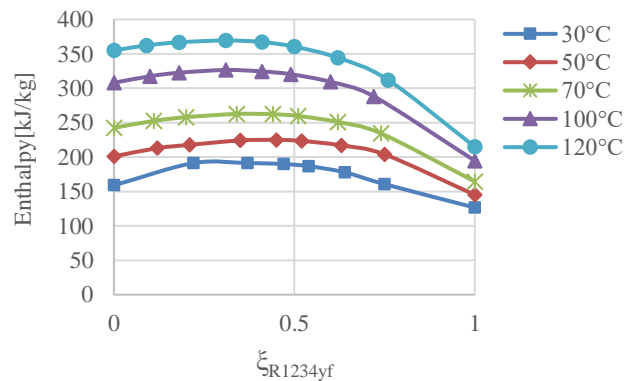


Figure 4. Liquid phase enthalpy as a function of the refrigerant concentration for various equilibrium temperatures.

4. Conclusions

This paper presents a thorough analysis of the thermodynamic characteristics of a new binary solution. The data utilized in this study was gathered through experimental measurements of mass, temperature, and pressure of the solution's phases at equilibrium. By employing a relatively simple setup and conducting complex data analysis, the thermodynamic properties of the binary solution consisting of R1234yf and DMAC were determined. The findings, published in this paper, provide researchers with the essential thermodynamic information needed for further investigations.

The outcomes, specifically the pressure-temperature-refrigerant concentration in the liquid phase, can be utilized to ascertain the solution concentration based on temperature and pressure at the absorber of the DAR system. Additionally, the enthalpy data is crucial for calculating the performance of the DAR system when utilizing R1234yf and DMAC as working fluids.

Acknowledgements:

The research was funded by the Israeli Ministry of Energy.

Nomenclature

A	First virial coefficient	
a	EOS parameter	
B	Second virial coefficient	
b	EOS parameter	
f	Fugacity	[bar]
g	Gibbs free energy	[kJ/kg]
h	Enthalpy	[kJ/kg]
M	Molar mass	[kg/kmol]
m	Mass	[kg]
p	Pressure	[bar]
T	Temperature	[°C],[K]
V	Volume	[m ³]
v	Specific volume	[m ³ /kg]
x	Mole fraction in liquid phase	
y	Mole fraction in gas phase	

Greek symbols

γ	Activity coefficient	
ξ	Weight fraction in liquid phase	
ρ	Density	[kg/m ³]
Φ	Correction factor	
ψ	Weight fraction in gas phase	
ω	Acentric factor	

Subscripts

AG	Absorbent in gas phase
AS	Absorbent in liquid phase
c	Critical
G	Gas
i	Component index
RG	Refrigerant in gas phase
RS	Refrigerant in liquid phase
S	Solution
T	Total

Superscript

E	Excess
L	Liquid
V	Vapor

References:

- [1] H. Averfalk, P. Ingvarsson, U. Persson, M. Gong, and S. Werner, "Large heat pumps in Swedish district heating systems," *Renew. Sustain. Energy Rev.*, 79, 1275-1284, 2017
- [2] B. Ziegler and C. Trepp, "Equation of state for ammonia-water mixtures," *Int. J. Refrig.*, 7, 101-106, 1984.
- [3] Y.M. El-Sayed and M. Tribus, "Thermodynamic properties of water-ammonia mixtures: theoretical implementation for use in power cycle analysis", *ASME Pub. J.*, 89-95.,1985.
- [4] K.E. Herold, K. Han and M.J. Moran., "AMMWAT: a computer program for calculating the thermodynamic properties of ammonia and water mixtures using a Gibbs free energy formulation". *ASME Pub.*, 4, 65-75, 1988.
- [5] Y.M. Park and R.E. Sonntag, "Thermodynamic properties of ammonia-water mixtures: a generalized equation-of-state approach," *ASHRAE Trans.*, 96, 150-159, 1990.
- [6] M. Pfaff, R. Saravanan, M. Prakash Maiya, and S. Srinivasa Murthy, "Studies on bubble pump for a water-lithium bromide vapor absorption refrigerator," *Int. J. Refrig.*, 21, 452-462, 1998.
- [7] L.A. McNeely, "Thermodynamic properties of aqueous solutions of lithium bromide," *ASHRAE Trans.*, 85, 413-434, 1979.
- [8] R.J. Lee, R.M. DiGuilio, S.M. Jeter, and A.S. Teja, "Properties of lithium bromide-water solutions at high temperatures and concentrations-part II: density and viscosity," *ASHRAE Trans.*, 96, 709-714, 1990.
- [9] M. Jeter, J.P. Moran, and A.S. Teja, "Properties of lithium bromide-water solutions at high temperatures and concentrations-part III: specific heat," *ASHRAE Trans.*, 98, 137-149, 1992.
- [10] J.L.Y. Lenard, S.M. Jeter, and A.S. Teja, "Properties of lithium bromide-water solutions at high temperatures and concentrations-part IV: vapor pressure," *ASHRAE Trans.*, 98, 167-172, 1992.
- [11] J. Patek and J. Klomfar, "Simple function for fast calculations of selected thermodynamic properties of ammonia-water system," *Int. J. Refrig.*, 18, 228-234, 1995.
- [12] M. Fatouh and S. Srinivasa Murthy, "Comparison of R22-absorbent pairs for absorption cooling based on P-T-X data," *Renew. Energy*, 3, 31-37, 1993.
- [13] M.O. McLinden, E.W. Lemmon, and R.T. Jacobsen, "Thermodynamic properties for alternatives refrigerants," *Int. J. Refrig.*, 21, 322-338, 1998.
- [14] R.S. Agarwal and S.L. Bapat, "Solubility characteristics of R22-DMF refrigerant-absorbent combination," *Int. J. Refrig.*, 12, 70-74, 1985.
- [15] S. Dorairaj and R.S. Agarwal, "Prediction of transport properties of R22-DMF refrigerant-absorbent combinations", *Int. J. Refrig.*, 10, 224-228, 1986.
- [16] N.N. Smirnova, L.Ya Tsvetkova, T.A. Bykova, and Y. Marcus, "Thermodynamic properties of N,N-

- dimethylformamide and N,N-dimethylacetamide," *J. Chem. Thermodyn.*, 39, 1508-1513, 2007.
- [17] L.J. He, L.M. Tang, J.M. Chen, "Performance prediction of refrigerant-DMF solutions in a single-stage solar-powered absorption refrigeration system at low generating temperatures", *Solar Energy*, 83, 2029-2038, 2009.
- [18] A. Koyfman, M. Jelinek, A. Levy, I. Borde, "An experimental investigation of bubble pump performance for diffusion absorption refrigeration system with organic working fluids," *Appl. Therm. Eng.*, 23, 1181-1194, 2003.
- [19] A. Zohar, M. Jelinek, A. Levy, I. Borde, "Performance of diffusion absorption refrigeration cycle with organic working fluids," *Int. J. Refrig.*, 32, 1241-1246., 2009.
- [20] N. Ben Ezzine, R. Garma, and A. Bellagi, "A numerical investigation of a diffusion-absorption refrigeration cycle based on R124-DMAC mixture for solar cooling," *Energy*, 35, 1874-1883, 2010.
- [21] N. Ben Ezzine, R. Garma, M. Bourouis, and A. Bellagi, "Experimental studies on bubble pump operated diffusion absorption machine based on light hydrocarbons for solar cooling," *Renew. Energy*, 35, 464-470, 2010.
- [22] E. Granryd, "Hydrocarbons as refrigerants - an overview," *Int. J. Refrig.*, 24, 1, 15-24, 2001.
- [23] B. Palm, "Hydrocarbons as refrigerants in small heat pump and refrigeration systems – A review," *Int. J. Refrig.*, 31, 4, 552-563, 2008.
- [24] N. Chekir, Kh. Mejbri, A. Bellagi, "Simulation d'une machine frigorifique à absorption fonctionnant avec des mélanges d'alcanes," *Int. J. Refrig.*, 29, 3, 469-475, 2006.
- [25] H. Dardour, P. Cézac, J.-M. Reneaume, M. Bourouis, and A. Bellagi, "Numerical Investigation of an Absorption-Diffusion Cooling Machine Using C3H8/C9H20 as Binary Working Fluid," *Oil Gas Sci. Technol.*, 68, 249-254, 2013.
- [26] M. Mehyo, E. Özbaş, and H. Özcan, "Performance investigation of utilizing nanoferrofluid as a working solution in a diffusion absorption refrigeration system under an external magnetic field effect," *Heat Mass Transfer*, 58, 2107-2128, 2022.
- [27] I. Borde, M., Jelinek, N.C Daltrophe, "Working fluids for an absorption system based on R124 (2-chloro-1,1,1,2,-tetrafluoroethane) and organic absorbents," *Int. J. Refrig.*, 20, 4, 256-266, 1997.
- [28] N. Dvoskin, "Thermodynamic equilibrium of new organic mixtures for absorption heat pumps," M.S. Thesis, Dept. Mech. Eng., Ben Gurion Univ., Beer Sheva, Israel, 2004.

Research Article

Thermodynamic Efficiency Analysis of a Combined Power and Cooling (ORC-VCRC) System Using Cyclopentane (C_5H_{10}) as a Substitute for Conventional Hydrocarbons

¹Y.Maalem , ²*H.Madani 

¹National Polytechnic School of Constantine (ENPC), BP75 A, Nouvelle Ville RP, 25000 Constantine, Algeria

²Laboratory of Studies of Industrial Energy Systems (LESEI), Department of Mechanical Engineering, Faculty of Technology, University of Batna 2, 05000 Batna, Algeria

E-mails: ¹youcef.maalem@cp.enp-constantine.dz, ²*h.madani@univ-batna2.dz

Received 31 May 2024, Revised 10 August 2024, Accepted 23 October 2024

Abstract

The present study investigation aims to contribute to the field of energy engineering by exploring the performances of cyclopentane gas as promising working fluid in combined power and cooling (ORC–VCRC) system. The present research emphasizes the comparative computation of various thermodynamic performance characteristics of (ORC–VCRC) system activated by low temperature heat sources using cyclopentane gas as a substitute to the conventional hydrocarbons (butane, isobutene, propane and propylene) widely used in (ORC–VCRC) system. A computer code was developed using MATLAB software for the numerical simulation. The performance characteristics computed are the performance indicators (overall coefficient of performance (COP_{oval}) and working fluid mass flow rate of per kW cooling capacity (MkW), expansion ratio in expander (EPR) and compression ratio in compressor (CMR). Furthermore, the effects of different operating parameters (e.g., boiler, condenser, and evaporator temperatures, isentropic efficiency of expander (η_{exp}), and isentropic efficiency of compressor (η_{comp})) on performance indicators are also examined for each working fluid. Results showed that under the same operating parameters, the use of cyclopentane gas as a working fluid in (ORC–VCRC) system exhibited a higher COP_{oval} and lower MkW compared with conventional hydrocarbons. When boiler temperature reaches 90 °C, the COP_{oval} of cyclopentane increase by 14 %, 19.8 %, 43.8 % and 59 % compared to those of butane, isobutene, propane and propylene, respectively. However, the MkW of cyclopentane reduced by 19.1 %, 29.2 %, 44.3 % and 53.7 % compared to same fluids, respectively. On another hand, the study revealed that the COP_{oval} rises as the temperature of the boiler, evaporator, η_{exp} and η_{comp} rises. Conversely, when the condenser temperature rises, the COP_{oval} value falls for all fluids. Overall, the study confirms that cyclopentane gas could be a promising working fluid in terms of performance indicators for (ORC–VCRC) system.

Keywords: Hybrid (ORC–VCRC) system; cyclopentane gas; thermodynamic analysis; performance indicators.

1. Introduction

Due to increasing energy and environmental problems, the development of new energy technologies and the exploration of alternative working fluids with environmentally friendly properties have become the most researched areas in energy engineering, particularly in the areas of power and cooling applications.

Today's, hybrid thermodynamic cycles, which combined the energy systems, such as power systems, refrigeration systems, heat pumps and air-conditioning systems are regarded as an efficient way to utilize the medium and low temperature heat sources of the renewable energies (solar heat, biogas, biomass, ..., etc) [1-2] for its various advantages (high energy conversion efficiency, low cost, easy maintenance, environmentally friendly, etc.) [3], where the use of this new technologies is growing significantly in the field of building energy.

One of this hybrid thermodynamic cycles that has been gaining attention is the hybrid ORC–VCR system, which

combined the organic Rankine cycle (ORC) with the vapor compression refrigeration (VCR) to convert the thermal energy input obtained from renewable energies sources at low and medium temperature into beneficial cooling or electrical power [4-5].

The working fluid selection has a considerable influence on the performance of the hybrid ORC–VCR system. At present, the choice of new working fluid is a challenge for the hybrid power-cooling system, where the good working fluid should be safe and environmentally friendly, should have high overall performances and adapt to the temperature of the available heat source [6-9]. In this context, many studies have been published in recent years using different working fluids on this type of hybrid system to improve the performances of the energy conversion at low temperatures by several researchers.

Saleh [10] proposed hydrofluoroolefins and common hydrofluorocarbons as working fluids for an ORC–VCR system that is powered by low-grade thermal energy. The

ORC–VCR system combines vapor compression refrigeration and the organic Rankine cycle. With a maximum overall performance of 0.718 at a condenser temperature of 30 °C and basic values for the remaining parameters, the results showed that working fluid R600 is the best candidate compared to the other substances suggested for the hybrid (ORC–VCR) system. Still, its flammability ought to draw sufficient notice.

Aphornratana and Sriveerakul [11] assessed the two working fluids, R22 and R134a, to determine which was best for the heat-powered refrigeration cycle and a combined Rankine–vapor–compression refrigeration cycle. The system can be powered by low-grade thermal energy as low as 60 °C and produce cooling temperatures as low as –10 °C. The results showed that R134a achieves the best system performance.

The performance and working fluid selection for a (VCR–ORC) system which recover the waste heat rejected by the condenser of air-conditioning system were examined by Asim et al. [12] Based on thermodynamics (energy and exergy) and thermo-economic analysis, R600a–R123 was chosen as the fluid pair for the integrated system, where the authors concluded that the combined coefficient of performance (COP) of the system could be improved from 3.10 to 3.54.

Mole's et al. [13] investigated a combined (ORC–VCR) system under various operating conditions that was activated by low temperature heat sources, using low GWP fluids with R134a for the power and refrigeration cycles. They concluded that R1336mzz(Z) and R1234ze(E), respectively, are the best candidates for the power and refrigeration cycles.

The performance of an ORC–VCR system was assessed by Li et al. [14] using the four hydrocarbons propylene, butane, propane, and isobutane. The system's optimal fluid, according to the results, is butane, which has an overall system coefficient of performance of 0.470.

Bu et al. [15] looked into six working fluids: R134a, R123, R245fa, R290, R600a, and R600. Their goal was to find the best working fluids for an ORC–VCR system that was activated by geothermal energy. They concluded that R600a is the best option. Nevertheless, enough attention should be paid to R600a's flammability.

Wang et al. [16] studied an (ORC–VCR) system using two different working fluids for the organic Rankine cycle and conventional vapor compression cycle, namely R245fa and R134a, respectively. The overall system coefficient of performance reached nearly 0.50.

Based on thermodynamics (energy and exergy), Nazer and Zubair [17] and Egrican and Karakas [18] examined an ORC–VCR system using the refrigerants R114 for the Rankine cycle and R22 for the vapor compression cycle. They concluded that it is critical to have the least amount of irreversibility possible in the system to complete the task more cheaply and with a more economical use of natural resources.

Kim and Perez-Blanco [19] examined an (ORC–VCR) system using eight working fluids (R143a, R22, R134a, R152a, propane, ammonia, isobutane, and butane), arranged according to their critical temperatures. The system was activated by low-grade sensible energy. The findings showed that because of its relatively high efficiencies, isobutane provides a sensitivity analysis in a few unique situations.

Three different refrigerants were evaluated by Jeong and Kang [20] to determine which was the best fit for the ORC–

VCR system: R123, R134a, and R245ca. The R123 case is found to provide the highest thermal efficiency.

The combined (ORC–VCR) thermodynamic model was developed by Bing et al. [21] for ship air conditioning to transfer the heat from flue gas waste and effectively use cooling water. Using five widely used working fluids: R22, R141b, R236ea, R218 and R601. The system performance was examined. It was determined through calculations that R601 was the best working fluid.

The thermal performance analysis of an ORC–VCR system with a common shaft was the focus of the study of Khatoon et al. [22]. Two refrigerants, R245fa and Propane, were selected for the organic Rankine cycle and three, R245fa, R123, and R134a, were chosen for the vapor compression cycle. When R123 was used as the working fluid in the vapor compression cycle and propane was used in the organic Rankine cycle, the results showed that the former had the highest efficiency (16.48%) and the latter had the highest coefficient of performance (2.85) at 40°C.

The energy and exergy analysis of a combined refrigeration and waste heat driven organic Rankine cycle system was assessed by Cihan and Kavasogullari [23] using five different organic fluids, which are R123, R600, R245fa, R141b, and R600a. They concluded from result of energy and exergy analysis that R141b is the most appropriate organic working fluid.

Kavasogullari et al. [24] studied the performance indices such as the cooling coefficient of performance (COP), exergy destruction and exergy efficiency of dual-ejector refrigeration system (DER) which constructed by adding a second ejector and a refrigeration pump to the classical single-ejector refrigeration system (SER). In their analysis, two different refrigerants (R134a and R600) are employed and compared at the same conditions. According to their results, with the DER system, the maximum cooling COP and energy efficiency are attained by 7.52 and 38.8%, respectively. R134a has a minimum exergy destruction of 9.3 kJ/kg in the DER system at evaporation temperatures of 10 °C and condensing temperatures of 40 °C. Furthermore, at 55 °C for the condenser and 5 °C for the evaporator, R600 produces 5.3% increases in the cooling COP and exergy efficiency. The outcomes also demonstrated that at high condensing and low evaporation temperatures, the DER system produces greater gains in cooling COP and energy efficiency.

Küçük and Kılıç [25] examined a hybrid (ORC–VCR) system operating under diverse conditions for the purpose of producing power and cooling. In the analysis, authors are using the working fluids (R114, R123, R600, R600a, and R245fa) in the ORC system and (R141b, R600a, R290, R134a, R123, R245fa and R143a) in the subsystem VCRC. They concluded that the highest energy utilization factor, exergy efficiency, the system coefficient of performance, and net power is obtained for the R123–R141b fluid pair.

Al-Sayyab et al. [26] looked at the working fluid selection and performance of modified compound organic Rankine–vapor compression cycle using ultra-low global warming potential working fluids (R1234ze(E), R1243zf, and R1234yf). The system can be adapted to three operating modes, depending on the ground source temperature, ranging from 55 to 90 °C: power-cooling, power-heat pump heating, and power-ground source heating. The results indicate that this system notably increases the overall performance of all investigated refrigerants.

Compared to conventional organic Rankine and vapor compression cycles (ORC and VCC), the R1234ze(E) power-cooling mode shows the highest coefficient of performance (COP) increase, 18 %. Besides, including a recapture heat exchanger for condenser waste heat recovery can increase power generation by 58 %. At ground source temperatures up to 65 °C, power generation and thermal efficiency increased in the power-heating mode due to the absence of the compressor power consumption.

Zhar et al. [27] investigated the performance of combining power and refrigeration system, which consists of an Organic Rankine Cycle driven Vapor Compression Cycle from waste heat source using R123, R11, and R113 as working fluids. The numerical model of the system is developed under Engineering Equation Solver software. Their findings indicate that the R123 is the best working fluid where the highest energy and exergy efficiencies using R123 as working fluid are over 1.02 and 0.53 respectively.

In the study of Wang et al. [28], authors experimented the performance of the (ORC–VCC) system with a zeotropic mixture of R245fa/R134a (0.9/0.1) at various evaporation temperatures and cooling conditions. In addition, the coupling effect of cooling water temperature and flow rate on the performance of the ORC–VCC system are investigated. They concluded that the cooling water temperature has a greater impact on system operational characteristics than cooling water flow rate. As the cooling water temperature, decreases and its flow rate increases, the cooling capacity of the system increases, while the coefficient of performance changes little.

From the abovementioned review about the previous researches, it is clear that there is still a need to search for suitable alternative working fluids for the (ORC–VCR) system that can meet the requirements of cycle performance, environmental performance, thermo-physical properties and safety at the same time, where it was noted that most of the investigations have been focusing on hybrid ORC–VCR system performance evaluation operating with pure working fluids (CFC, HCFC, and HFC) have strong climate impacts, which has several drawbacks, such as environmental performance.

On other hand, the use of conventional hydrocarbons (HCs), such as (butane (R600), isobutene (R600a), propane (R290), etc.) as suitable working fluids in ORC–VCR system is good choice, because these hydrocarbons are rather cheap, plentiful and environmentally benign chemicals (zero ODP and near zero GWP), good thermodynamic performances, thermo-physical properties, non-toxic and have many outstanding properties. However, there are very limited researches, which focused on thermodynamic efficiency analysis of combined power and cooling (ORC–VCRC) system by using this type of working fluids, where we can find research gaps in the cycle performances of the hydrocarbons in the published literature.

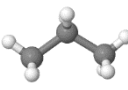
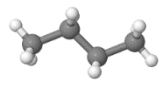
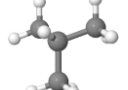
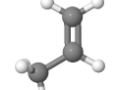
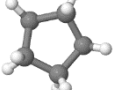
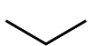
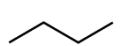
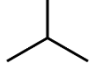
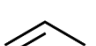

There is recently a renewed interest in the use of cyclopentane gas (C₅H₁₀) as promising working fluid in the thermodynamic systems [29]. This study is conducted for this purpose.

This paper aims to contribute to the field of energy engineering by exploring the performances of cyclopentane gas as a substitute to the conventional hydrocarbons (butane, isobutene, propane and propylene) widely used in (ORC–VCRC) system activated by low-temperature renewable energies having a temperature around 100 °C. Therefore, a comparative computation of various thermodynamic performance characteristics of cyclopentane, butane, isobutene, propane and propylene was carried out under the same operating conditions.

The investigated performance characteristics are (performance indicators (overall coefficient of performance (COP_{oval}) and working fluid mass flow rate of per kW cooling capacity (MkW), expansion ratio in expander (EPR) and compression ratio in compressor (CMR)). Furthermore, the effects of different operating parameters (e.g., boiler, condenser, and evaporator temperatures, isentropic efficiency of expander (η_{exp}), and isentropic efficiency of compressor (η_{comp})) on performance indicators are also examined for each working fluid.

The basic physical and environmental properties of the investigated working fluids are shown in Table 1 [30–36].

Table 1. Basic physical and environmental properties of investigated hydrocarbons [30–36].

Specifications	Unit	Propane	Butane	Isobutene	Propylene	Cyclopentane
Component properties						
Chemical formula	-	C ₃ H ₈	C ₄ H ₁₀	Iso-C ₄ H ₁₀	CH ₂ =CH=CH ₂	C ₅ H ₁₀
Type of working fluid	-	HC	HC	HC	HC	HC
Molecular structure	-					
Chemical structure	-					
CAS Registry Number	-	74-98-6	106-97-8	75-28-5	115-07-1	287-92-3
Basic physical properties						
Molar mass	(kg/kmol)	44.096	58.122	58.122	42.08	70.133
Critical temperature	(K)	369.89	425.13	407.85	365.57	511.72
Critical pressure	(MPa)	4.2512	3.796	3.6400	4.665	4.5712
Normal boiling point	(K)	231.04	272.66	261.4	225.46	322.41
Basic environment properties						
ODP (R11 = 1)	-	0	0	0	0	0
GWP (CO ₂ = 1, 100 yrs)	-	3	20	3	4	<25

2. Description of Hybrid (ORC–VCRC) System

Figure 1 (a) illustrates the schematic diagram of the studied hybrid (ORC–VCRC) system, which consists of two subsystems: the organic Rankine cycle (ORC) identified as (1–2–3–4–1) and the vapor compression refrigeration cycle (VCRC) identified as (5–6–3–7–5). The studied hybrid (ORC–VCRC) system comprises essentially seven components, which are: a feed pump, a boiler, an expander, a condenser, a compressor, a throttle valve and an evaporator.

Figure 1 (b) depicts the corresponding temperature–entropy (T-s) diagram of the state points and various processes of the studied hybrid (ORC–VCRC) system. The various processes of the sub-systems (ORC and VCRC) of the studied hybrid (ORC–VCRC) system can be described as follows:

In the subsystem ORC: process (1→2s) is an isentropic expansion process across the expander, process (1→2) is the condenser, process (3→4s) is an isentropic pumping process, process (3→4) is the actual pumping process and (4→1) is a heat addition process in the boiler.

In the subsystem VCRC: process (5→6s) is an isentropic compression across the compressor, process (5→6) is the actual compression process, process (6→3) is a heat rejection (condensation) process across the condenser, process (3→7) is an isenthalpic expansion across the throttle valve and process (7→5) is a heat absorption (evaporation) process in the evaporator.

The two cycles work respectively as follows:

- In the subsystem ORC, the condensed working fluid is pressurized by the feed pump and enters the boiler where it is heated by the low temperature heat source. Then the vapor of working fluid produced in the boiler at high-pressure flows into the expander, which produces mechanical work to drive the compressor in the VCRC. Subsequently, the working fluid returns to the condenser and the ORC is completed.
- In the subsystem VCRC, the liquid working fluid out of the condenser goes through the throttle valve and enters, the evaporator where the low pressure and low temperature working fluid vaporizes and cools the conditioned space where it produces cold. In the sequence, the vapor of working fluid is sucked into the compressor where it is pressurized and then discharged into the condenser to complete the VCRC.

3. Methodology and Mathematical Formulation

3.1 Thermodynamic Assumptions

To develop the thermodynamic models of the studied hybrid (ORC–VCRC) system, the following thermodynamic assumptions are made:

- Steady-state flow in each component is considered;
- The pressure and heat losses in the hybrid (ORC–VCRC) system are negligible;
- The potential energy and kinetic energy are not considered in the hybrid (ORC–VCRC) system;
- The transformations in all heat exchangers are isobaric process;
- The working fluids at the exit of the boiler and evaporator are assumed to be saturated;
- The condenser has a given subcooling of 3 °C to prevent boiler feed pump cavitation;
- The flow through in the throttle valve is isenthalpic process.

According to the given thermodynamic assumptions, the mathematical models used to determine the thermodynamic performance characteristics of the studied hybrid (ORC–VCRC) system could be established.

3.2 Modelling of Components and Energy Analysis

After applying the first law of thermodynamics to various components of a combined (ORC–VCRC) system, the following mathematical models were constructed:

Organic Rankine Cycle (ORC):

Expander:

$$W_{exp} = m_{ORC}(h_1 - h_{2s})\eta_{exp} \quad (1)$$

Pump:

$$W_{pump} = \frac{m_{ORC}(h_{4s} - h_3)}{\eta_{pump}} \quad (2)$$

Boiler:

$$Q_{boil} = m_{ORC}(h_1 - h_4) \quad (3)$$

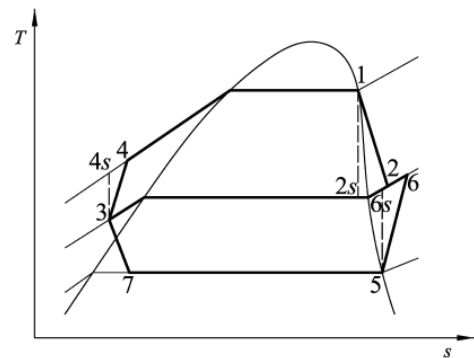
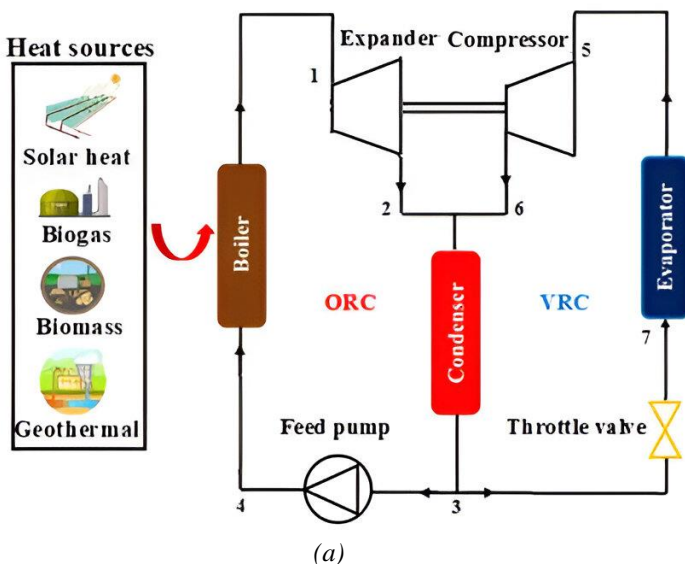


Figure 1. Schematic diagram (a) of (ORC–VCRC) system and its corresponding Temperature–entropy diagram (b).

The thermal efficiency of the organic Rankine cycle (ORC) is defined as:

$$\eta_{ORC} = \frac{W_{net}}{Q_{boil}} \quad (4)$$

Vapor Compression Refrigeration Cycle (VCRC):

Evaporator:

$$Q_{ev} = m_{VCRC}(h_5 - h_7) \quad (5)$$

Compressor:

$$W_{comp} = \frac{m_{VCRC}(h_5 - h_{6s})}{\eta_{comp}} \quad (6)$$

The COP of vapor compression refrigeration cycle (VCRC) is given by:

$$COP_{VCRC} = \frac{Q_{ev}}{W_{comp}} \quad (7)$$

With [14]:

$$W_{net} = W_{exp} - W_{pump} \quad (8)$$

$$W_{comp} = W_{net} \quad (9)$$

The overall coefficient of performance (COP_{oval}) of the hybrid (ORC–VCRC) system can be calculated as follows:

$$COP_{oval} = \eta_{ORC} COP_{VCRC} \quad (10)$$

The working fluid mass rate of per kW cooling capacity in the ORC–VCRC system is expressed as:

$$MkW = \frac{m_{ORC} + m_{VCR}}{Q_{ev}} \quad (11)$$

The expansion ratio in expander (EPR) and compression ratio in compressor (CMR) are calculated for the required compressor and expander sizes, respectively, and described as follows:

$$EPR = \frac{v_2}{v_1} \quad (12)$$

$$CMR = \frac{p_6}{p_5} \quad (13)$$

3.3 Operating Conditions for the Combined Power and Cooling (ORC–VCRC) Calculation

The operating conditions for the system calculation were:

- The temperature of heat source was 100 °C;
- The working fluid mass flow rate in ORC is taken to be 1.0 kg/s;
- The boiler temperature ranged from 60 to 90 °C;
- The condensation temperature ranged from 30 to 55 °C;
- The evaporation temperature ranged from -15 to 15 °C;

- The typical values of boiler temperature, condensation temperature and evaporation temperature are set as 80, 40 and 5 °C, respectively;
- The isentropic efficiency of the compressor, feed pump and expander are taken to be 75, 75 and 80 %, respectively [14].

Based on the assumptions and mathematical models above, a computer code was written and developed in MATLAB software and integrated with REFPROP Version 9.0. With the given input parameters, the code calculates all thermodynamic properties of each point of the (ORC–VCRC) system and simulate the thermodynamic performance characteristics of the hydrocarbons (propane, butane, isobutene, propylene, and cyclopentane) in (ORC–VCRC) system in a wide range of working conditions.

4. Results and Discussion

4.1 Model Validation

To validate the present model, the performance indicators (overall coefficient of performance (COP_{oval}) and working fluid mass flow rate of per kW cooling capacity (MkW)) have been compared with the available data in the literature using the isobutene as working fluid in hybrid (ORC–VCRC) system.

The results of this study were compared with the simulation data published by Li et al. [14] under the same operating conditions (boiler temperatures vary from (60 to 90 °C), constant condensation temperature of 40 °C, constant evaporation temperature of 5 °C). The simulation results are illustrated in Figure 2.

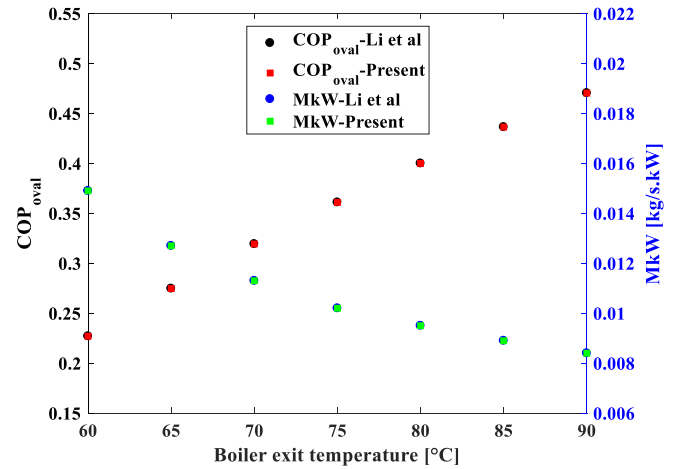


Figure 2. Validation of the present work.

Figure 2 shows an explicit agreement between the performance indicators results obtained in this study and the data published in the preceding literature.

The comparison results indicate that the deviation between the calculated performance indicators (COP_{oval} and MkW) and the reference values are small, with a mean deviation being 0.1 % and 0.2 % for COP_{oval} and MkW, respectively. These deviations are very acceptable and indicate that the developed model can calculate the thermodynamic performances of combined power and cooling (ORC–VCRC) system, which confirms the validity of our simulation model.

The following section presents the simulation results of the comparative evaluation of thermodynamic performance characteristics of the investigated hydrocarbons in (ORC–VCRC) system.

4.2 Performances Analysis

4.2.1 Effect of Boiler Exit Temperature

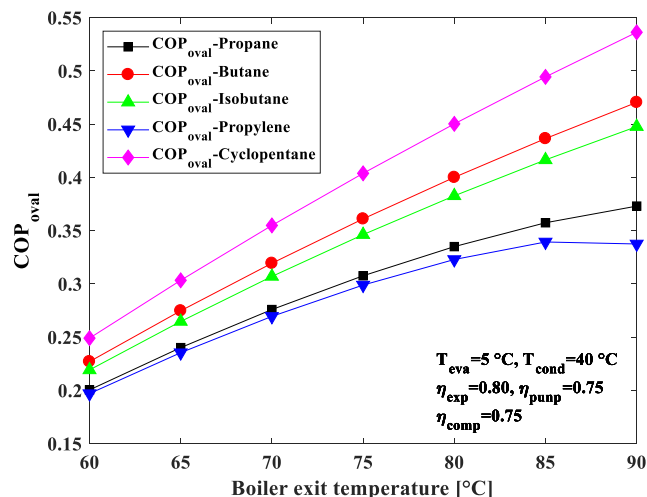


Figure 3. Effect of variation of boiler exit temperature on COP_{oval} .

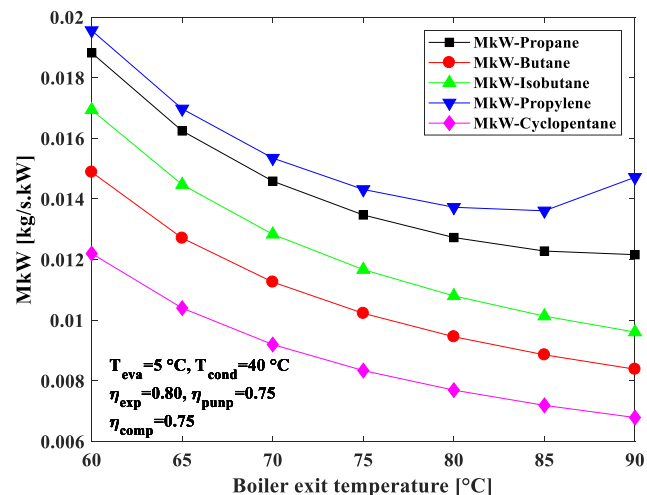


Figure 4. Effect of variation of boiler exit temperature on MkW .

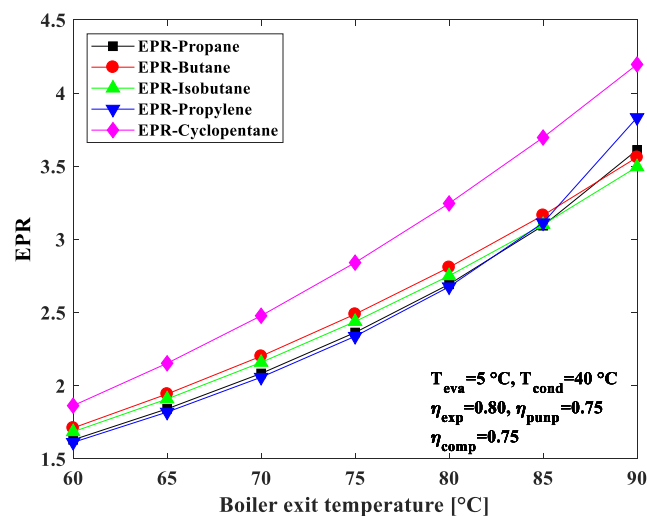


Figure 5. Effect of variation of boiler exit temperature on EPR .

Figure 3 illustrates the simulation results of the effect of variation of boiler exit temperature ($T_{boil}=60$ to 90 °C) on COP_{oval} of combined power and cooling (ORC–VCRC) system, while maintaining the other variables unchanged,

using the hydrocarbons: propane, butane, isobutene, propylene, and cyclopentane as working fluids.

From the curves of the variation of the COP_{oval} , it was noticed that the COP_{oval} keeps increasing as T_{boil} increases for each working fluid, where it can be observed that the lower value of boiler exit temperature ($T_{boil}=60$ °C) led to a lower value of COP_{oval} , however, as the T_{boil} increased, the COP_{oval} also increased. The following provides an explanation of the situation's cause. Both the compressor's cooling capability and power consumption are constant when the condenser and evaporator temperatures remain constant. Therefore, the COP_{VCRC} of VCRC system does not change. On the other hand, η_{ORC} of the ORC system will increase when boiler temperature increases and condenser temperature is constant. Since the input power to the compressor must be equal to the net output power of the expander, the ORC with a high boiler temperature produces the same power with a lower mass flow rate. This raises the ORC's thermal efficiency by reducing the amount of heat added to the boiler. The (ORC–VCRC) system becomes more efficient as the boiler temperature rises because of these two factors. On the other hand, the results showed that the maximum COP_{oval} of combined power and cooling (ORC–VCRC) system working with the propylene is lower than that obtained with the other studied working fluids, while for the cyclopentane, the COP_{oval} is higher than the obtained with butane, isobutene, propane and propylene for all the boiler exit temperature range studied. The results indicate that when boiler temperature reaches 90 °C, the COP_{oval} of cyclopentane increase by 14 %, 19.8 %, 43.8 %, and 59 % compared to those of butane, isobutene, propane and propylene, respectively.

When the boiler exit temperature increases from 60 to 90 °C, the COP_{oval} of the five working fluids (cyclopentane, butane, isobutene, propane, and propylene) increases from $(0.2490$ to $0.5362)$, $(0.2270$ to $0.4704)$, $(0.2192$ to $0.4476)$, $(0.2004$ to $0.3730)$ and $(0.1969$ to $0.3374)$, respectively.

Figure 4 exhibits the simulation results of the effect of variation of boiler exit temperature ($T_{boil}=60$ to 90 °C) on MkW of combined power and cooling (ORC–VCRC) system using the hydrocarbons: propane, butane, isobutene, propylene, and cyclopentane as working fluids.

From the curves of the variation of the MkW , it was noticed that the MkW keeps decreasing as boiler exit temperature increases for each working fluids, where it can be observed that the lower value of boiler exit temperature (60 °C) led to a higher value of MkW , however, as the boiler exit temperature increased, the MkW decreased.

By comparing the simulation results obtained, the results showed that the MkW of combined power and cooling (ORC–VCRC) system working with propylene is higher than that obtained with the other studied working fluids, while for cyclopentane, the MkW is lower than the obtained with propane, butane, isobutene and propylene for all the temperature range studied, which confirms that it could be a good working fluid for the (ORC–VCRC) system. The results indicate that at ($T_{boil}=90$ °C), the MkW of cyclopentane reduced by 19.1 %, 29.2 %, 44.3 %, and 53.7 % compared to those of butane, isobutene, propane, and propylene, respectively.

When the boiler exit temperature increases from 60 to 90 °C, the MkW of the five working fluids (cyclopentane, butane, isobutene, propane, and propylene) decreases from $(0.0122$ to $0.0068)$, $(0.0149$ to $0.0084)$, $(0.0169$ to $0.0096)$, $(0.0188$ to $0.0122)$ and $(0.0196$ to $0.0147)$, respectively.

The effect of the boiler exit temperature ($T_{\text{boil}}=60$ to 90 °C) on the expansion ratio in expander (EPR), while maintaining the other variables unchanged, using the hydrocarbons: propane, butane, isobutene, propylene and cyclopentane as working fluids is displayed in Figure 5.

As shown in the figure, like the COP_{oval} , the expansion ratio in expander (EPR) increases as the boiler exit temperature increases from 60 to 90 °C for all investigating working fluids. The following provides an explanation of the situation's cause. The boiler temperature (saturation pressure) increases while the temperature of the condenser (saturation pressure) is constant. As a result, the specific volume drops and the pressure at the expander inlet rises. The expansion ratio in expander (EPR) rises because of this.

From the curves of the variation of the expansion ratio in expander (EPR), it was noticed that the expansion ratio in expander (EPR) of combined power and cooling (ORC–VCRC) system, which working with the cyclopentane is higher than the obtained with the other working fluids.

When the boiler exit temperature increases from 60 to 90 °C, the EPR of the five working fluids (cyclopentane, butane, isobutene, propane, and propylene) increases from (1.8636 to 4.1951), (1.7112 to 3.5607), (1.6850 to 3.4951), (1.6302 to 3.6109) and (1.6126 to 3.8321), respectively.

4.2.2 Effect of Condensation Temperature

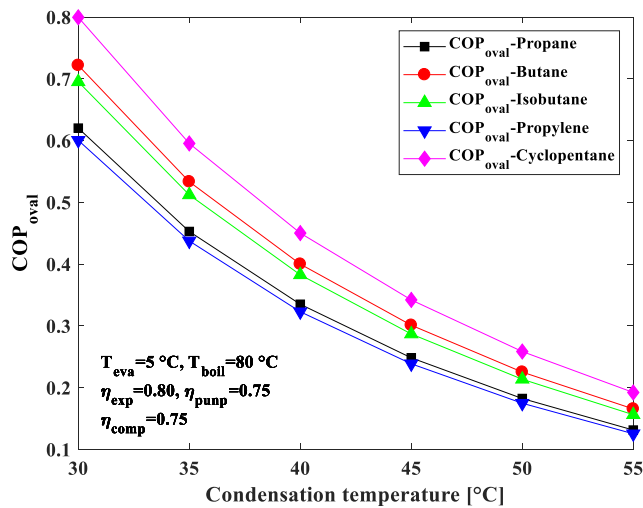


Figure 6. Effect of variation of condensation temperature on COP_{oval} .

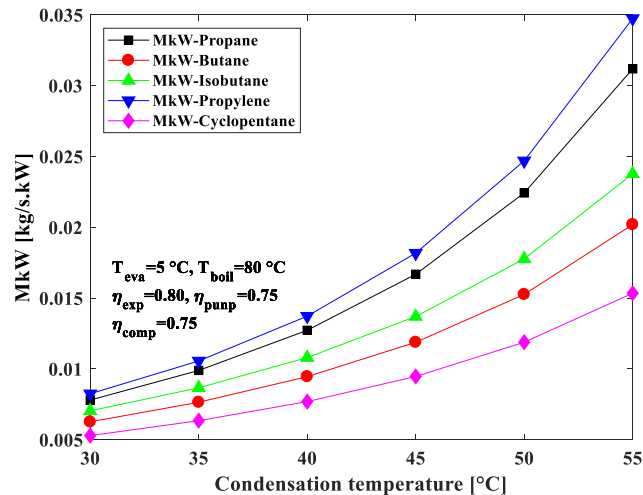


Figure 7. Effect of variation of condensation temperature on MkW .

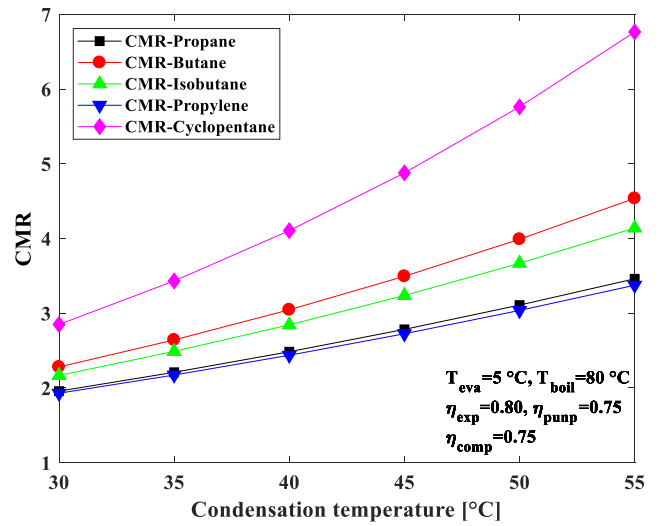


Figure 8. Effect of variation of condensation temperature on CMR .

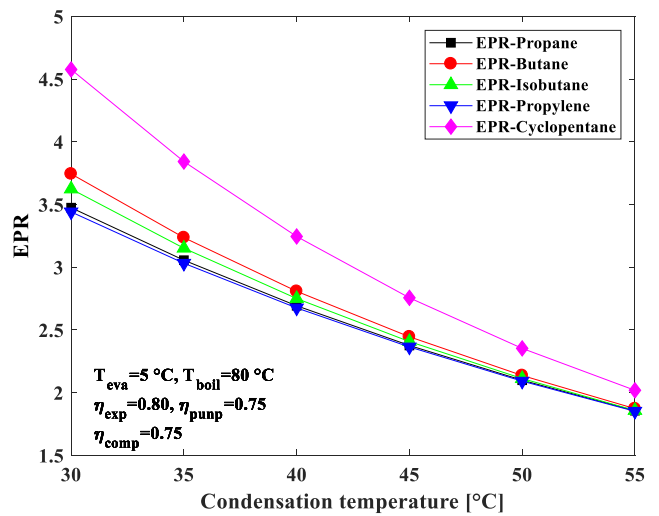


Figure 9. Effect of variation of condensation temperature on EPR .

Figure 6 illustrates the variation of condensation temperature ($T_{\text{cond}} = 30$ to 55 °C) on COP_{oval} of combined power and cooling (ORC–VCRC) system while maintaining the other variables unchanged, using the hydrocarbons: propane, butane, isobutene, propylene, and cyclopentane as working fluids.

As clearly shown in the figure, the results showed that the curves of the variation of the COP_{oval} decreases as condensation temperature increases for all the considered working fluids, where it can be observed that the lower value of condensation temperature (30 °C) led to a higher value of COP_{oval} , however, as the condensation temperature increases (55 °C), the COP_{oval} decreases.

As can be seen from equation (10) the COP_{oval} value of the combined power and cooling (ORC–VCRC) system is found by multiplying the thermal efficiency of ORC and coefficient of cooling performance of the VCRC. As the T_{cond} increases, the COP_{VCRC} value decreases as expected for all working fluids, while the evaporator temperature is constant. On the other hand, the η_{ORC} value decreases since the heat addition to the boiler increases while the condenser temperature is increasing.

According to the figure, the results showed that the COP_{oval} of combined power and cooling (ORC–VCRC) system working with the propylene is lower than that

obtained with the other studied working fluids, while for the cyclopentane, the COP_{oval} is higher than the obtained with propane, butane, isobutene and propylene for all the condensation temperature range studied.

The results indicate that at ($T_{cond}=30\text{ }^{\circ}\text{C}$), the COP_{oval} of cyclopentane increase by 16.1 %, 23 %, 46.4 % and 53.4 % compared to those of butane, isobutene, propane and propylene, respectively.

When the condensation temperature increases from 30 to 55 $^{\circ}\text{C}$, the COP_{oval} of the five working fluids (cyclopentane, butane, isobutene, propane and propylene) decreases from (0.7996 to 0.1922), (0.7218 to 0.1655), (0.6952 to 0.1562), (0.6201 to 0.1313) and (0.6004 to 0.1253), respectively.

Figure 7 represents the effect of variation of condensation temperature on MkW of combined power and cooling (ORC–VCRC) system while maintaining the other variables unchanged, using the hydrocarbons: propane, butane, isobutene, propylene and cyclopentane as working fluids. As can be observed in the figure, the MkW increases when increasing the temperature of the condenser from 30 to 55 $^{\circ}\text{C}$.

By comparing obtained results of MkW of each working fluids, the figure showed that the MkW of combined power and cooling (ORC–VCRC) system working with propylene is higher than that obtained with the other studied working fluids, while for cyclopentane, the MkW is lower than the obtained with propane, butane, isobutene and propylene for all the condensation temperature range studied.

The results indicate that at ($T_{cond}=30\text{ }^{\circ}\text{C}$), the MkW of cyclopentane reduced by 24.3 %, 35.7 %, 50.9 % and 55.9 % compared to those of butane, isobutene, propane, and propylene, respectively.

When the condensation temperature increases from 30 to 50 $^{\circ}\text{C}$, the MkW of the working fluids (cyclopentane, butane, isobutene, propane and propylene) increases from (0.0053 to 0.0153), (0.0063 to 0.0202), (0.0070 to 0.0238), (0.0078 to 0.0312) and (0.0082 to 0.0347), respectively.

Figure 8 shows the evolution of the compression ratio in compressor (CMR) of the combined power and cooling (ORC–VCRC) system with various condensation temperatures while maintaining the other variables unchanged, using the hydrocarbons: propane, butane, isobutene, propylene and cyclopentane as working fluids.

From the curves of the variation of the compression ratio in compressor (CMR), it was noticed that the compression ratio in compressor (CMR) keeps increasing as condensation temperature increases for each working fluids, where it can be observed that the lower value of condensation temperature (30 $^{\circ}\text{C}$) led to a lower value of CMR, however, as the condensation temperature increased (55 $^{\circ}\text{C}$), the compression ratio in compressor (CMR) increased.

The following provides an explanation of the situation's cause. The compressor saturation pressure rises and the compression ratio in compressor (CMR) value rises as the condenser temperature rises to the constant evaporator temperature (saturation pressure).

It can also be seen that cyclopentane has the highest values of compression ratio in compressor (CMR) compared to the other working fluids.

When the condensation temperature increases from 30 to 55 $^{\circ}\text{C}$, the compression ratio in compressor (CMR) of the working fluids (cyclopentane, butane, isobutene, propane and propylene) increases from (2.8497 to 6.7639), (2.2810 to 4.5365), (2.1675 to 4.1398), (1.9578 to 3.4606) and (1.9299 to 3.3746), respectively.

The effect of the condensation temperature on the expansion ratio in expander (EPR) of combined power and cooling (ORC–VCRC) system while maintaining the other variables unchanged, using the hydrocarbons: propane, butane, isobutene, propylene and cyclopentane as working fluids is displayed in Figure 9.

As shown in the figure, like the COP_{oval} , the expansion ratio in expander (EPR) decreases as the condensation temperature increases from 30 to 55 $^{\circ}\text{C}$ for all investigating working fluids.

From the curves of the variation of the EPR, it was noticed that the maximum EPR of combined power and cooling (ORC–VCRC) system, which is working with the cyclopentane is better than the obtained with the other working fluids. Additionally, it was found that the values of the EPR of the propane are like propylene for all the condensation temperature range studied.

When the condensation temperature increases from 50 to 60 $^{\circ}\text{C}$, the EPR of the five working fluids (cyclopentane, butane, isobutene, propane and propylene) decreases from (4.5767 to 2.0190), (3.7443 to 1.8729), (3.6239 to 1.8586), (3.4750 to 3.4606) and (3.4412 to 1.8520), respectively.

4.2.3 Effect of Evaporation Temperature

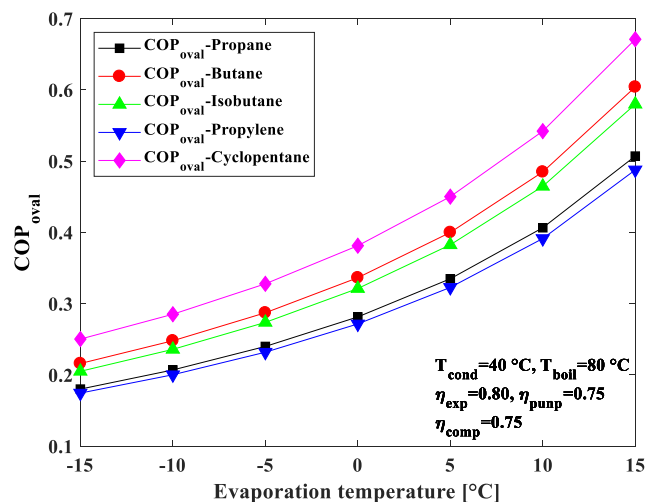


Figure 10. Effect of variation of evaporation temperature on COP_{oval} .

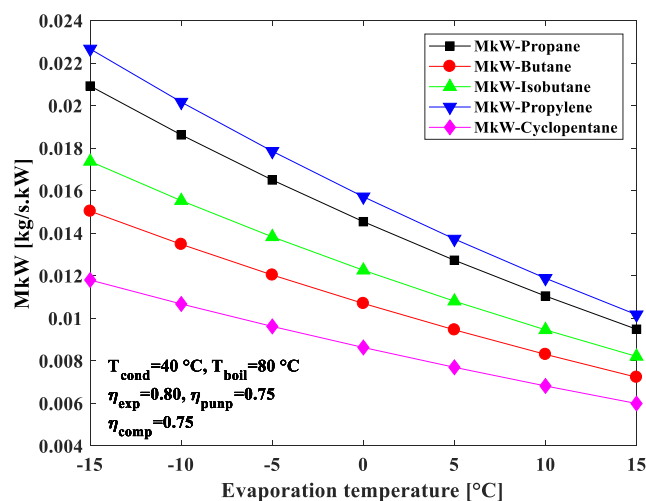


Figure 11. Effect of variation of evaporation temperature on MkW.

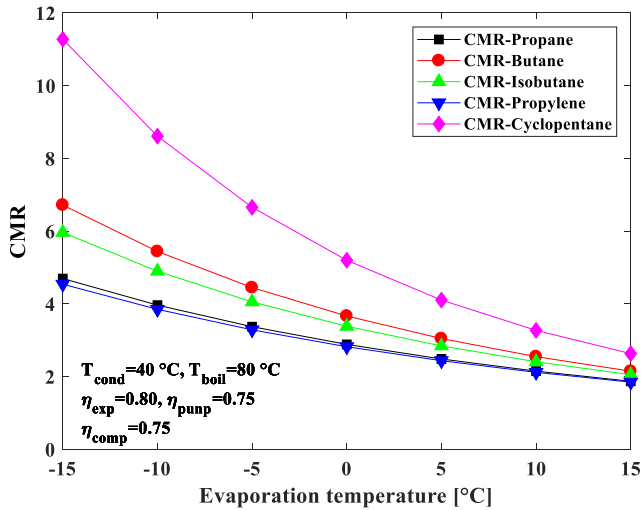


Figure 12. Effect of variation of evaporation temperature on CMR.

The effect of evaporation temperature ($T_{eva}=-15$ to 15 °C) on the COP_{oval} of combined power and cooling (ORC–VCRC) system while maintaining the other variables unchanged is displayed in Figure 10.

As shown in figure, the curves of the variation of the COP_{oval} keeps increasing as T_{eva} increases for each working fluids, where it can be observed that the lower value of evaporation temperature ($T_{eva}=-15$ °C) led to a lower value of COP_{oval} , however, as the T_{eva} increased, the COP_{oval} also increased.

The following provides an explanation of the situation's cause. The evaporator capacity increases and the compressor pressure ratio decreases with increased evaporator temperature (saturation pressure) at constant condenser temperature, resulting in a reduction in the compressor's power consumption. This also increases the value of COP_{VCRC} of VCRC system. On the other hand, the η_{ORC} value does not change. Because of these two effects, the COP_{oval} increases as the T_{eva} increases.

On other hand, it was noticed that the best performing working fluid is the cyclopentane. The results indicate that at ($T_{eva}=15$ °C), the COP_{oval} of cyclopentane increase by 11.1 %, 15.7 %, 32.3 %, and 37.6 % compared to those of butane, isobutene, propane and propylene, respectively.

When the evaporation temperature increases from -15 to 15 °C, the COP_{oval} of the working fluids (cyclopentane, butane, isobutene, propane and propylene) increases from (0.2503 to 0.6710), (0.2161 to 0.6041), (0.2051 to 0.5799), (0.1802 to 0.5071) and (0.1745 to 0.4877), respectively.

Figure 11 gives the effect of variation of evaporation temperature on MkW for the combined power and cooling (ORC–VCRC) system operating with the working fluids (propane, butane, isobutene, propylene, and cyclopentane) while maintaining the other variables unchanged.

From the curves of the variation of the MkW, it was noticed that the MkW keeps decreasing as evaporation temperature increases for each working fluids, where it can be observed that the lower value of evaporation temperature ($T_{eva}=-15$ °C) led to a higher value of MkW, however, as the T_{eva} increased, the MkW decreased.

The results indicate that at ($T_{eva}=15$ °C), the MkW of cyclopentane reduced by 16.7 %, 26.9 %, 36.9 %, and 41.2 % compared to those of butane, isobutene, propane, and propylene, respectively.

When the evaporation temperature (T_{eva}) increases from -15 to 15 °C, the MkW of the five working fluids (cyclopentane, butane, isobutene, propane and propylene) decreases from (0.0118 to 0.0060), (0.0150 to 0.0072), (0.0174 to 0.0082), (0.0209 to 0.0095) and (0.0227 to 0.0102), respectively.

The effect of evaporation temperature on the CMR of the combined power and cooling (ORC–VCRC) system is plotted in Figure 12.

It can be observed from figure that the lower value of evaporation temperature ($T_{eva}=-15$ °C) led to a higher value of CMR, however, as the evaporation temperature increased, the CMR decreased.

The following provides an explanation of the situation's cause. Increased evaporator temperature (saturation pressure) at the constant condenser temperature causes the compressor pressure ratio to decrease.

When the evaporation temperature (T_{eva}) increases from -15 to 15 °C, the CMR of the five working fluids (cyclopentane, butane, isobutene, propane and propylene) decreases from (11.2766 to 2.6321), (6.7171 to 2.1487), (5.9651 to 2.0511), (4.6958 to 1.8720) and (4.5409 to 1.8481), respectively.

4.2.4 Effect of Expander Isentropic Efficiency

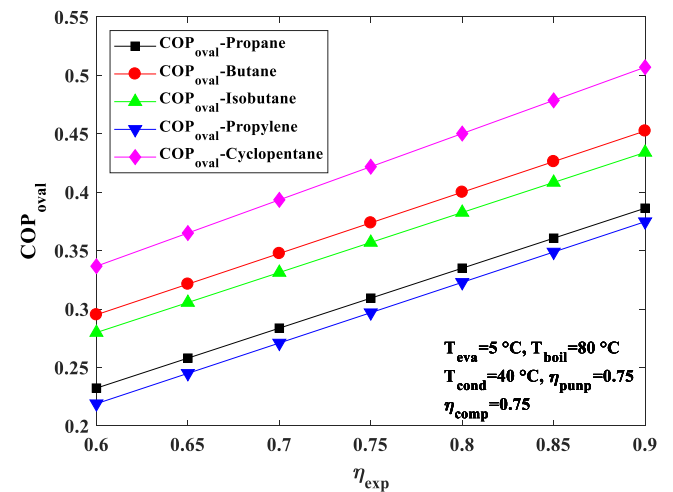


Figure 13. Effect of expander isentropic efficiency on COP_{oval} .

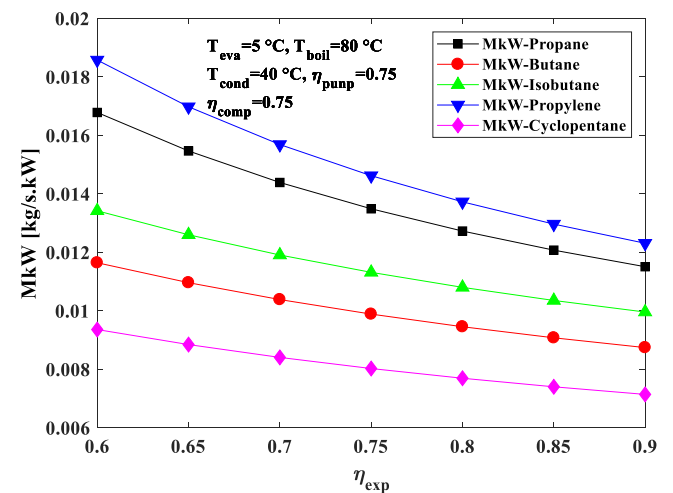


Figure 14. Effect of expander isentropic efficiency on MkW.

Figure 14 reveals the variation of overall coefficient of performance (COP_{oval}) by varying the expander isentropic

efficiency ($\eta_{exp}=0.6$ to 0.9) for the combined power and cooling system (organic Rankine cycle (ORC)–vapor compression refrigeration cycle (VCRC)) activated by low-temperature renewable energies operating with the investigated working fluids (propane, butane, isobutene, propylene, and cyclopentane).

From the results obtained, it can be observed that an increase in the expander isentropic efficiency leads to a gradual increase in overall coefficient of performance for all investigated working fluids.

The maximum COP_{oval} of system working with the propylene is lower than that obtained with the other studied working fluids, while for the cyclopentane, the COP_{oval} is higher than the obtained with butane, isobutene, propane, and propylene.

The results indicate that at expander isentropic efficiency of 0.9 , the overall coefficient of performance of cyclopentane increase by 12.1% , 16.9% , 31.1% , and 35.3% compared to those of butane, isobutene, propane, and propylene, respectively.

When the expander isentropic efficiency increases from 0.6 to 0.9 , the overall coefficient of performance of the working fluids (cyclopentane, butane, isobutene, propane, and propylene) increases from $(0.3367$ to $0.5070)$, $(0.2951$ to $0.4524)$, $(0.2799$ to $0.4340)$, $(0.2323$ to $0.3868)$ and $(0.2190$ to $0.3748)$, respectively.

The effect of expander isentropic efficiency on MkW of the (ORC–VCRC) system is plotted in Figure 14.

From the simulated results, it can be observed that the MkW curves of the working fluids decreases with the increasing of the expander isentropic efficiency.

The results indicate that at ($\eta_{exp}=0.9$), the MkW of cyclopentane reduced by 18.4% , 29% , 38.3% , and 42.3% compared to those of butane, isobutene, propane, and propylene, respectively.

When the expander isentropic efficiency increases from 0.6 to 0.9 , the MkW of the (cyclopentane, butane, isobutene, propane, and propylene) decreases from $(0.0094$ to $0.0071)$, $(0.0116$ to $0.0087)$, $(0.0134$ to $0.0100)$, $(0.0168$ to $0.0115)$, $(0.0186$ to $0.0123)$, respectively.

4.2.5 Effect of Compressor Isentropic Efficiency

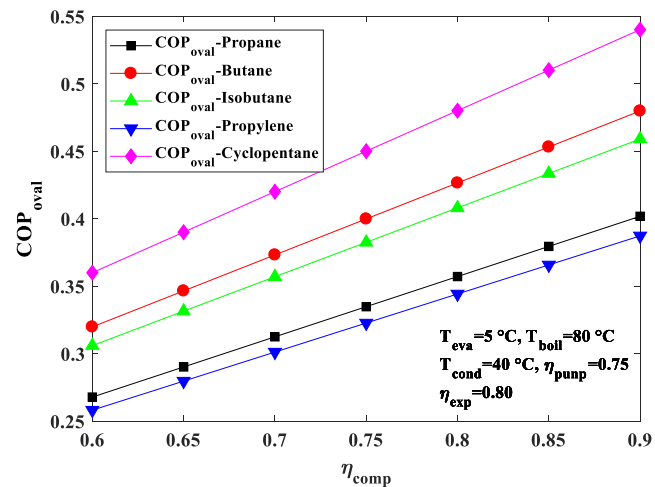


Figure 15. Effect of compressor isentropic efficiency on COP_{oval} .

Figure 15 shows the effect of compressor isentropic efficiency on COP_{oval} for the combined power and cooling

(ORC–VCRC) system operating with the working fluids (propane, butane, isobutene, propylene, and cyclopentane).

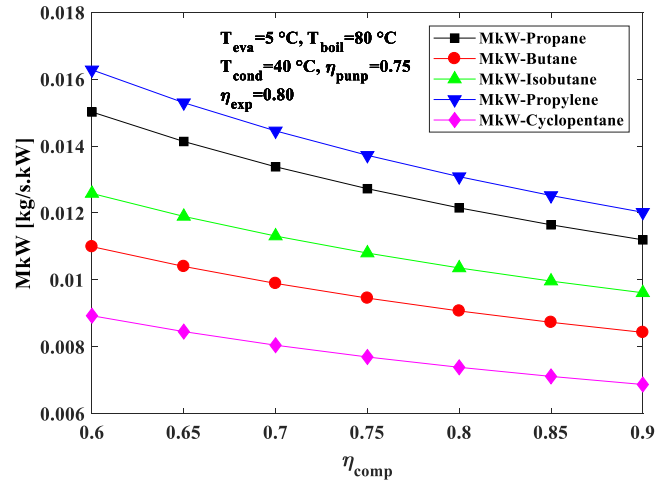


Figure 16. Effect of compressor isentropic efficiency on MkW.

From the simulation results obtained, it is seen that an increase in the compressor isentropic efficiency leads to a gradual increase in COP_{oval} for all working fluids. The results indicate that at ($\eta_{comp}=0.9$), the COP_{oval} of cyclopentane increase by 12.6% , 17.7% , 34.4% and 39.5% compared to those of butane, isobutene, propane and propylene, respectively.

When the compressor isentropic efficiency increases from 0.6 to 0.9 , the COP_{oval} of the five working fluids (cyclopentane, butane, isobutene, propane and propylene) increases from $(0.3602$ to $0.5403)$, $(0.3200$ to $0.4800)$, $(0.3061$ to $0.4592)$, $(0.2680$ to $0.4020)$ and $(0.2583$ to $0.3874)$, respectively.

Figure 16 gives the simulation results of the variation of the MkW values of the (ORC–VCRC) system for working fluids versus the compressor isentropic efficiency ($\eta_{comp}=0.6$ to 0.9). As can be observed in the figure, the MkW decreases when increasing the efficiency of the compressor.

The results indicate that at ($\eta_{comp}=0.9$), the MkW of cyclopentane reduced by 17.9% , 28.1% , 38.4% and 42.5% compared to those of butane, isobutene, propane and propylene, respectively.

When the compressor isentropic efficiency increases from 0.6 to 0.9 , the MkW of the (cyclopentane, butane, isobutene, propane, and propylene) decreases from $(0.0089$ to $0.0069)$, $(0.0110$ to $0.0084)$, $(0.0126$ to $0.0096)$, $(0.0150$ to $0.0112)$, $(0.0163$ to $0.0120)$, respectively.

5. Conclusions

This study examined the theoretical use of power from ORC using renewable energy sources with low temperature heat sources in VCRC system for cooling using cyclopentane gas as promising working fluid to replace the conventional hydrocarbons (butane, isobutene, propane, and propylene) widely used in (ORC–VCRC) system.

A comparative examination of the performance characteristics of (ORC–VCRC) system between the working fluids are presented. The performance characteristics investigated are (performance indicators (overall coefficient of performance (COP_{oval}) and working fluid mass flow rate of per kW cooling capacity (MkW), expansion ratio in expander (EPR) and compression ratio in compressor (CMR)). Furthermore, the effects of different

operating parameters (e.g., boiler, condenser, and evaporator temperatures, isentropic efficiency of expander (η_{exp}), and isentropic efficiency of compressor (η_{comp})) on performance indicators are also examined for each working fluid.

The simulation was realized by adjusting the boiler temperature between 60°C and 90°C, the condenser temperature between 30°C and 55°C, and the evaporator temperature between -15°C and 15°C.

Based on the results obtained from the present study, the main conclusions are listed as follows:

- The COP_{oval} rises as the boiler and evaporator temperatures rises. Conversely, when the condenser temperature rises, the COP_{oval} value falls for all fluids;
- The MkW value falls as the boiler and evaporator temperatures rises. Conversely, when the condenser temperature rises, the COP_{oval} value rises for all fluids;
- The EPR rises as the boiler temperatures rises. Conversely, when the condenser temperatures rises, the EPR value falls for all fluids;
- The CMR rises as the condenser temperatures rises. Conversely, when the evaporator temperatures rises, the CMR value falls for all fluids;
- The COP_{oval} rises as the expander isentropic efficiency rises. Conversely, when this parameter rises, the MkW value falls for all fluids;
- The COP_{oval} rises as the compressor isentropic efficiency rises. Conversely, when this parameter rises, the MkW value falls for all fluids;
- The maximum COP_{oval} of (ORC–VCRC) system is obtained with cyclopentane;
- The minimum COP_{oval} of (ORC–VCRC) system is obtained with propylene;
- The maximum MkW of (ORC–VCRC) system is obtained with propylene;
- The minimum MkW of (ORC–VCRC) system is obtained with cyclopentane;

By analyzing the performance characteristics of studied working fluids, the investigated cyclopentane gas emerges better performances in most of the cases, which confirms that it could be a promising working fluid in terms of performance indicators for (ORC–VCRC) system.

In future works, it would be very interesting to research about a novel design of a power-cooling system using cyclopentane gas as working fluid to improve the performance indicators of the conventional (ORC–VCRC) system.

Nomenclature

Symbols

COP_{VCRC}	: Coefficient of performance of VCRC
COP_{oval}	: Overall coefficient of performance of the hybrid ORC–VCRC system
CMR	: Compression ratio in compressor
EPR	: Expansion ratio in expander
h	: Specific enthalpy (kJ kg^{-1})
p	: Pressure (kPa)
m	: Mass flow rate (kg s^{-1})
MkW	: Working fluid mass flow rate of per kW cooling capacity ($\text{kg s}^{-1} \text{ kW}^{-1}$)
s	: Specific entropy ($\text{kJ kg}^{-1} \text{ K}^{-1}$)
v	: Specific volume ($\text{m}^3 \text{ kg}^{-1}$)
Q_{boil}	: Boiler heat input (kW)
Q_{ev}	: Evaporator cooling capacity (kW)
W_{comp}	: Compressor work input (kW)

W_{exp}	: Expander work output (kW)
W_{net}	: Net work output (kW)
W_{pump}	: Pump power consumption (kW)
T	: Temperature (°C)

Greek symbols

η_{comp}	: Isentropic efficiency of compressor
η_{exp}	: Isentropic efficiency of expander
η_{pump}	: Isentropic efficiency of pump
η_{ORC}	: Power cycle thermal efficiency

Subscripts

$cond$: Condensing process
eva	: Evaporation process
$boil$: Boiler process
s	: Isentropic process
ORC	: Organic Rankine cycle
$VCRC$: Vapor compression refrigeration cycle
$1, 2, 3, \dots$: Respective state points in the hybrid (ORC–VCRC) system

Abbreviations

ORC	: Organic Rankine cycle
$VCRC$: Vapor compression refrigeration cycle
GWP	: Global warming potential
ODP	: Ozone depleting potential

References:

- [1] P. Gang, L. Jing, J. Jie, “Design and analysis of a novel low-temperature solar thermal electric 465 system with two-stage collectors and heat storage units,” *Renew. Energy.*, 36, 2324–2333, 2011, doi:10.1016/j.renene.2011.02.008.
- [2] M. Ciani Bassetti, D. Consoli, G. Manente, A. Lazzaretto, “Design and off-design models of a 468 hybrid geothermal-solar power plant enhanced by a thermal storage,” *Renew. Energy.*, 128, 460–472, 2018, doi:10.1016/j.renene.2017.05.078.
- [3] H.Cho, A.D, Smith, P .Mago, “Combined cooling, heating and power: a review of performance improvement and optimization,” *Applied Energy.*, 136, 168–185, 2014, doi:10.1016/j.apenergy.2014.08.107.
- [4] H. Chang, Z. Wan, Y. Zheng, X. Chen, S. Shu, Z. Tu, S.H. Chan, “Energy analysis of a hybrid PEMFC-solar energy residential micro CCHP system combined with an organic Rankine cycle and vapor compression cycle,” *Energy Conversion and Management.*, 142, 374–384, 2017, doi:10.1016/j.enconman.2017.03.057.
- [5] C. Yue, F. You, Y. Huang, “Thermal and economic analysis of an energy system of an ORC coupled with vehicle air conditioning,” *International Journal of Refrigeration.*, 64, 152–167, 2016, doi:10.1016/j.ijrefrig.2016.01.005.
- [6] J.M. Calm, “The next generation of refrigerants-historical review, considerations, and Outlook,” *International Journal of Refrigeration.*, 31, 1123–1133, 2008, doi:10.1016/j.ijrefrig.2016.01.005.
- [7] N.Abas, A.R.Kalair, N.Khan, A.Haider, Z.Saleem, M.S.Saleem, “Natural and synthetic refrigerants, global warming: A review.,” *Renew. Sustain. Energy Rev.*, 90, 557–569, 2018, doi:10.1016/j.rser.2018.03.099.
- [8] S.Wang, C. Liu, Q. Li, L. Liu, E. Huo, C. Zhang, “Selection principle of working fluid for organic

- Rankine cycle based on environmental benefits and economic performance,” *Applied Thermal Engineering.*, 178, 115598, 2020, doi:10.1016/j.applthermaleng.2020.115598.
- [9] J. Bao, L. Zhao, “A review of working fluid and expander selections for organic Rankine cycle,” *Renew Sustain Energy Rev.*, 24, 325–42, 2013, doi:10.1016/j.rser.2013.03.040.
- [10] B. Saleh, “Parametric and working fluid analysis of a combined organic Rankine-vapor compression refrigeration system activated by low-grade thermal energy,” *Journal of Advanced Research.*, 7, 651–660, 2016, doi:10.1016/j.jare.2016.06.006.
- [11] S. Aphornratana, T. Sriveerakul, “Analysis of a combined Rankine-vapour compression refrigeration cycle,” *Energy Conversion and Management.*, 51, 2557–2564, 2010, doi:10.1016/j.enconman.2010.04.016.
- [12] M. Asim, M.K.H. Leung, Z. Shan, Y. Li, D.Y.C. Leung, M. Ni, “Thermodynamic and thermo-economic analysis of integrated organic Rankine cycle for waste heat recovery from vapor compression refrigeration cycle,” *Energy Procedia*, 143, 192–198, 2017, doi:10.1016/j.egypro.2017.12.670.
- [13] F. Molés, J. Navarro-Esbri, B. Peris, A. Mota-Babiloni, K. Kontomaris, “Thermodynamic analysis of a combined organic Rankine cycle and vapor compression cycle system activated with low temperature heat sources using low GWP fluids,” *Applied Thermal Engineering.*, 87, 444–453, 2015, doi:10.1016/j.applthermaleng.2015.04.083.
- [14] H. Li, X. Bu, L. Wang, Z. Long, Y. Lian, “Hydrocarbon working fluids for a Rankine cycle powered vapor compression refrigeration system using low-grade thermal energy,” *Energy Build.*, 65, 167–172, 2013, doi:10.1016/j.enbuild.2013.06.012.
- [15] X. Bu, L. Wang, H. Li, “Performance analysis and working fluid selection for geothermal energy-powered organic Rankine-vapor compression air conditioning,” *Geotherm Energy.*, 1, 1–14, 2013, doi:10.1186/2195-9706-1-2.
- [16] H. Wang, R. Peterson, K. Harada, E. Miller, R. Ingram-Goble, L. Fisher, “Performance of a combined organic Rankine cycle and vapor compression cycle for heat activated cooling,” *Energy.*, 36, 447–458, 2011, doi:10.1016/j.energy.2010.10.020.
- [17] M.O. Nazer, S.M. Zubair, “Analysis of Rankine cycle air-conditioning systems,” *ASHRAE Journal.*, 88, 332–334, 1982.
- [18] A.N. Egrican, A. Karakas, “Second law analysis of a solar powered Rankine cycle/vapor compression cycle,” *Journal of Heat Recovery Systems.*, 6, 135–141, 1986, doi:10.1016/0198-7593(86)90073-1.
- [19] K.H. Kim, H. Perez-Blanco, 2015, “Performance analysis of a combined organic Rankine cycle and vapor compression cycle for power and refrigeration cogeneration,” *Applied Thermal Engineering.*, 91, 964–974, 2015, doi:10.1016/j.applthermaleng.2015.04.062.
- [20] J. Jeong, Y.T. Kang, “Analysis of a refrigeration cycle driven by refrigerant steam turbine,” *International Journal of Refrigeration.*, 27, 33–41, 2004, doi:10.1016/S0140-7007(03)00101-4.
- [21] B. Hu, J. Guo, Y. Yang, Y. Shao, “Performance analysis and working fluid selection of organic Rankine steam compression air conditioning driven by ship waste heat,” *Energy Reports.*, 8, 194–202, 2022, doi:10.1016/j.egy.2022.01.094.
- [22] S. Khatoon, N.M.A. Almeftreji, M.H. Kim, “Thermodynamic study of a combined power and refrigeration system for low-grade heat energy source,” *Energies.*, 14, no. 2, 410, 2021, doi:10.3390/en14020410.
- [23] E. Cihan and B. Kavasogullari, “Energy and exergy analysis of a combined refrigeration and waste heat driven organic rankine cycle system,” *Thermal science.*, 21, no. 6A, 2621–2631, 2017, doi:10.2298/TSCI150324002C.
- [24] B. Kavasogullari, E. Cihan, H. Demir, “Energy and Exergy Analyses of a Refrigerant Pump Integrated Dual-Ejector Refrigeration (DER) System,” *Arabian Journal for Science and Engineering.*, 46, 11633–11644, 2021, doi:10.1007/s13369-021-05541-7.
- [25] E.O. Küçük and M. Kılıç, “Exergoeconomic and Exergetic Sustainability Analysis of a Combined Dual-Pressure Organic Rankine Cycle and Vapor Compression Refrigeration Cycle,” *Sustainability.*, 15, no. 8, 6987, 2023, doi: 10.3390/su15086987.
- [26] A.K.S. Al-Sayyab, A. Mota-Babiloni, J. Navarro-Esbri, “Performance Evaluation of Modified Compound Organic Rankine-Vapour Compression Cycle with Two Cooling Levels, Heating, and Power Generation,” *Appl Energy.*, 334, 120651, 2023, doi: 10.1016/j.apenergy.2023.120651.
- [27] R. Zhar, A. Allouhi, M. Ghodbane, A. Jamil, K. Lahrech, “Parametric analysis and multi-objective optimization of a combined Organic Rankine Cycle and Vapor Compression Cycle,” *Sustainable Energy Technologies and Assessments.*, 47, 101401, 2021, doi:10.1016/j.seta.2021.101401.
- [28] Z. Wang, Y. Zhao, X. Xia, S. Zhang, Y. Xiao, X. Zhang, W. Chen, “Experimental study of the thermodynamic performance of the ORC-VCC system with a zeotropic mixture,” *Applied Thermal Engineering.*, 250, 123534, 2024, doi: 10.1016/j.applthermaleng.2024.123534.
- [29] D.M. Ginosar, L.M. Petkovic, D.P. Guillen, “Thermal Stability of Cyclopentane as an Organic Rankine Cycle Working Fluid,” *Energy Fuels.*, 25, 9, 4138–4144, 2011, doi:10.1021/ef200639r.
- [30] Y. Maalem, Y. Tamene, H. Madani, “Behavior of the thermo-physical properties and performance evaluation of the refrigerants blends of (Fluorocarbon/Hydrocarbon) for cooling cycle,” *Recueil de Mécanique.*, 6, 544–559, 2022, doi:10.5281/zenodo.5918533.
- [31] J.S. Lim, J.Y. Park, J.W. Kang, B.G. Lee, “Measurement of vapor–liquid equilibria for the binary systems of propane + 1,1,1,2-tetrafluoroethane and 1,1,1-trifluoroethane + propane at various temperatures,” *Fluid Phase Equilibria.*, 243, 57–63, 2006, doi:10.1016/j.fluid.2006.02.016.

- [32] S. Bobbo, R. Stryjek, N. Elvassore, A. Bertucco, "A recirculation apparatus for vapor-liquid equilibrium measurements of refrigerants. Binary mixtures of R600a, R134a and R236fa," *Fluid Phase Equilibria.*, 150, 343-352, 1998, doi:10.1016/S0378-3812(98)00334-3.
- [33] Q.N. Ho, B.G. Lee, J.Y. Park, J.D. Kim, J. S. Lim, "Measurement of vapor-liquid equilibria for the binary mixture of propylene (R-1270)+1,1,1,2-tetrafluoroethane (HFC-134a)," *Fluid Phase Equilibria.*, 225, 125-132, 2004, doi:10.1016/j.fluid.2004.08.028.
- [34] L. Fedele, S. Bobbo, R. Camporese, M. Scattolini, "Isothermal vapour+liquid equilibrium measurements and correlation for the pentafluoroethane+cyclopropane and the cyclopropane+1,1,1,2-tetrafluoroethane binary systems," *Fluid Phase Equilibria.*, 251, 41-46, 2007, doi:10.1016/j.fluid.2006.10.023.
- [35] N. Lim, G. Seong, H. Roh, "Vapor-Liquid Equilibria for the 1,1,1,2-Tetrafluoroethane (HFC-134a)+n-Butane (R-600) System," *J. Chem. Eng. Data.*, 52, 1313-1318, 2007, doi:10.1021/je700041v.
- [36] Y. Maalem, S. Fedali, H. Madani, Y. Tamene, "Performance analysis of ternary azeotropic mixtures in different vapor compression refrigeration cycles," *International Journal of Refrigeration.*, 119, 139-151, 2020, doi:10.1016/j.ijrefrig.2020.07.021.

Research Article

Highly Efficient Energy Integration: Thermodynamic Analysis of Heat Recovered from SOFC Through S-CO₂ And Kalina Cycles

¹*A. Elbir 

¹Suleyman Demirel University Renewable Energy Resources Research and Application Center
E-mail: ¹*ahmetelbir@sdu.edu.tr

Received 19 May 2024, Revised 28 Sep 2024, Accepted 14 Nov 2024

Abstract

This study focuses on the implementation of a highly efficient energy integration using solid oxide fuel cell (SOFC) technology. A detailed thermodynamic analysis of the integration of heat energy obtained from SOFC into the Supercritical Carbon Dioxide (S-CO₂) cycle and the Kalina cycle aims to assess its effectiveness, sustainability, and economic performance in energy systems. The study presents a thermodynamic analysis encompassing the integration of SOFC technology into an energy system, as well as the integration of the heat energy obtained into the S-CO₂ cycle, Kalina cycle, and hot water production. The high energy efficiencies, low carbon emissions, and economic advantages individually achieved by SOFC, S-CO₂ cycle, and Kalina cycle are significantly enhanced when integrated into a cohesive system. The integrated system analysis results show an energy efficiency of 89.1%, an exergy efficiency of 64.6%, and an exergetic sustainability index of 0.83, demonstrating that this integration provides an energy solution with high efficiency, sustainability, and a low carbon footprint. Thermodynamic analyses were performed using the EES (Engineering Equation Solver) software. The main contribution of this study is the introduction of innovative approaches to energy efficiency and exergy analysis. The system achieves high energy efficiency through the integration of SOFC and the Kalina cycle. Particularly, optimizing the thermal management of the SOFC and utilizing the ammonia-water mixture more efficiently in the Kalina cycle brings significant improvements in the system's energy and exergy efficiency. These analyses demonstrate higher efficiency and sustainability compared to existing systems, emphasizing the originality of this approach.

Keywords: Solid oxide fuel cell; supercritical CO₂; kalina cycle; energy analysis; exergy analysis.

1. Introduction

In research aimed at enhancing the efficiency and sustainability of modern energy systems, there is a growing emphasis on the high potential of heat recovered from solid oxide fuel cells (SOFC) in energy recycling. In this context, this study presents a thermodynamic analysis of a highly efficient energy integration strategy involving the integration of heat obtained from SOFC power sources into the Supercritical Carbon Dioxide (S-CO₂) cycle and the Kalina cycle, respectively. The analysis aims to contribute significantly to the field of sustainable energy production by thoroughly evaluating the system's performance in terms of energy and exergy.

Numerous studies in the field have proposed innovative Combined Cooling, Heating, and Power (CCHP) systems, all built upon the concept of energy cascading. Among these, a notable system, integrating SOFC/GT (Solid Oxide Fuel Cell/Gas Turbine) and trans-critical CO₂ power/cooling cycles, showcased impressive capabilities, delivering 48.37 kW of cooling, 240.65 kW of heating, and 250.95 kW of net electricity production, with power generation and exergetic efficiency levels reaching 62.65% and 62.27%, respectively [1]. In its configuration, the excess heat generated by the proton exchange membrane (PEM) fuel cells is designed to be efficiently recovered using an organic Rankine cycle

(ORC) system, further supported by a liquefied natural gas (LNG) subsystem for efficient heat exchange within the ORC. A comprehensive exergo-environmental analysis was conducted to assess the ecological impacts of irreversible processes occurring in the system. In this proposed setup, PEM fuel cells serve as the primary power generation source. Outputs from both the ORC and LNG subsystems are used to develop a transcritical CO₂ compression refrigeration system and to provide a reverse osmosis desalination unit. This integrated approach enables the system to achieve a fresh water production rate of 6 kg/s along with 1214 kW of electricity, 1116 kW of cooling capacity and 161.1 kW of heating capacity [2]. Furthermore, a groundbreaking cogeneration system, combining a gas turbine cycle, a supercritical CO₂ cycle, and a Kalina cycle, has emerged for integrated heating and power generation purposes. Comprehensive energy, exergy, and exergoeconomic analyses have been conducted to assess the system's performance and feasibility. The study findings unveil remarkable energy and exergy efficiencies of 78.15% and 40.97%, respectively. Economic scrutiny under specific pricing conditions reveals a promising payback period of 6.9 years and a net present value of \$5.374 million [3]. Additionally, a newly devised cogeneration setup effectively merges solid oxide fuel cell (SOFC), internal combustion

engine (ICE), supercritical carbon dioxide (S-CO₂) power cycle, and heat recovery steam generators (HRSG). With a combined output power of 345.58 kW and a net output power of 288.94 kW, the system attains an economical unit cost of 42.98 \$/GJ, coupled with theoretical and actual generation efficiencies of 48.00% and 40.13%, respectively. Noteworthy is the overall energy efficiency reaching 65.82%, complemented by an exergy efficiency of 42.28% [4]. This investigation unveils a system composed of a solid oxide fuel cell (SOFC), a solar tower facility, and a (S-CO₂) Brayton cycle. Through multi-objective optimization, it is demonstrated that integrating an additional simple S-CO₂ cycle and a re-compression S-CO₂ cycle leads to notable achievements, including an exergy efficiency of 56.86% and a total system economic ratio of 513.10 \$/hour, with specific metrics of 56.45% for exergy efficiency and 481.59 \$/hour for total system economic ratio [5]. Furthermore, the introduction of a biomass-based solid oxide fuel cell (SOFC)-supported poly-generation system marks a significant advancement. Integrating a transcritical CO₂ cycle, re-compression (S-CO₂) Brayton cycle, and a double-effect LiBr absorption refrigerator, the system attains exceptional performance metrics, boasting an overall efficiency of 93.00% and an exergy efficiency of 29.95%. Under optimal conditions, the system can generate a maximum net power of 99.66 kW when the SOFC inlet temperature is set at 550°C and the current density reaches 3680 A/m² [6]. Moreover, in the proposed integrated system, waste heat from the SOFC is efficiently recovered through a Kalina cycle, enhancing overall efficiency. Additionally, simultaneous cooling and power supply functions are fulfilled by utilizing waste heat from the Kalina cycle for liquefied natural gas (LNG) cold flow. Results underscore the system's efficacy, achieving approximately 55% exergy efficiency and 60% energy efficiency at a current density of 550 A/m² [7]. Implementing a Kalina cycle for waste heat recovery from the SOFC stack and employing a thermoelectric generator to harness heat emitted from the Kalina condenser, this system demonstrates notable energy and exergy efficiencies of 58% and 54%, respectively, under optimal conditions [8]. The study further explores the integration of an organic Rankine cycle (ORC) into a solid oxide fuel cell (SOFC)-gas turbine (GT) hybrid power system. R123zd(E) is selected as the working fluid for the ORC, showcasing significant energy and exergy efficiencies of 55.67% and 53.55%, respectively, under specific conditions. Economic and environmental evaluations under design conditions reveal a total cost rate of \$36.09 per hour, with CO₂ emissions (EMI) at 355.8 kg/MWh. Comparative thermodynamic analyses indicate an 11.72% increase in exergy efficiency in the SOFC-GT-ORC configuration compared to the hybrid SOFC-GT cycle, highlighting the superiority of the hybrid SOFC-GT-ORC system. Moreover, the study suggests the potential utilization of alternative ORC working fluids such as R123, R601a, and R245fa in future applications [9]. Furthermore, a hybrid PV-SOFC system is analyzed by integrating actual load profiles and solar/air data into the system model. The PV and SOFC subsystems achieve maximum power outputs of 70 kWe and 152 kWe, respectively. The SOFC subsystem demonstrates average net electrical and total efficiencies of 30.3% and 70.0%, with peak values reaching 37.5% and 75.6%. [10]. In this system configuration, a (SOFC), a miniature gas turbine (MGT), a (S-CO₂) Brayton cycle, and a lithium bromide absorption refrigerator are integrated. By efficiently

capturing waste heat from the SOFC-MGT combination using the S-CO₂ Brayton cycle, surplus electricity is generated. The excess heat from the MGT's exhaust is utilized for household heating and, via a lithium bromide absorption refrigerator, for both heating and cooling purposes, achieving an energetic return efficiency of 70.49% and an electrical efficiency of 60.59% [11]. Additionally, a Combined Heat and Power (CHP) system employing an SOFC is introduced. The study investigates the influence of various factors such as cell temperature, pressure, fuel utilization coefficient, and system air-to-fuel ratio on the performance of the SOFC-CHP setup. Reforming, electrochemical, and thermal models are concurrently introduced and solved to attain precise outcomes. Graphs depicting power and heat generation, as well as cell voltage loss, are generated under diverse operational conditions. It is observed that cell power increases with rising temperature and pressure, with temperature exhibiting a more pronounced effect. Moreover, the overall efficiency of the SOFC-CHP system is estimated to be approximately 73%. Finally, the optimal air-to-fuel ratio and fuel utilization coefficient are determined to be 9.4 and 0.85, respectively [12]. Their research has facilitated the integration of biomass gasification with (SOFC) technology. The hydrogen produced is introduced into the biomass gasification-SOFC system, proposing two distinct configurations. In the first configuration, hydrogen is directed into the anode inlet to provide a hydrogen-rich fuel, while in the second proposed configuration, it is injected into the SOFC's afterburner to elevate the gas turbine inlet temperature. These configurations undergo a thorough assessment and comparison from thermodynamic, environmental, and economic perspectives. It is evident that injecting hydrogen into the anode demonstrates superior performance in the system. Under the optimal operation of this configuration, the exergy efficiency, CO₂ emissions, and electricity cost are determined to be 24.85%, 0.257 kg/kWh, and 0.0911 \$/kWh, respectively [13]. The relationship between heat transfer rate and entropy generation for single pressure and dual pressure waste heat recovery boilers has been examined. It has been stated that entropy generation per heat transfer is less in dual pressure boilers than in single pressure boilers because the temperature difference of heat transfer is less in dual pressure boilers. The analyses have shown that larger boilers (dual pressure) are both more efficient in terms of heat transfer and have less entropy generation per heat transfer [14]. They used the Kalina cycle instead of conventional methods for waste heat recovery. A system was designed with the Kalina cycle instead of the Rankine cycle. The designed system achieved an estimated efficiency increase of approximately 30%. The net power obtained from the Kalina cycle was calculated to be around 550 kW, whereas for the Rankine cycle, this value was calculated to be 420 kW. They stated that the Kalina cycle resulted in an annual fuel savings of 610.18 tons and a thermal efficiency increase of 4.8% [15]. They examined superheated and saturated vapor ORCs. A parametric study was conducted using different organic fluids to determine the best operating conditions for the system and to evaluate the findings of conventional exergy-based analyses. Conventional exergy and exergoeconomic analyses were calculated [16]. A theoretical performance analysis based on the exergetic performance coefficient, coefficient of performance (COP), exergy efficiency, and exergy destruction ratio criteria was conducted for a multipurpose refrigeration system using different

refrigerants under serial and parallel operating conditions. The exergetic performance coefficient criterion was defined as the ratio of exergy output to the total exergy destruction rate (or loss rate of availability) [17].

The imperative to enhance energy system efficiency and ensure sustainability is escalating in contemporary times. Within this context, the spotlight on the latent potential of heat derived from solid oxide fuel cells (SOFC) for waste heat recovery and the imperative of leveraging energy resources more effectively is progressively intensifying. This study posits that the integration of heat sourced from SOFCs into (S-CO₂) and Kalina cycles holds promise for augmenting overall system efficiency. Such integration harbors the prospect of judiciously exploiting waste heat and curbing carbon emissions. In contrast to antecedent studies, the proposed energy integration methodology focalizes on amalgamating SOFC heat with S-CO₂ and Kalina cycles. The distinctive feature of this study lies in its provision of novel perspectives on energy efficiency and waste heat utilization, thereby bridging extant gaps in the literature. While drawing upon antecedent research on energy integration strategies and waste heat recovery, this study's novelty lies in furnishing a comprehensive thermodynamic analysis of the amalgamation of SOFC heat with S-CO₂ and Kalina cycles, thus addressing a lacuna in the existing literature. The selection of S-CO₂ and Kalina cycles stems from their inherent advantages, including high efficiency, scalability, and proficient waste heat utilization. Nonetheless, the drawbacks of these systems, such as technological intricacy and cost implications, warrant consideration. The antecedent studies referenced in the introduction play a pivotal role in elucidating the subject matter. This study's contribution is underscored by its augmentation of existing literature and revelation of the potential inherent in integrating SOFC heat with S-CO₂ and Kalina cycles.

The motivation of this study is to present new approaches to increase the efficiency of existing energy systems and minimize energy losses. It is aimed to optimize energy recovery using solid oxide fuel cell (SOFC) technology and integrated thermodynamic systems. The study aims to increase energy efficiency especially by integrating SOFC's waste heat into the Super Critical Carbon Dioxide (S-CO₂) cycle and Kalina cycle. With this approach, both energy saving is achieved and sustainability is targeted with low carbon emissions. The study offers significant innovations in energy systems by providing higher energy and exergy efficiency compared to existing systems.

2. Methodology

The Solid Oxide Fuel Cell (SOFC) operates under steady-state conditions, meaning the system is modeled to function in equilibrium. The pressure within the system remains constant. This assumption implies that pressure is maintained at a continuous value throughout the analysis. The operation of the SOFC is considered ideal, assuming a fuel utilization rate of 100%. Real-world losses and interactions are not taken into account. The mixture ratio of fuel and oxidant is assumed to be ideal, reflecting a stoichiometric reaction assumption. The SOFC operates within a constant thermal bath at a specific temperature. Variations in temperature are not considered. The temperatures of the exhaust gases are equal to the temperature of the SOFC cells, indicating the condition of the gases within the cells. All heat transfer occurs within the

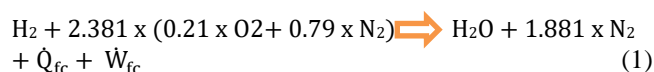
environmental temperature limits between the cells. Heat transfer between cells is constrained within the environmental temperature limits. The SOFC operates in a thermodynamically reversible state, with irreversible entropy changes. The electrochemical reaction occurring at the anode represents the chemical reactions at both the cathode and anode of the SOFC. These reactions depict the interaction of fuel and oxidant through electrochemical processes. Air consists of 21% oxygen and 79% nitrogen, with an ambient temperature of 25°C and 1 bar. Considering hydrogen's purity and performing calculations on a unit mass/time basis, the flow rate is determined as 1 kmol/s, a considerably high flow rate. The operating temperature of the SOFC is set at 1000°C. The temperature in all heat exchangers is calculated with a 0.7 efficiency ratio. The Higher Heating Value of Hydrogen (HHV_{H₂}) is 285830 kJ/kmol [12]. [13]. [18].

2.1. Assumptions For Thermodynamic Analysis Of S-CO₂ Cycle And Kalina Cycle

The system exhibits stable and consistent performance, indicating that the operating conditions of the system are predetermined and continue steadily. Only pure substances are used in the system, allowing for the use of ideal conditions in analysis and calculations. Compression processes for the compressor and pump occur adiabatically, signifying minimal interaction of energy transfer with the external environment. Pressure drops in system components and heat transfer in the pipeline are ignored in the analysis, reducing complexity and indicating theoretical modeling. The dead state of the circulating fluids in all cycles is considered as standard conditions: 25°C temperature and 1 bar atmospheric pressure. The system demonstrates regular and stable performance, implying that system parameters are under control, and expected values are approached consistently. In the analysis, the gravitational potential energy and kinetic energy of the fluids in the system are neglected, assuming these energy types have negligible effects on the system's performance in practice.

2.2. Assumptions For Thermodynamic Analysis Of SOFC

SOFC is generally a type of fuel cell that produces electrical energy through an electrochemical reaction between a fuel (usually hydrogen or methane) and an oxidant (typically oxygen in the air). Electrochemical reactions take place at the anode and cathode electrodes of the SOFC. The electrochemical reactions occurring at the anode and cathode electrodes of the SOFC are defined as equations, such as Equation 1 [18]:



Equation 1 represents the electrochemical reaction of a solid oxide fuel cell (SOFC). SOFC produces electrical energy through a reaction between a fuel, such as hydrogen, and a mixture of oxygen and nitrogen in the air. This reaction occurs in the electrochemical process at the anode of the SOFC. The terms in the equation are as follows: Hydrogen (H₂) is the fuel supplied to the anode of the SOFC; Oxygen (O₂) is the primary oxidizing agent in the air; Nitrogen (N₂) is an inert gas present in the air; Water (H₂O) is produced as a result of the reaction; \dot{Q}_{fc} represents the heat flow from the

SOFC; \dot{W}_{fc} represents the electrical energy generated by the SOFC.

The first law of thermodynamics can be written as Equation 2:

$$\dot{N}_{H_2} \times h_{H_2}|_{in} + \dot{N}_{O_2} \times h_{O_2}|_{in} + \dot{N}_{N_2} \times h_{N_2}|_{in} - \dot{N}_{H_2O} \times h_{H_2O}|_{out} - \dot{N}_{N_2} \times h_{N_2}|_{out} + \dot{Q}_{fc} + \dot{W}_{fc} = 0 \quad (2)$$

Equation 2 represents the energy balance of a solid oxide fuel cell (SOFC). In this equation, the sum of enthalpy values of the inflowing and outflowing streams to the SOFC equals the heat and electric energy generated by the SOFC. The terms in the equation include: the molar flow rate of hydrogen (\dot{N}_{H_2}), the molar enthalpy of inflowing hydrogen ($h_{H_2}|_{in}$), the molar flow rate of oxygen (\dot{N}_{O_2}), the molar enthalpy of inflowing oxygen ($h_{O_2}|_{in}$), the molar flow rate of nitrogen (\dot{N}_{N_2}), the molar enthalpy of inflowing nitrogen ($h_{N_2}|_{in}$), the molar flow rate of water (\dot{N}_{H_2O}), the molar enthalpy of outflowing water ($h_{H_2O}|_{out}$), the molar flow rate of outflowing nitrogen (\dot{N}_{N_2}), and the molar enthalpy of outflowing nitrogen ($h_{N_2}|_{out}$). Additionally, the terms representing the heat flow from the SOFC (\dot{Q}_{fc}) and the electric energy flow from the SOFC (\dot{W}_{fc}) are included in the equation.

The second law of thermodynamics can be expressed as Equation 3.

$$\dot{N}_{H_2} \times s_{H_2}|_{in} + \dot{N}_{O_2} \times s_{O_2}|_{in} + \dot{N}_{N_2} \times s_{N_2}|_{in} - \dot{N}_{H_2O} \times s_{H_2O}|_{out} - \dot{N}_{N_2} \times s_{N_2}|_{out} + \frac{\dot{Q}_{fc}}{T_{fc}} + \dot{S}_{fc} = 0 \quad (3)$$

Equation 3 represents the entropy balance of a solid oxide fuel cell (SOFC). In this equation, the sum of the entropies of the inflowing and outflowing streams to and from the SOFC is equal to the total entropy production from the SOFC ($\frac{\dot{Q}_{fc}}{T_{fc}}$) divided by the absolute temperature of the cell (T_{fc}) and the entropy production rate due to irreversibility ($-\dot{S}_{fc}$). The terms in the equation are as follows: the molar flow rate of hydrogen (\dot{N}_{H_2}), the molar entropy of inflowing hydrogen ($s_{H_2}|_{in}$), the molar flow rate of oxygen (\dot{N}_{O_2}), the molar entropy of inflowing oxygen ($s_{O_2}|_{in}$), the molar flow rate of nitrogen (\dot{N}_{N_2}), the molar entropy of inflowing nitrogen ($s_{O_2}|_{in}$), the molar flow rate of water vapor (\dot{N}_{H_2O}), the molar entropy of outflowing water vapor ($s_{H_2O}|_{out}$), the molar flow rate of nitrogen leaving the system (\dot{N}_{N_2}), and the molar entropy of outflowing nitrogen ($s_{N_2}|_{out}$). Additionally, the term representing the entropy production rate due to irreversibility ($-\dot{S}_{fc}$) is divided by the absolute temperature of the cell (T_{fc}).

Here, \dot{N} is the molar flow rate, "h" is the specific molar enthalpy, "S" is the specific molar entropy, "T_{fc}" is the absolute temperature of the fuel cell, and \dot{S}_g is the entropy production rate due to irreversibility. In this context, h_{in} represents the enthalpy per mole of H₂ transported, while s_{in} and s_{out} denote the amounts of reactant inlet and reaction product outlet, respectively, per mole of H₂ taken from the system by the exhaust. The variables s_{in} and s_{out} are analogous to h_{in} and h_{out} , respectively. All these variables can be determined by the following expressions Equations (4),(5),(6),(7):

$$h_{in} = (h_{H_2} + 0.5xh_{O_2} + 1.881x h_{N_2})_{in} \quad (4)$$

$$h_{out} = (h_{H_2O} + 1.881x h_{N_2})_{out} \quad (5)$$

$$s_{in} = (s_{H_2} + 0.5xs_{O_2} + 1.881xs_{N_2})_{in} \quad (6)$$

$$s_{out} = (s_{H_2O} + 1.881xs_{N_2})_{out} \quad (7)$$

If we assume an ideal, energy-neutral process, the entropy generation is zero. The ideal power of the cell Equation (8):

$$\dot{W}_{fc} = -\dot{N}_{H_2} \times (\Delta h - T_{fc} \times \Delta s) \quad (8)$$

When $\Delta h = h_{out} - h_{in}$ and $\Delta s = s_{out} - s_{in}$, the enthalpy and entropy changes for the fuel cell reaction, respectively.

Given that the Gibbs free energy is expressed as $g = h - T \times s$, the equivalent for isothermal processes can be rewritten as equation (9):

$$\dot{W}_{fc} = \dot{N}_{H_2} \times (g_{in} - g_{out}) = -\dot{N}_{H_2} \times \Delta g \quad (9)$$

Note that the previous equation is valid under the condition that reactants and product flows are at the default operating temperature of the cell. In this study, as the cell does not operate isothermally (reactants are at a lower temperature than the cell), eq. (9) is not applicable, and eq. (8) has been used to calculate the ideal power of the SOFC.

When the ideal power is obtained, efficiency can be formulated as follows when the maximum possible Process is reversible Equation (10):

$$\eta_{fc} = \frac{\dot{W}_{fc}}{-\dot{N}_{H_2} \times \Delta h} = \frac{\Delta h - T \times \Delta s}{\Delta h} \quad (10)$$

Equation 10 represents the efficiency of a (SOFC), which is defined as the ratio of the work output (\dot{W}_{fc}) to the heat input ($-\dot{N}_{H_2} \times \Delta h$). This can also be expressed as the ratio of the change in enthalpy (Δh) minus the product of the temperature (T) and the change in entropy (Δs) to the change in enthalpy (Δh).

In the non-isothermal process examined in this study, where the temperature of reactants is lower than that of the products, and under certain conditions, the Δs term can be greater than zero. In this scenario, equation (9) would imply that the fuel cell system absorbs heat from the surroundings and converts it entirely into electrical energy, potentially achieving a fuel cell efficiency higher than unity. However, this scenario is not feasible; thus, operating at the claimed temperature of the cell is unattainable, and the outlet temperature of the products will be lower [19].

Finally, in this study, the Δh (enthalpy change) used in equations (9) and (10) is not based on the higher heating value or lower heating value of the fuel; instead, it is based on the actual enthalpy change for the fuel cell reaction.

Thermodynamic analyses for the S-CO₂ cycle and Kalina cycle:

For steady state in thermodynamic analysis. the basic mass balance equation can be given as follows Equation (11) [20]. [21]. [22];

$$\sum \dot{m}_{in} = \sum \dot{m}_{ex} \quad (11)$$

The mass flow rate is denoted by \dot{m} , where the 'in' and 'ex' indices signify the inlet and outlet states, respectively. Equation (12) represents the energy balance:

$$\dot{Q}_{in} + \dot{W}_{in} + \sum_{in} \dot{m} \left(h + \frac{v^2}{2} + gz \right) = \dot{Q}_{ex} + \dot{W}_{ex} + \sum_{ex} \dot{m} \left(h + \frac{v^2}{2} + gz \right) \quad (12)$$

At this point, \dot{Q} denotes the heat transfer rate, while \dot{W} represents power. Specific enthalpy is denoted by h , velocity by v , height by z , and gravitational acceleration by g . Equation (13) expresses the entropy balance equation under steady-state conditions:

$$\sum_{in} \dot{m}_{in} s_{in} + \sum_k \frac{\dot{Q}_k}{T_k} + \dot{S}_{gen} = \sum_{ex} \dot{m}_{ex} s_{ex} \quad (13)$$

Here, s represents the specific entropy, and \dot{S}_{gen} denotes the entropy generation rate. Equation (14) presents the exergy balance equation.

$$\sum \dot{m}_{in} ex_{in} + \sum \dot{E}x_{Q,in} + \sum \dot{E}x_{W,in} = \sum \dot{m}_{ex} ex_{ex} + \sum \dot{E}x_{Q,ex} + \sum \dot{E}x_{W,ex} + \dot{E}x_D \quad (14)$$

Equation 14, known as the exergy balance equation, expresses the conservation of exergy within a system. On the left side of the equation, incoming exergy flows are summed. These flows include the exergy values of the substances entering the system ($\sum \dot{m}_{in} ex_{in}$), the exergy associated with incoming heat transfer ($\sum \dot{E}x_{Q,in}$), and the exergy associated with incoming work transfer ($\sum \dot{E}x_{W,in}$). On the right side of the equation, outgoing exergy flows are summed. These flows include the exergy values of the substances leaving the system ($\sum \dot{m}_{ex} ex_{ex}$), the exergy associated with outgoing heat transfer ($\sum \dot{E}x_{Q,ex}$), and the exergy associated with outgoing work transfer ($\sum \dot{E}x_{W,ex}$). Additionally, the equation includes the exergy related to the work transfer applied externally to the system ($\dot{E}x_D$).

The specific flow exergy can be written as Equation (15):

$$ex = ex_{ph} + ex_{ch} + ex_{pt} + ex_{kn} \quad (15)$$

The kinetic and potential components of exergy are considered negligible. Additionally, the chemical exergy is assumed to be insignificant. The physical or flow exergy (ex_{ph}) is defined by Equation (16):

$$ex_{ph} = (h - h_o) - T_o(s - s_o) \quad (16)$$

In this context, h and s denote specific enthalpy and entropy, respectively. In real scenarios, h_o and s_o refer to enthalpy and entropy at reference medium states, respectively.

Exergy destruction is calculated as the product of specific exergy and mass, as expressed in Equation (17):

$$\dot{E}x_D = ex * m \quad (17)$$

The exergy ratios related to work, denoted as $\dot{E}x_D$, are provided by Equation (18):

$$\dot{E}x_D = T_o \dot{S}_{gen} \quad (18)$$

The exergy ratios related to work, denoted as $\dot{E}x_W$, are provided by Equation (19):

$$\dot{E}x_W = \dot{W} \quad (19)$$

$\dot{E}x_Q$. are the exergy rates related to heat transfer and are given as below Equation (20).

The exergy rates related to heat transfer, denoted as $\dot{E}x_Q$, are given by Equation (20) below.

$$\dot{E}x_Q = \left(1 - \frac{T_o}{T} \right) \dot{Q} \quad (20)$$

Exergy destruction within the system Equation (21);

$$\dot{E}x_{D,syst} = \dot{E}x_{in} - \dot{E}x_{aut} \quad (21)$$

What work comes out of the system Equation (22);

$$\dot{W}_{net,out} = \dot{Q}_{in} - \dot{Q}_{out} \quad (22)$$

System thermal efficiency (η) Equation (23);

$$\eta = \frac{\text{energy in exit outputs}}{\text{total energy inlets}} \quad (23)$$

The exergy efficiency (ψ) can be defined as follows Equation (24);

$$\psi = \frac{\text{exergy in exit outputs}}{\text{total exergy inlets}} \quad (24)$$

2.3. Exergoenvironmental Analysis For Integrated System

Shows exergoenvironmental impact factor. $\dot{E}x_{D,tot}$. is total exergy destruction rate. $\dot{E}x_{D,in}$. is input exergy rate Equation (25) [23].

fei represents the exergoenvironmental impact factor $\dot{E}x_{D,tot}$, denotes the total exergy destruction rate, while $\dot{E}x_{D,in}$. represents the input exergy rate, as described in Equation (25) [23]

$$fei = \frac{\dot{E}x_{D,tot}}{\dot{E}x_{D,in}} \quad (25)$$

Cei is exergoenvironmental impact coefficient. ψ_{ex} represents exergy efficiency of the system Equation (26):

$$Cei = \frac{1}{\psi_{ex/100}} \quad (26)$$

Φei represents the exergoenvironmental impact index, as defined in Equation (27).

$$\Phi ei = fei \times Cei \quad (27)$$

Φeii represents the improvement in exergoenvironmental impact, as described in Equation (28).

$$\Phi eii = \frac{1}{\Phi ei} \quad (28)$$

fes is the exergy stability factor, defined by Equation (29).

$$fes = \frac{\dot{E}x_{D,out}}{\dot{E}x_{D,out} + \dot{E}x_{D,tot}} \quad (29)$$

$\Phi fest$ represents exergetic sustainability index Equation (30).

$$\Phi_{est} = f_{es} \times \Phi_{eii} \quad (30)$$

To evaluate the carbon emissions stemming from electricity consumption, the formula [24] multiplies the direct energy consumption denoted as "E" by the carbon intensity factor "eCO₂". In this context, "E" represents the emissions quantity derived by subtracting the net power of the subcycle from the overall net power Equation (31):

$$\text{Carbon Emissions} = E \times eCO_2 \quad (31)$$

Countries can be categorized based on the carbon intensity of electricity generation, with three primary groups: Group A, exhibiting a carbon intensity of up to 0.29 kg.CO₂/kWh; Group B, ranging between 0.30 and 0.69 kg.CO₂/kWh; and Group C, exceeding 0.70 kg.CO₂/kWh [25].

The reduction in integrated system power production cost is determined by subtracting the net power gained from waste heat from the initially obtained net power, dividing this result by the system efficiency, and then multiplying it by the designated electricity price for cost assessment Equation (32):

$$\text{electricitycost} = \frac{\text{Power gained}}{\text{cycle efficiency}} * \text{electricityprice} \quad (32)$$

Electricity Cost represents the economic aspect of electricity per unit. Power Gained denotes the energy acquired by the system. Cycle Efficiency signifies the efficiency of the energy conversion cycle. With a carbon intensity of 0.50 kg.CO₂/kWh [25] and a unit electricity price of 0.14 \$/kWh [26].

This equation provides a metric for understanding the economic implications of electricity generation per unit, considering the energy obtained, the efficiency of the energy conversion cycle, and the specific carbon intensity and unit electricity price values used in the calculation.

2.4. Overview Of The System

The diagram in Figure 1 illustrates the integrated power generation facility, which underwent thermodynamic analysis.

The system utilizes hydrogen (H₂) as the primary fuel. Hydrogen is directed from the storage tank to (SOFC) system through a heat exchanger-I. The pure hydrogen (The phrase 'facilitating a more rapid transformation' implies that the controlled introduction of pure hydrogen into the anode of the SOFC during its initial stages helps accelerate the conversion process. In other words, this controlled manner of introducing hydrogen at the beginning of the operation of the SOFC aids in speeding up the chemical reactions taking place within the fuel cell, resulting in a quicker onset of electricity generation.) is introduced to the anode of the SOFC in a controlled manner during its initial stages, facilitating a more rapid transformation. The oxidant employed in the system is a gas containing air. The air is heated through a separate heat exchanger-II. Subsequently, the preheated air is directed to the cathode of the SOFC. At the cathode, a reaction between oxygen and oxygen occurs, releasing electrons. The electrochemical outcomes at the anode and cathode involve the conversion of the chemical energy of hydrogen and oxygen into electrical energy and heat. These released electrons flow through the circuit, generating electrical energy [18].

The waste heat from the SOFC is initially transferred to a S-CO₂ cycle. Compressed CO₂ is directed to the heat absorption system, utilizing the high-temperature waste heat from the SOFC. At this stage, the waste heat from the SOFC expands the supercritical CO₂ by adding heat to it. The supercritical CO₂, now carrying the absorbed heat, expands through a turbine, producing energy. After electricity generation, the CO₂ gas is cooled and prepared for compression again to ensure the continuity and readiness for reuse. These steps enable the efficient utilization of waste heat in the supercritical carbon dioxide cycle. By converting waste heat into electrical energy, this system can enhance overall energy efficiency [18].

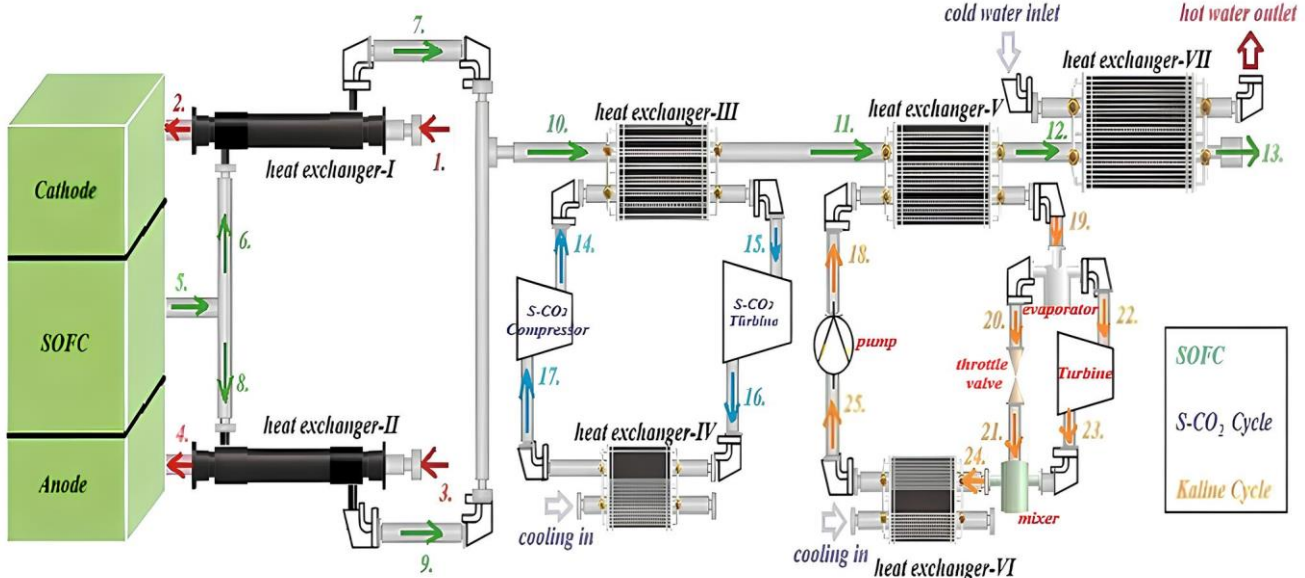


Figure 1. Integrated power generation facility with thermodynamic analysis.

In the second stage of waste heat from the SOFC, it is transferred to the heat exchanger-V containing a Kalina solution. The waste heat causes the solution to evaporate, triggering the evaporation reaction within the solution due to its low temperature. The evaporated solution expands through a turbine, producing electrical energy. The spent solution is condensed in a condenser. Additionally, a partition valve releases the high-pressure solution into a low-pressure region, ensuring pressure balance. This allows for the release and separation of vapor within the solution. The condensed solution is redirected to the heat exchanger, initiating a cycle. The heat generated during the condensation of the solution is returned to the heat exchanger to reuse the waste heat from the SOFC, constituting a heat recovery step that enhances the system's efficiency. The Kalina cycle is specifically designed for energy production from low-temperature heat sources, such as waste heat from SOFC. The evaporation and condensation within the solution, operating at low temperatures, increase the efficiency of the cycle. One of the advantages of this system is its applicability in various industrial processes and waste heat sources. Heat recovery aids in improving system efficiency, contributing to the reduction of overall energy consumption [19].

3. Findings And Discussion

3.1. Results For SOFC Analysis

Figure 2 shows the SOFC flowchart.

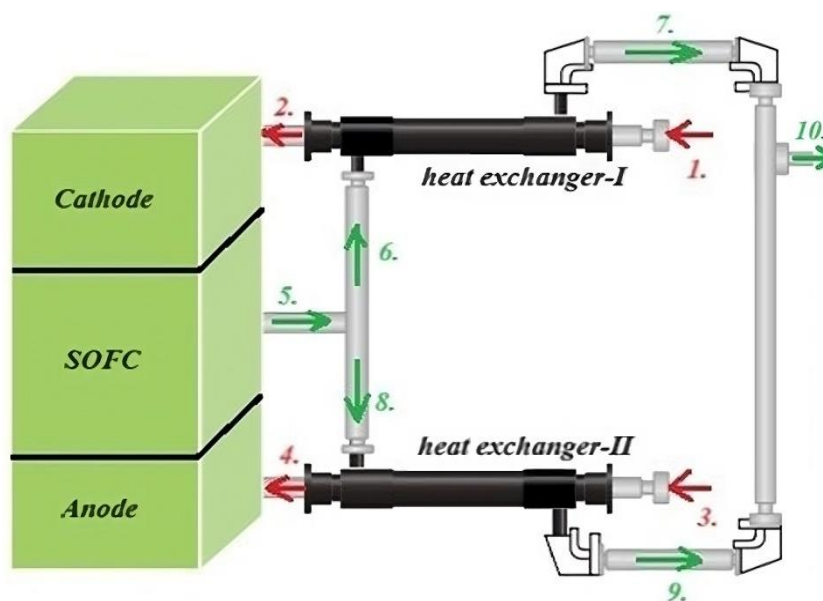


Figure 2. Flow chart of SOFC system.

Table 1. Thermodynamic properties of SOFC flow chart according to locations (T_0 . dead state).

Location	T [°C]	h (kJ/kmol)	\dot{N} [mol/s]	Composition (mol%)	s [kJ/kmolK]	Ex (Kw)
1.	25	0	1	CO:100	130.7	0
2.	694.7	19706	1	H ₂ :100	165.2	9.417
3.	25	0	2.381	O ₂ :21 N ₂ :79	198.7	0
4.	694.7	20665	2.381	O ₂ :21 N ₂ :79	244	23.736
5.	1000	-50866	2.881	H ₂ O:34.7 N ₂ :65.3	217.3	54.087
6.	1000	-50866	0.8239	H ₂ O:34.7 N ₂ :65.3	244	15.467
7.	317.5	-74785	0.8239	H ₂ O:34.7 N ₂ :65.3	217.3	2.301
8.	1000	-50866	2.057	H ₂ O:34.7 N ₂ :65.3	244	38.618
9.	317.5	-74785	2.057	H ₂ O:34.7 N ₂ :65.3	217.3	5.747
10.	317.5	-74785	2.881	H ₂ O:34.7 N ₂ :65.3	217.3	8.049
11.	190	-78833	2.881	H ₂ O:34.7 N ₂ :65.3	209.6	1.046
12.	85.51	-82076	2.881	H ₂ O:34.7 N ₂ :65.3	201.7	0.1678
13.	43.13	-83378	2.881	H ₂ O:34.7 N ₂ :65.3	197.8	0.01671
T0.	25	-83934		H ₂ O:34.7 N ₂ :65.3	162.2	

Table 2. Thermodynamic and calculations results for SOFC.

Parameters	values
Enthalpy change during fuel cell reactions (Δh)	-215452 (kJ/kmol)
Entropy change during fuel cell reactions (Δs)	-20.93 (kJ/kmol.K)
Electric power (\dot{W}_{fc})	188.81kW
Fuel cell energy efficiency (η_{fc})	% 87.63
Fuel cell exergy efficiency (ψ_{fc})	% 61.33
exergetic sustainability index	0.70
Carbon emissions	94.4 kg/h
Economic value of the generated electricity	34.42 \$/h

The technoeconomic analysis of the proposed system should be made more comprehensive by comparing it with similar plants in the existing literature. This comparison is an important step that will clearly demonstrate the economic feasibility of the proposed system.

Energy Production Costs: The energy production costs of the proposed system should be determined by analyzing the cost structure of each of the SOFC, S-CO₂ and Kalina cycles. In the existing literature, the energy production costs of similar plants generally vary between \$ 50-70 per kWh. Comparing the costs in the proposed system with this range is important for evaluating the economic sustainability of the system.

Payback Periods: The payback periods of the proposed system should be calculated based on investment costs and annual revenues. The payback periods of similar systems in the existing literature generally vary between 5-8 years. Whether the payback period of the proposed system remains in this range will be an important indicator for investors.

Net Present Value (NPV): The net present value analysis will show the long-term economic performance of the proposed system. The NPV values of similar plants are generally positive and around \$ 100,000. If the NPV value of the proposed system is above this value, it indicates that the system is attractive in terms of investment. This extended technoeconomic analysis will allow us to better understand the economic feasibility of the proposed system and increase its attractiveness to potential investors.

3.2. Results For S-CO₂ Analysis

Figure 3 gives the heat flow diagram of the supercritical carbon dioxide cycle.

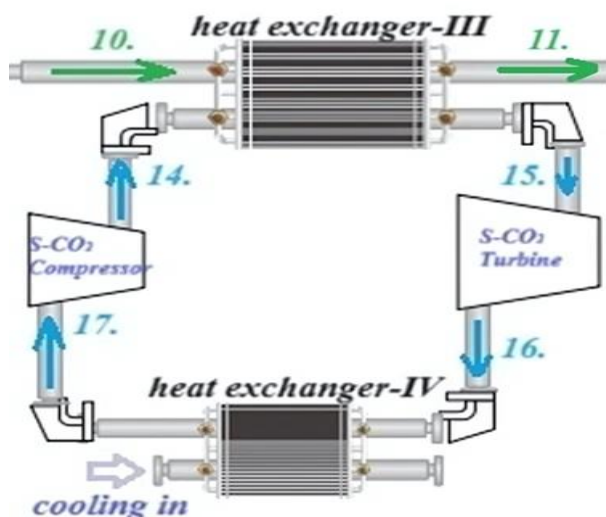


Figure 3. Flow chart of the S-CO₂ cycle.

Table 3. Thermodynamic data of the S-CO₂ cycle (T0, dead state).

Loc.	T [°C]	s[kJ/kg.K]	P [bar]	h [kJ/kg]	ex [kJ/kg]	m [kg/s]
14.	79.7	-1.075	140	-83.63	237.8	0.04629
15.	246.2	-0.4756	140	168.3	311.1	0.04629
16.	193.1	-0.4652	80	125	264.8	0.04629
17.	40	-1.08	80	-103.6	219.6	0.04629
T0.	25	0.00046	1	-0.883	0	-----

Table 3 presents the thermodynamic data of the S-CO₂ cycle. The table includes specific values of temperature (T), entropy (s), pressure (P), enthalpy (h), exergy (ex), and mass flow rate (m) at different locations. These data enable the analysis of the performance of the S-CO₂ cycle under various operating conditions.

Table 4. Results obtained within the of S-CO₂ cycle.

Parameters	Values
Electric power (\dot{W}_{s-co_2})	2 kW
S-CO ₂ heat transfer rate with heat exchanger-III (\dot{Q}_{s-co_2})	11.66 kW
S-CO ₂ energy efficiency (η_{s-co_2})	% 15.9
S-CO ₂ exergy efficiency (ψ_{s-co_2})	% 47.2
exergetic sustainability index	0.37
Carbon emission	1 kg/h
Economic value of electricity	10.26 \$/h

Table 4 presents the results for the Kalina cycle. The outcomes related to (S-CO₂) cycle are as follows: The electric power (\dot{W}_{s-co_2}) is determined as 2 kW, signifying the electricity generated by the S-CO₂ cycle. The transferred heat through heat exchanger-III (\dot{Q}_{s-co_2}) is 11.66 kW, representing the heat transfer within the system. The S-CO₂ energy efficiency (η_{s-co_2}) is calculated as 15.9%, illustrating the energy conversion efficiency of the S-CO₂ cycle. The S-CO₂ exergy efficiency (ψ_{s-co_2}) is 47.2%, showcasing how effectively S-CO₂ minimizes energy losses. The Exergetic Sustainability Index value is 0.37, reflecting the relationship between the system's energy efficiency and sustainability. Carbon emissions are 1 kg/h, providing a measure of the carbon emissions produced by the system. The economic value of electricity is determined as 10.26 \$/hour, expressing the economic viability of the electricity generated by the S-CO₂ cycle. These results encompass crucial parameters used to evaluate the performance and environmental impacts of the S-CO₂ cycle in the energy production process, indicating its potential to play an effective role in the energy sector.

3.3. Result For Kalina Cycle Analysis

Figure 4 shows the flow chart of the kalina cycle.

Table 5 provides the thermodynamic properties of the cycle. It includes data such as temperature (T), enthalpy (h), entropy (s), pressure (P), exergy (ex), mass flow rate (m), ammonia concentration (%NH₃), and the fluid used at different locations within the cycle. These properties are essential for analyzing the performance and behavior of the cycle under various operating conditions.

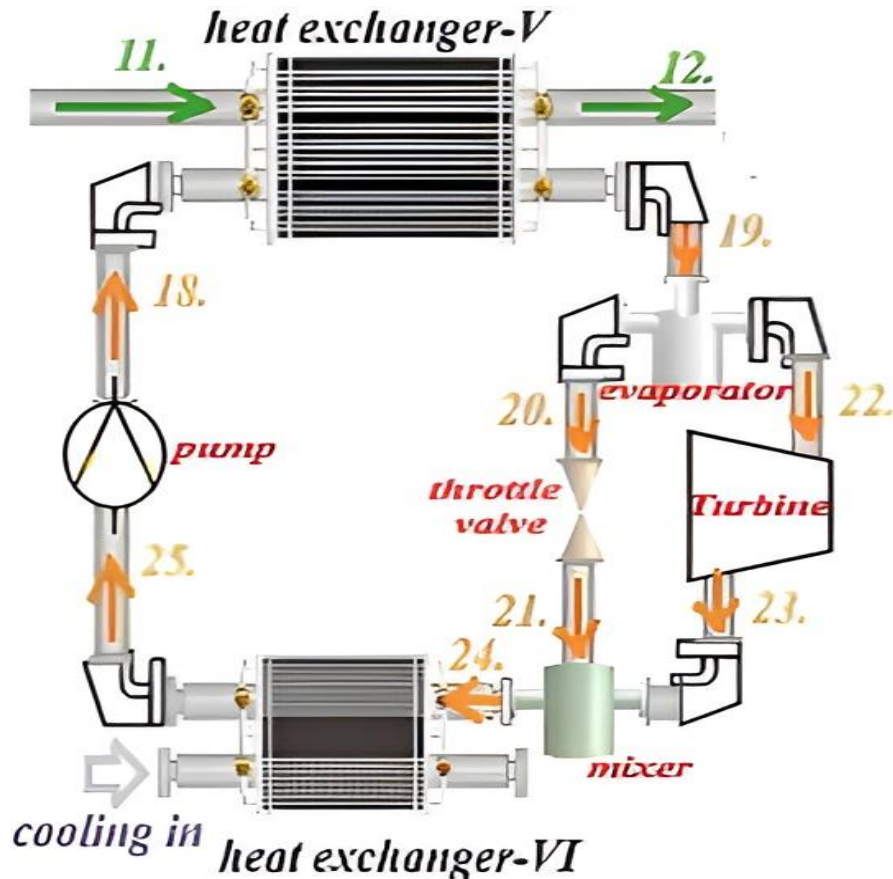


Figure 4. Kalina cycle flow chart.

Table 5. Thermodynamic properties of the cycle (T_0 . dead state).

Location	T [oC]	h [kJ/kg]	s [kJ/kg.K]	P [bar]	ex [kJ/kg]	m [kg/s]	X [%NH ₃]	Fluid
22.	115	1488	4.457	30	245	0.007204	0.9701	NH ₃ H ₂ O
23.	34.46	1267	4.585	5	-13	0.007204	0.9701	NH ₃ H ₂ O
20.	115	291.8	1.436	30	-82	0.000415	0.495	NH ₃ H ₂ O
21.	59.48	291.8	1.526	5	-107	0.000415	0.495	NH ₃ H ₂ O
24.	42.11	1164	4.267	5	-25	0.007618	0.92	NH ₃ H ₂ O
25.	40	130.8	0.6384	5	-13	0.007618	0.92	NH ₃ H ₂ O
18.	40.73	134.8	0.6433	30	-10	0.007618	0.92	NH ₃ H ₂ O
19.	115	1362	4.138	30	211	0.007618	0.92	NH ₃ H ₂ O
T[0].	25	-207.5	-0.5807	1	0	-----	----	NH ₃ H ₂ O

Table 6. Results obtained in the context of kalina.

Parameters	Values
Electric power (\dot{W}_{kalina})	1.59 kW
Kalina heat transfer rate with heat exchanger-V (\dot{Q}_{kalina})	9.35 kW
Kalina energy efficiency (η_{kalina})	16.9 %
Kalina exergy efficiency (ψ_{kalina})	10.9 %
exergetic sustainability index	0.20
Carbon emission	0.79 kg/h
Economic value of the electricity produced	7.74 \$/h

Results obtained for Table 6 in the Kalina cycle are as follows: Electric Power for the Kalina cycle (\dot{W}_{kalina}): 1.59 kW. This value represents the electric power generated by the Kalina cycle. Kalina Heat Transfer Rate with Heat Exchanger-V (\dot{Q}_{kalina}): 9.35 kW. It signifies the heat flow rate transferred through heat exchanger-V in the Kalina cycle. Kalina Energy Efficiency (η_{kalina}): 16.9%. This value expresses the energy efficiency of the Kalina cycle, indicating how effectively it converts incoming energy into

electrical energy. Kalina Exergy Efficiency (ψ_{kalina}): 10.9%. Exergy, a thermodynamic concept measuring the quality and usability of energy, indicates how efficiently the Kalina cycle utilizes energy resources. Exergetic Sustainability Index: 0.20.

This index evaluates the sustainability impact of the Kalina cycle. A low value may indicate less efficient use of energy resources or potentially more environmental harm. Carbon Emissions: 0.79 kg/h. Measuring the environmental impact, it represents 0.79 kg of carbon emissions per hour for the Kalina cycle. Produced Electric Economic Value: 7.74 \$/h. This value denotes the economic performance of electricity generated by the Kalina cycle per hour. These results provide crucial information for the assessment of the Kalina cycle's energy conversion efficiency, sustainability index, and economic performance.

3.4. Findings Related To S-CO₂ And Kalina Cycles

The inclusion of Super Critical Carbon Dioxide (S-CO₂) and Kalina cycles in the system integration has significantly increased the power increase. In this context, a power

increase of 3.59 kW and an efficiency increase of 1.90% have been achieved in the system. These findings show that the system has a significant impact on its overall performance.

Power Increase and Efficiency Increase: The integration of S-CO₂ and Kalina cycles has contributed to the increase in total power by increasing energy production. The obtained increase of 3.59 kW shows a significant improvement in the total power of the system, while the efficiency increase of 1.90% increases the energy conversion efficiency.

Energy and Exergy Efficiency: At this point, the improvements in energy and exergy efficiencies achieved with the addition of S-CO₂ and Kalina cycles should be clearly demonstrated. **S-CO₂ Cycle:** The energy efficiency of the S-CO₂ cycle is determined as 15.9% and the exergy efficiency as 47.2%. This helps to minimize energy losses in the system. **Kalina Cycle:** The energy efficiency of the Kalina cycle is 16.9% and the exergy efficiency is 10.9%. The integration of the Kalina cycle provides an effective method for the recovery of low-temperature waste heat.

As a result, the inclusion of the S-CO₂ and Kalina cycles positively affected the overall performance by increasing the energy efficiency of the system. These findings provide the basis for further optimization of the system in future studies.

3.5. Result For Hot Water Analysis

Figure 5 shows the flow chart for the system used to obtain hot water.

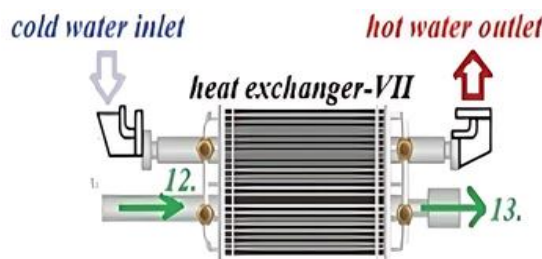


Figure 5. Hot water cycle flow chart.

Table 7. Thermodynamic properties of the cycle (T₀ dead state).

Loc.	T [°C]	s[kJ/kg.K]	P [bar]	h [kJ/kg]	ex [kJ/kg]	m [kg/s]
Cold water	25	0.3676	1	105.1	0	0.03588
Hot water	50	0.7043	1	209.6	4.108	0.03588
T ₀ water	25	0.3676	1	105.1	-----	-----

Table 7 presents the thermodynamic properties of the cycle, focusing on the properties of cold water, hot water, and the reference water temperature. It provides information such as temperature (T), entropy (s), pressure (P), enthalpy (h), exergy (ex), and mass flow rate (m) for each type of water at different locations within the cycle. These properties are crucial for understanding the heat transfer and energy exchange processes occurring within the cycle.

Table 8. Results obtained in the hot water cycle.

Parameters	Values
Heat exchanger-VII heat flow rate	3.75 kW
Obtained useful heat flow rate	3.75 kW
Hot water energy efficiency (η water)	100 %
Hot water exergy efficiency (ψ water)	97 %
Carbon emission	1.875 kg/h

The results for the hot water cycle are presented in Table 8, offering insights into the energy conversion efficiency, exergetic efficiency, and environmental impact of Heat Exchanger-VII used for hot water production. High energy and exergetic efficiency, coupled with low carbon emissions, indicate the effective operation of the system in hot water generation.

3.6. Findings And Analysis Results Of The Integrated System

Table 9. Results Obtained from the Integrated System.

Parameters	Values
Energy analysis (SOFC+S-CO ₂ +kalina+water)	89.1 %
Exergy analysis (SOFC+S-CO ₂ +kalina+water)	64.6 %
Exergetic sustainability index (SOFC+S-CO ₂ +kalina)	0.83
Carbon emission (SOFC+S-CO ₂ +kalina+hot water)	98.06 kg/h

Table 9 shows that when the whole system is combined and an integrated system;

Energy Analysis (89.1%), When the integrated system includes SOFC, S-CO₂, Kalina cycle and hot water integration, the total energy analysis was measured at 89.1%. Compared to other studies, especially Hasanzadeh et al. [27] and You et al. Similar to [28] studies, this system has achieved a very high energy efficiency of 89.1%. This indicates that the energy in the integrated system is used effectively.

Exergy Analysis (64.6%), When the integrated system was evaluated with the integration of SOFC, S-CO₂, Kalina cycle and hot water, the exergy analysis results were determined as 64.6%. Gholamian et al. [29] study reported an exergy efficiency of 62.35% in an ORC-based system, which is similar to 64.6% in this study. This indicates that the energy in the system is used effectively in terms of exergy.

Exergetic Sustainability Index (0.83), The sustainability index is used to evaluate the sustainability of the integrated system including SOFC, S-CO₂ and Kalina cycles. In this study, the exergetic sustainability index value was determined as 0.83. This shows that energy integration is successful in terms of sustainability.

Carbon Emission (98.06 kg/h), Evaluated together with SOFC, S-CO₂, Kalina cycle and hot water integration, the integrated system produces 98.06 kg carbon emissions per hour. This is considered an important indicator for assessing environmental impact.

Produced Electricity Economic (33.85 \$/h), The electricity economic value refers to the hourly electricity production economy of the integrated system including SOFC, S-CO₂ and Kalina cycles, and this value is determined as 33.85 \$. A low electricity economy indicates an economically efficient energy integration.

Each cycle in the proposed system integration (SOFC, S-CO₂ and Kalina cycles) is compared with experimental studies in the existing literature. These comparisons are important in supporting the accuracy of the system's performance and are presented as follows:

SOFC (Solid Oxide Fuel Cell) Comparison: Experimental studies on SOFC in the literature show that these cells operate at high temperatures and provide high

energy efficiency. The SOFC in the proposed system provides 87.63% energy efficiency and 61.33% exergy efficiency, which is consistent with similar experimental studies in the literature. These data are consistent with the thermal management and energy conversion capability of the SOFC and the data in the literature.

S-CO₂ Cycle Comparison: Experimental studies on the S-CO₂ cycle reveal that this system is an energy cycle that provides high efficiency and produces low carbon emissions. The 15.9% energy efficiency and 47.2% exergy efficiency obtained in our study are consistent with the experimental results in the literature and emphasize the environmental sustainability of the system.

Kalina Cycle Comparison: Experimental studies on the Kalina cycle in the literature show that this system is quite effective for the recovery of low-temperature waste heat. The 16.9% energy efficiency and 10.9% exergy efficiency obtained in the Kalina cycle in our study are consistent with similar experimental studies. These findings support that the Kalina cycle plays an effective role in the recovery of waste heat in our system. These comparisons confirm the accuracy of the performance of the proposed system integration and show that it largely overlaps with the experimental studies in the literature. However, the points where some aspects of the system differ from the experimental studies in the literature can be discussed and the reasons for these differences can be examined in future studies. Thermodynamic analyses were performed using the EES (Engineering Equation Solver) software [30].

4. Conclusion

The integration system shows high performance with its components including Solid Oxide Fuel Cell (SOFC), Super Critical Carbon Dioxide (S-CO₂) cycle, Kalina cycle and hot water recovery. While SOFC provides very successful results in terms of energy conversion efficiency, S-CO₂ and Kalina cycles have also been effective in electricity generation. Detailed energy and exergy analyses show that the existing energy resources in the system are used efficiently and that the system exhibits a sustainable profile with low carbon emissions.

- **Energy and Exergy Efficiency:** Detailed energy and exergy analyses show that the existing energy resources in the system are used efficiently and that it offers a sustainable profile with low carbon emissions.

- **Exergy Analysis Results:** Exergy analyses have determined the points where energy losses are the highest in the system. Optimizing the thermal management of the SOFC and efficient use of the ammonia-water mixture in the Kalina cycle will increase the exergy efficiency of the system. These improvements will be effective in minimizing energy losses and increasing system efficiency.

- **Entropy Production Amounts:** Entropy production values indicate the regions where thermodynamic irreversibilities in the system are concentrated. Entropy production can be reduced with optimizations, especially in heat exchangers and pressurized operating conditions. In this way, higher efficiency can be achieved.
- **Evaluation of Irreversibility:** Irreversibility in each component of the system is examined in detail with advanced exergy analysis. In particular, while examining the components of the SOFC, S-CO₂ and Kalina cycles, the energy efficiency of the SOFC was determined as 87.63%, exergy efficiency as 61.33% and carbon emissions as 94.4 kg/h. These results show the potential of minimizing the environmental impacts of the

system. The energy efficiency of the S-CO₂ cycle was determined as 15.9%, exergy efficiency as 47.2% and carbon emissions as 1 kg/h. These data reflect the effectiveness of the S-CO₂ cycle in energy conversion. The energy efficiency of the Kalina cycle was measured as 16.9%, exergy efficiency as 10.9% and carbon emissions as 0.79 kg/h. These results show how the Kalina cycle uses energy resources.

- **Areas for improvement:** The energy efficiency of the SOFC is 87.63% and the exergy efficiency is 61.33%. These efficiency values indicate that the thermal management of the SOFC needs to be optimized. Improving the thermal management will reduce energy losses and increase the overall efficiency of the system.
- S-CO₂ Cycle:** The energy efficiency of the S-CO₂ cycle is 15.9% and the exergy efficiency is 47.2% (Table 4). These values indicate that optimization of the heat exchangers and other components in the cycle is necessary. Improvements to the heat exchangers can increase the overall efficiency of the S-CO₂ cycle by increasing the heat transfer efficiency.
- Kalina Cycle:** The energy efficiency of the Kalina cycle is 16.9% and the exergy efficiency is 10.9% (Table 6). More efficient use of the ammonia-water mixture in the Kalina cycle is critical to increasing the energy conversion efficiency. Optimization of the ammonia-water mixture can contribute to increasing exergy efficiency.
- Hot Water Recovery System:** The results in Table 8 show that the energy efficiency of the hot water recovery system is 100% and the exergy efficiency is 97%. High efficiency values indicate the effectiveness of the hot water production system, while indicating that the current system can be improved with further integration and optimization. These findings are associated with suggestions for increasing the exergy efficiency of the system, defining applicable improvement areas. Thus, the overall efficiency of the system is increased, contributing to sustainable energy production. As a result, the integrated system approach presented in this study provides significant contributions in terms of energy efficiency and sustainability, and shows higher performance compared to current systems.

Nomenclature

C _{ei}	Exergoenvironmental impact coefficient	-
COP	Coefficient of performance	-
E	Energy consumption	kW·h
eCO ₂	Carbon intensity factor	kgCO ₂ /kW·h
ex	Exergy	kJ/kg
fe _i	Exergoenvironmental impact factor	-
h	Enthalpy	kJ/kg
HHV _{H₂}	Higher heating value of hydrogen	kJ/kmol
m	Mass flow rate	kg/s
P	Pressure	Bar
s	Entropy	kJ/kg·K
T	Temperature	°C
T _{fc}	Fuel cell absolute temperature	K
η	Efficiency	%
η _{fc}	Fuel cell energy efficiency	%
η _{Kalina}	Energy efficiency of Kalina cycle	%
η _{S-CO₂}	Energy efficiency of S-CO ₂ cycle	%
Φ _{ei}	Exergoenvironmental impact index	-
Φ _{est}	Exergetic sustainability index	-
ψ	Exergy efficiency	%
ψ _{fc}	Fuel cell exergy efficiency	%
ψ _{Kalina}	Exergy efficiency of Kalina cycle	%
ψ _{S-CO₂}	Exergy efficiency of S-CO ₂ cycle	%
Ṅ	Molar flow rate	kmol/s

\dot{Q}	Heat transfer rate	kW
\dot{S}_g	Entropy generation rate	kW/K
\dot{W}	Electric power	kW
Δh	Change in enthalpy	kJ/kmol
Δs	Change in entropy	kJ/kmol·K

References:

- [1] Y. Liu, J. Han, and H. You, "Exergoeconomic analysis and multi-objective optimization of a CCHP system based on SOFC/GT and transcritical CO₂ power/refrigeration cycles," *Appl. Therm. Eng.*, vol. 230, p. 120686, 2023.
- [2] D. Wang, H. A. Dhahad, M. A. Ali, S. F. Almojil, A. I. Almohana, A. F. Alali, and K. T. Almoalimi, "Environmental/Economic assessment and multi-aspect optimization of a poly-generation system based on waste heat recovery of PEM fuel cells," *Appl. Therm. Eng.*, vol. 223, p. 119946, 2023.
- [3] Y. Ji-chao and B. Sobhani, "Integration of biomass gasification with a supercritical CO₂ and Kalina cycles in a combined heating and power system: A thermodynamic and exergoeconomic analysis," *Energy*, vol. 222, p. 119980, 2021.
- [4] Z. Wang, Y. Ma, M. Cao, Y. Jiang, Y. Ji, and F. Han, "Energy, exergy, exergoeconomic, environmental (4E) evaluation and multi-objective optimization of a novel SOFC-ICE-SCO₂-HRSG hybrid system for power and heat generation," *Energy Convers. Manag.*, vol. 291, p. 117332, 2023.
- [5] Y. Zhou, X. Han, D. Wang, Y. Sun, and X. Li, "Optimization and performance analysis of a near-zero emission SOFC hybrid system based on a supercritical CO₂ cycle using solar energy," *Energy Convers. Manag.*, vol. 280, p. 116818, 2023.
- [6] W. Liang, Z. Yu, F. Bian, H. Wu, K. Zhang, S. Ji, and B. Cui, "Techno-economic-environmental analysis and optimization of biomass-based SOFC poly-generation system," *Energy*, vol. 285, Art. no. 129410, Jan. 2023.
- [7] H. R. Abbasi, H. Pourrahmani, and N. Chitgar, "Thermodynamic analysis of a tri-generation system using SOFC and HDH desalination unit," *Int. J. Hydrogen Energy*, vol. 46, no. 18, pp. 12345-12357, 2021.
- [8] N. Chitgar, M. A. Emadi, A. Chitsaz, and M. A. Rosen, "Investigation of a novel multigeneration system driven by a SOFC for electricity and fresh water production," *Energy Convers. Manag.*, vol. 196, pp. 296–310, 2019.
- [9] A. Kumar, A. K. Yadav, and S. Sinha, "Techno-Economic and Environmental Analysis of a Hybrid Power System formed from Solid Oxide Fuel Cell, Gas Turbine, and Organic Rankine Cycle," *J. Energy Resour. Technol.*, vol. 146, pp. 1–30, 2024.
- [10] A. Arsalis and G. E. Georghiou, "A decentralized, hybrid photovoltaic-solid oxide fuel cell system for application to a commercial building," *Energies*, vol. 11, no. 12, p. 3512, 2018.
- [11] P. Ran, X. Zhou, Y. Wang, Q. Fan, D. Xin, and Z. Li, "Thermodynamic and exergetic analysis of a novel multi-generation system based on SOFC, micro-gas turbine, S-CO₂ and lithium bromide absorption refrigerator," *Appl. Therm. Eng.*, vol. 219, p. 119585, 2023.
- [12] J. Pirkandi, M. Ghassemi, M. H. Hamed, and R. Mohammadi, "Electrochemical and thermodynamic modeling of a CHP system using tubular solid oxide fuel cell (SOFC-CHP)," *J. Cleaner Prod.*, vol. 29, pp. 151–162, 2012.
- [13] Y. Cao, S. Alsharif, E. A. Attia, M. A. Shamseldin, and B. F. Ibrahim, "A conceptual process design towards CO₂ emission reduction by integration of solar-based hydrogen production and injection into biomass-derived solid oxide fuel cell," *Process Saf. Environ. Prot.*, vol. 164, pp. 164–176, 2022.
- [14] U. Gunes, A. S. Karakurt, and B. Sahin, "The effect of size on entropy generation for waste heat recovery boiler," in *Proc. 32nd Int. Conf. Eff., Cost, Optim., Simul. Environ. Impact Energy Syst.*, 2019, pp. 809–818.
- [15] E. Yücel, B. Doğanay, F. Gökalp, N. Baycık, and Y. Durmuşoğlu, "Kalina çevriminin bir tanker gemisine entegrasyonu ve geminin enerji verimliliğine etkisinin analizi," *Seatific*, vol. 1, no. 1, pp. 26–36, Dec. 2021.
- [16] T. Koroglu and O. S. Sogut, "Advanced exergoeconomic analysis of organic rankine cycle waste heat recovery system of a marine power plant," *Int. J. Thermodyn.*, vol. 20, no. 3, pp. 140–151, 2017.
- [17] Y. Ust, A. S. Karakurt, and U. Gunes, "Performance analysis of multipurpose refrigeration system (MRS) on fishing vessel," *Pol. Maritime Res.*, vol. 23, no. 2, pp. 48–56, 2016.
- [18] J. Sieres and J. A. Martínez-Suárez, "Simulation of an integrated hydrogen fuel cell with LIBR-water absorption system for combined production of electricity, cooling and hot water," in *Proc. 8th Int. Conf. Heat Transfer, Fluid Mechanics, and Thermodynamics (HEFAT)*, Pointe Aux Piments, Mauritius, Jul. 2012, pp. 1163–1170.
- [19] R. A. Gaggioli and W. R. Dunbar, "Emf, maximum power and efficiency of fuel cells," *Energy Resour. Technol.*, vol. 115, pp. 100–104, 1993.
- [20] Y. A. Cengel and M. A. Boles, *Thermodynamics: An Engineering Approach*, 8th ed. New York, NY, USA: McGraw-Hill, 2011.
- [21] I. Dincer and M. A. Rosen, *Exergy: Energy, Environment and Sustainable Development*, 2nd ed. Amsterdam, The Netherlands: Elsevier Science, 2012.
- [22] A. Bejan, G. Tsatsaronis, and M. Moran, *Thermal Design and Optimization*. New York, NY, USA: John Wiley & Sons, 1996.
- [23] M. Sharifishourabi, "Energetic and Exergetic Analysis of a Solar Organic Rankine Cycle with Triple Effect Absorption System," M.S. thesis, Eastern Mediterranean Univ. (EMU), Famagusta, Cyprus, 2016.
- [24] J. Jeswiet and S. Kara, "Carbon emissions and CESTTM in manufacturing," *CIRP Annals*, vol. 57, no. 1, pp. 17–20, 2008.
- [25] International Energy Agency (IEA), "Global Energy & CO₂ Data," 2018. [Online]. Available: <https://www.iea.org/countries>. [Accessed: Aug. 2023].

- [26] IRENA, “REmap 2030 commodity prices,” [Online]. Available: https://www.irena.org/-media/Files/IRENA/REmap/Methodology/IRENA_REmap_2030_commodity_prices.xlsx?la=en&hash=505B546E4EE80A557363781E83EA1AE83D9FB256. [Accessed: Aug. 2023].
- [27] A. Hasanzadeh, A. Chitsaz, P. Mojaver, and A. Ghasemi, “Stand-alone gas turbine and hybrid MCFC and SOFC-gas turbine systems: Comparative life cycle cost, environmental, and energy assessments,” *Energy Rep.*, vol. 7, pp. 4659–4680, 2021.
- [28] H. You, Y. Xiao, J. Han, A. Lysyakov, and D. Chen, “Thermodynamic, exergoeconomic and exergoenvironmental analyses and optimization of a solid oxide fuel cell-based trigeneration system,” *Int. J. Hydrogen Energy*, vol. 48, no. 11, pp. 15950–15965, 2023.
- [29] E. Gholamian and V. Zare, “A comparative thermodynamic investigation with environmental analysis of SOFC waste heat to power conversion employing Kalina and Organic Rankine Cycles,” *Energy Convers. Manag.*, vol. 117, pp. 150–161, 2016.
- [30] S. A. Klein, *Engineering Equation Solver (EES)*, F-Chart Software, Version 10.835-3D, 2020.